OPTIMISATION AND FABRICATION OF ULTRA VIOLET EMITTING CuCl THIN FILMS BY RF SPUTTERING

A thesis for the degree of Doctor of Philosophy

Presented to

Dublin City University

by

Gomathi Natarajan, M.Sc.,

School of Electronic Engineering

Dublin City University

Supervised by

Prof. David Cameron

Dr. Stephen Daniels

March, 2007

Declaration

I hereby certify that this material, which I now submit for assessment on the programme of study leading to the award of Ph.D. is entirely my own work and has not been taken from the work of others save and to the extent that such work has been cited and acknowledged within the text of my work.

Signed: _____

(Candidate) ID No.: 52151042

Date: 09/03/07

Dedicated to…

My parents and family

Abstract

Wide direct band gap CuCl is a promising candidate for the next generation Si based optoelectronics, thanks to its excellent properties such as high excitonic binding energy (190 meV) and a close lattice matching with Si.

In this thesis, growth of CuCl using RF magnetron sputtering is investigated in detail. Stoichiometry and microstructure are the two major deciding factors for the UV emission from the film. We have successfully controlled both these properties by varying the sputtering parameters. Chemical stoichiometry was mainly controlled by the spacing between the target and substrate. An optimum spacing of 6 cm was found to yield films with Cu/Cl ratio almost close to stoichiometry (Cu/Cl = 0.94). A more fine control was achieved providing a suitable bias to the substrate and high quality stoichiometric CuCl films were obtained.

Microstructural evaluation revealed that the grain interface area of the film increases on increasing the sputtering pressure. UV emission properties were found to be influenced by the existence of meso- and nanostructural interfaces within the thin film. Cathodoluminescence studies showed a strong UV exciton emission and a green emission from deep levels in a non-stoichiometric and lower crystalline quality samples. CuCl films deposited with optimum sputtering parameters showed good optical quality with an intense and sharp UV emission at room temperature without any deep level emission.

Excitonic line transitions of sputtered CuCl films were investigated using temperature dependant PL spectroscopy. The thermal activation energy was calculated to be 112 meV. Our results show that the sputtered CuCl films have relative higher optical quality compared to the other UV emitting materials such as epitaxially grown GaN and ZnO, demonstrating the potential for Si based UV photonic devices.

Preliminary electrical studies were carried out to identify the conduction mechanism associated with the sputtered CuCl thin films. Field dependant DC conduction studies on CuCl/Si structure indicates that ohmic conduction prevails in the lower field region and an electrode limited Schottky emission process was found to dominate the mechanism of charge carrier transport through these structures at higher fields.

Acknowledgements

I would like to express my thanks and appreciation to many people who made this thesis possible and I hope the following few lines will be able to express my gratitude to all of them.

Firstly, I would like to thank my supervisors, Prof. David Cameron and Dr. Stephen Daniels. It is a pleasure to have worked with such high quality motivating researchers with immense scientific experience, knowledge, perceptiveness, problem solving, and also generosity for research and conference funding. The freedom they gave me to carry out my research during the entire period of my study was so great, and it has been essential to my successful thesis. I am very much thankful to them for their constant encouragement and valuable guidance throughout my PhD. I express my sincere thanks to the collaborative professors, Prof. Patrick McNally (DCU) and Dr. Louise Bradley, (Trinity College, Dublin) for their valuable input to this thesis.

I wish to thank my examiners, Prof. Martin Henry (School of Physics, DCU) and Dr. John Sheridan (Dept. of Electronic and Engineering, University College Dublin), for reading my thesis so thoroughly, adding interesting comments and conducting a very enjoyable viva.

I would like to thank Dr. R. T. Rajendra Kumar for his encouragement, valuable suggestions, teaching me the positive approaches to find fun in research.

Special thanks to our technician Billy Roarty, for his technical as well as moral support and bringing things from 2D drawings on papers to 3D working units. I would like to acknowledge Robert, Ger, Paul, Conor and Liam in Electronic Engineering in DCU for their helps at different levels.

Thanks to Dr. Aran Rafferty for his ideas in target preparation and allowing me to use their equipments. Thanks to Dr. Damien O'Rourke for his help with labview program which saved a lot of time for me.

I wish to extend my gratitude to my colleagues *cum* friends Ramprasad, Lisa, Francis and Anirban for their support during my stay at DCU. Thanks to all staff in Electronic Engineering and NCPST especially Breda (Electronic Engineering), Shiela and Sarah (NCPST).

Lastly but most importantly, I want to thank my parents, brother Balu, Swamy and all my friends in India for their moral support for making my Ph.D successful.

Gomathi Natarajan

DCU, Ireland, March 2007

Table of contents

List of tables and figures

Tables

Figures

Chapter 1

INTRODUCTION

1.1 Short-wavelength optoelectronics

Compact, high-efficient ultraviolet (UV) solid-state light sources such as light-emitting diodes (LEDs) and laser diodes (LDs) are of considerable technological interest as alternatives to large, toxic, low-efficiency gas lasers and mercury lamps. Microelectronic fabrication technologies and the environmental sciences both require light sources with shorter emission wavelengths; the former for improved resolution in photolithography and the latter for sensors that can detect minute hazardous particles.

Optical data storage is one of the major consuming fields of short-wavelength laser diodes (e.g. blue laser) to increase the data density of the optical disc formats (e.g. CDs, DVDs, etc.,). This technology requires a laser beam to write, read and erase the

data. The written data size, which is decided by the laser spot size, should be smaller to achieve higher storage densities. The shorter the laser wavelength, the smaller will be the spot size and hence the data storage capacity will be higher. This in turn means that the laser beams used to write/read out the data have to have ever-shorter wavelengths.

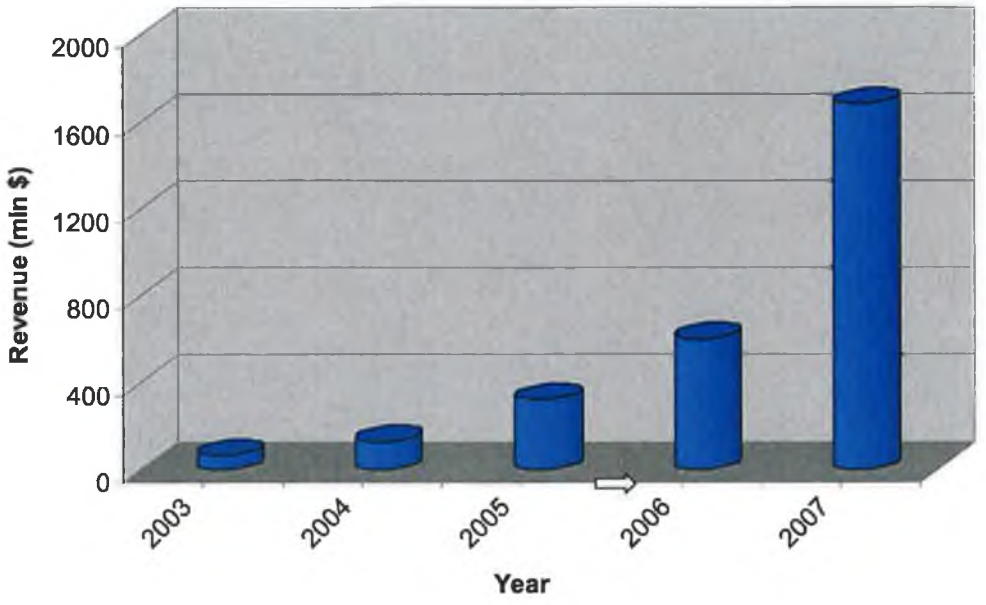

Figure 1.1. Worldwide market of UV/blue LDs (source: Compound semiconductors, 2006)

Figure 1.1 shows the market strategy of UV/blue LDs in the past few years and the forecast for the next year. Major companies such as Nichia, Sanyo, Sony, Cree, Toyoda, and NEC have been concentrating mainly on the on data storage applications of violet 405 nm LDs, neglecting other markets. Digital storage format using 405 nm LDs called Blu ray disc (BD) is expected to hold a storage capacity of up to 100 GB. In addition, ultraviolet solid-state light sources are also attracting attention for

potential applications in biomedicine and water purification, for example, ultraviolet light is used to sterilize hazardous organic matter.

To summarise the current thrusts in the applications using shortwavelength optoelectronics;

- Development of LED and related technologies to meet the requirements of lighting applications provides an energy-saving and environmentally-friendly light source and promotes the adoption of LEDs as a general light source for lighting in the 21st century.
- Development of short wavelength LDs to increase the capacity of optical data storage discs.
- Development of quantum dot technology to enhance the performance of LED/LD and to reduce manufacturing costs.

Light emitting diode configurations

There are two types of LEDs based on Metal Semiconductor Insulator (MIS) and p-n junction LED. In the metal-insulator-semiconductor (MIS) structure, light emission occurs through hot-electron impact excitation of electron-hole pairs. The operation of an ACTFEL device involves six primary physical processes, as illustrated in figure 1.2.

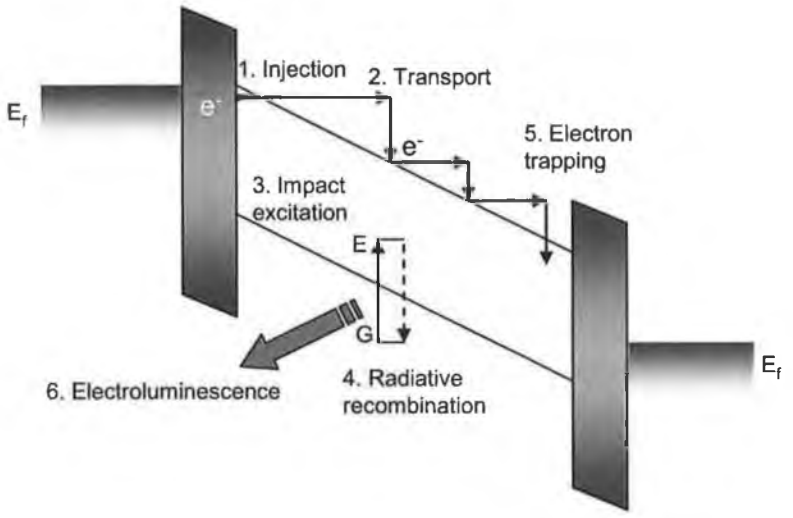

Figure 1.2. Energy band diagram illustrating the six primary physical processes of importance for operation of an MIS electroluminescence device

Upon the application of a sufficiently large voltage to the MIS device, the electrons trapped in interface states are tunnel-emitted into the semiconductor conduction band (Process 1). Subsequently, these injected electrons gain energy from the field and are transported across the semiconductor (Process 2). As these hot electrons transit the semiconductor layer, a fraction of them excite luminescent centres (Process 3) from their ground state to their excited states; the hot electron must concomitantly lose energy during this impact excitation process. Subsequently, the luminescent centre relaxes from its excited state to its ground state (Process 4), possibly giving off a photon during this energy relaxation process (the energy relaxation process can also occur non-radiatively, in which case the potential energy in the excited state is dissipated via the emission of phonons to the lattice). Eventually, the transported electrons reach the semiconductor/insulator anode interface and are trapped in interface states (Process 5). Finally, photons generated by radiative recombination are seen as a light emission from the device. (Process 6).

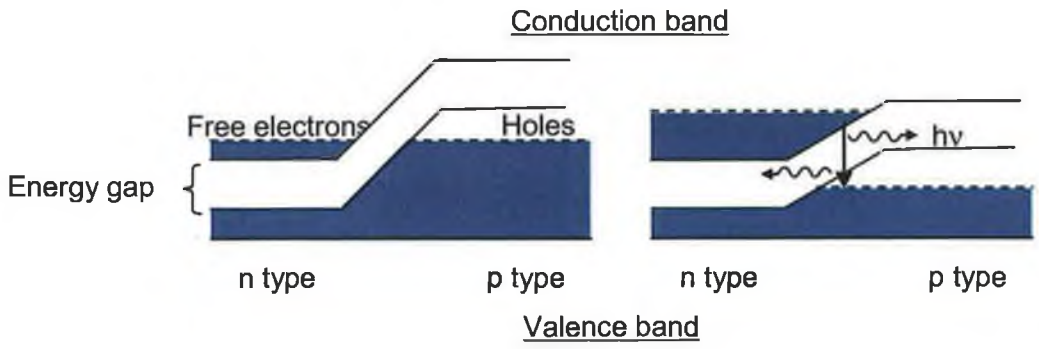

Figure 1.3. Band structure near a semiconductor p-n junction.
Left: No forward-bias voltage. Right: Forward-bias voltage present

Luminescence from a pn junction occurs as follow. Figure 1.3 shows the relative populations of the energy bands of both sides of a p-n junction with no voltage applied to the diode. The n-type material contains electrons which behave as the current carriers in its conduction band, whereas the p-type material has holes for carriers in its valence band. When a forward voltage is applied to the diode, the energy levels are caused to shift as illustrated in figure 1.3. Under these conditions there is a significant increase in the concentration of electrons in the conduction band near the junction on the n-side and the concentration of holes in the valence band near the junction on the p-side. The electrons and holes recombine and energy is given off in the form of photons. In principle LEDs based on p-n junction have many advantages over those based on MIS structure, including a high luminescence efficiency, higher emission intensity and reliable device characteristics.

1.2 Materials for short wavelength optoelectronics

In the search of materials for the development of blue/UV emitting devices, II-V materials such as ZnSe, ZnS, III-V nitrides such as GaN and its variants have been extensively investigated [1]. The short life time of the devices based on these compound semiconductors due to the high level of defect density prevented the commercialization of these devices. Among these, GaN brought a commercial breakthrough on S. Nakumura's [2] successful development of high brightness GaN based LEDs. Yet another potential material is the wide band gap ZnO which has also been widely investigated for short-wavelength applications. The important aspects and the recent developments in GaN and ZnO based optoelectronics are addressed briefly in the following sections.

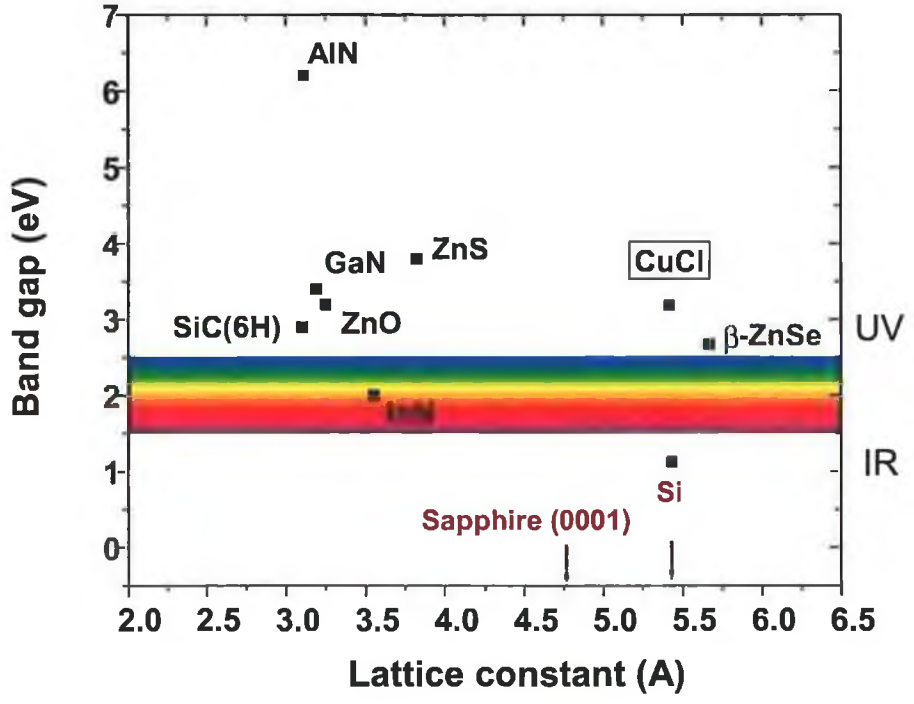

Figure 1 4. Band gap and lattice constants of various wide bandgap optoelectronic semiconductors

Materials for short-wavelength devices are not limited to GaN or ZnO. A recent report in Nature by Yoshitaka Taniyasu and colleagues [3] demonstrates a light-emitting diode (LED) with the shortest wavelength of any such device to date, which emits deep in the ultraviolet part of the spectrum. This research brings out a new material called aluminum nitride (AlN). Figure 1.4 shows various materials available for short-wavelength optoelectronic applications with their bandgap and lattice constant details. Lattice constants of sapphire and Si which are the popular substrate choices for these semiconducting layers are indicated.

a) Gallium Nitride and related compounds

GaN and related compounds such as InGaN and AlGaN have a wurtzite lattice structure with a direct band gap energy from 6.2 to 1.9 eV depending on the composition. The exciton binding energy of GaN is around 25 meV [4]. These III-Nitrides are typically hexagonally co-ordinated crystals with wurtzite structure, which are not grown as single wafers, due to the severe difficulty of so doing. Instead, these are grown epitaxially in thin single crystal layers on suitable substrates, typically Al_2O_3 (sapphire) or SiC. The major problem with this is that there are large lattice constant differences between the epilayers and the substrate. For example, in the case of GaN epitaxy on Al_2O_3, the lattice misfit is 13.6%. This leads to the generation of misfit dislocations (densities as high as 10^{10} cm^{-2}) which are deleterious to the performance of light emitting devices produced thereupon, as these defects act as non-radiative recombination centers [5,6].

Defect-related trapping and recombination limit the performance of the semiconductor devices. Trapping and non-radiative recombination at defects restricts minority carrier transport and contributes to localized heating. Progress to date in reducing the misfit dislocation density has focussed on improvements in the epitaxial techniques for growing the III-Nitride on the highly non-commensurate substrate (e.g. epitaxial lateral overgrowth, pendeo-epitaxy, etc.) [7,8].

The first GaN LED was reported in 1971 by Pankove *et al.* [9]. P- type doping of GaN could not be achieved at the time. Hence, this LED was not a *p-n* junction LED, it was a MIS LED. Electrons injected into a Zn doped (electrically high resistivity) GaN drop to Zn centers producing the emission in the visible range. However, an undesired yellow emission (2.2 eV) dominated the spectra over a weaker blue emission. The forward voltage required was almost 10 V and the measured efficiencies of these preliminary MIS LEDs were not encouraging even with a commercial venture by Matsushita.

In 1989, Akasaki *et al.* [10] demonstrated p-type GaN doping using Mg as a dopant and treating the layer by low-energy electron beam irradiation (LEEBI). The first GaN pn junction LED was demonstrated by the same group. However, the carrier concentration of the films was found to be very low, due to this it failed to reach production. On the other hand, GaN homo-junction LED's fabricated by Nakamura *et al.*[2] had higher hole concentration of 8×10^{18} cm^{-3} for p-type GaN films. Nakamura also used LEEBI treatment to obtain p-type GaN. Usually a MOCVD reactor has one gas flow, which is a reactive gas that flows parallel to the substrate. Nakumara

modified the commercial MOCVD reactor by adding a sub flow with an inactive gas blowing perpendicular to the substrate. This suppressed the large thermal convection where the growth temperature was 1000°C. This yielded high quality GaN layer, but the dislocation density is still as high as 10^{10} cm^{-3}, however the hole mobility was higher. With the improved quality epitaxial layer with the novel "two-flow MOCVD" reactor and enhanced p-type doping, the device had a sharp and intense emission with a FWHM of 55 nm at 405 nm. The external quantum efficiency was 0.18%, which was six times larger than that of commercially available SiC LED with emission wavelength of 480 nm. Even with the "two-flow MOCVD" reactor, the dislocation density was as high as 10^{10} cm^{-3}. Investigations to reduce the misfit dislocations have been focusing on the introduction of buffer layers and epitaxial lateral overgrowth [11,12].

b) Zinc oxide

Zinc oxide (ZnO) is another widely studied material for shortwavelength devices. It is a direct band gap II-VI semiconductor which has similar properties to GaN with wurtzite structure and band gap energy of 3.37 eV. A large exciton binding energy of 60 meV [13] is the key advantage of ZnO compared to GaN. This could lead to lasing action based on exciton recombination even above room temperature. There are several reports on the fabrication of ZnO nanostructures [14]. Even though research focusing on ZnO goes back many decades [15,16,17,18] the renewed interest is fueled by the availability of high-quality substrates and reports of p-type conduction

and ferromagnetic behavior when doped with transitions metals [19], both of which remain controversial.

While ZnO already has many industrial applications, owing to its piezoelectric properties and band gap in the near ultraviolet, its applications to optoelectronic devices have not yet materialized due chiefly to: i) high growth temperature and ii) the lack of p-type epitaxial layers. Very high quality what used to be called whiskers and platelets, now called nanostructures, have been prepared and used to deduce much of the principal properties of this material, particularly in terms of optical processes.

Attainment of *p*-type conductivity will result in the realization of the long-time target of exploiting this material for optoelectronic applications. As discussed earlier, it is very difficult to obtain p-type doping in wide-band-gap semiconductors, such as GaN, ZnSe and also ZnO. The difficulties can arise from a variety of causes. Dopants may be compensated by low-energy native defects, such as Zn interstitials (Zn_i) or Oxygen vacancies (V_O) [20], or background impurities. Low solubility of the dopant in the host material is also another possibility [21]. Deep impurity levels can also be a source of doping problem, causing significant resistance to the formation of shallow acceptor level. It has been believed that the most promising dopants for p-type ZnO are the group-V elements, although theory suggests some difficulty in achieving shallow acceptor level [22,23].

Following the success in the p-type doping of ZnSe with nitrogen [24,25], a number of groups have expended a good deal of effort in an attempt to realize p-type ZnO using nitrogen N as a possible shallow acceptor dopant [26,27,28,29,30,31]. Although Nitrogen has been considered as a best candidate, the main difficulty was that the solubility of N in ZnO was very low. To increase the solubility limit, a donor-acceptor co-doping was employed [32,33,34,35,36,37]. There are many reports on co-doping of N with some metal, for example Ga [35,38], In [39] and Al [40]. Although p doping is possible with this co-doping, some of the reports indicate increase in resistivity of several orders of magnitude [33,34,37]. Apart from nitrogen, other reported p type dopants include P [41,42], As [43]. Despite numerous efforts made to attain a p-type doping of ZnO, the reproducibility still remains a major problem, and this must be solved before ZnO can be used in optoelectronics applications such as homo-junction LEDs and laser diodes LDs.

Integration with Si microelectronics

Current substrate materials for the growth of GaN and ZnO are sapphire (Al_2O_3) or SiC. There are some issues with the above substrates for device fabrication such as,

(i) Insulating nature,

(ii) Cost,

(iii) Incompatibility with standard microfabrication processes.

Silicon is the most widely used semiconductor today and is abundantly available and significantly less expensive than many of the other potential substrates. This drives the development of optoelectronic devices that can be integrated with standard silicon

microelectronics as the optoelectronics and communication technologies become increasingly important. Over the past decade, there has been much progress in developing silicon-based optoelectronic devices such as waveguides, tunable optical filters, add/drop switches, optical modulators, CMOS photodetectors, photonic crystals, and micro-electro-mechanical systems. In addition to these devices, light sources such as lasers and light-emitting diodes are also important components of integrated optoelectronic circuits. Although silicon is not an ideal candidate for light emitting devices because of its indirect band gap, growing a direct-wide band gap layer on Si with high optical gain can resolve this issue. Si is an ideal platform for the optoelectronic device integration for the following reasons:

(i) Cost effective

(ii) Tuneable electrical properties

(iii) Well established microfabrication process

(iv) Monolithic integration of microelectronics

(v) Less heat dissipation problem (good heat conduction).

Epitaxial growth of GaN and ZnO layers on silicon substrates has been demonstrated by a few research groups [44,45]. However, there some few issues in the growth of III-V semiconductors on Si, namely (i) the difference in lattice parameter between these semiconductor layers and the Si substrate (e.g. lattice mismatch between GaN and Si is about 17%, refer figure 1.4), and (ii) difference in lattice symmetry.

Therefore there is a strong motivation for an alternative material which has lattice compatibility with Si which will enable the development of Si based optoelectronics.

Copper (I) chloride has a cubic zinc blende structure with a lattice constant, a_{CuCl} = 5.41 Å [46], which is very close (mismatch ~ 0.4 %) to that of Si (a_{Si} = 5.43 Å – diamond cubic) [47]. This close match in the crystal system and lattice parameters opens up a possibility for growing CuCl-Si with very low defect density.

1.3 CuCl – a proposed candidate for Si based UV/blue devices

As a potential alternative for GaN based materials, the wide band gap semiconductor CuCl (E_g = 3.395 eV) has very attractive features for optoelectronics such as room temperature exciton emission in the UV region and very high exciton binding energy. The binding energy of the excitons in CuCl is 190 meV and the excitonic radius is 0.7 nm [48]. The binding energy is very high compared to that of other important blue optoelectronic materials such as GaN (25 meV) [4] and ZnO (60 meV) [13] and hence the excitons are stable over wide temperature ranges. The exciton emission in the UV region, its large exciton binding energy and also close lattice matching with Si make CuCl a potential candidate for the development of Si based UV-blue emitting devices.

Two major issues with the current UV/blue materials are: (i) Growing high optical quality defect free thin film and, (ii) using a substrate material that is compatible with the current microfabrication technology. Growing CuCl on Si could solve both problems. The potential for use of CuCl in optoelectronics can be explained with reference to Table 1.1, which compares the key properties of CuCl with other compound semiconductors currently in use.

Material	Crystal structure	Exciton Binding energy	Lattice mismatch with Si	Limitations
GaN	Wurtzite	25 meV	17%	Expensive growth processes, Low optical gain
ZnO	Wurtzite	60 meV	18%	Unreliable p-type doping High temperature growth
CuCl	Cubic zinc blende	190 meV	0.4%	Aging effect (could be solved with a capping layer [50])

Table 1. 1 Comparison of the key features of CuCl with other UV emitting candidates

CuCl has a combination of large band gap, exciton stability at high temperatures and compatibility with Si substrates. One issue with CuCl is that it is hygroscopic in nature. When it is exposed to humid atmosphere for extended periods, it tends to absorb moisture and the film surface suffers from the formation of oxi-halides [49]. Our group has recently demonstrated that a suitable capping layer could solve this problem. Cyclo olyfin co polymer (COC) and polysilsesquioxane (PSSQ) layers on CuCl films were demonstrated to provide effective capping layers [50].

1.4 Literature survey

The previous investigations on CuCl focused on three main areas which are described briefly in the following sections: (i) Spectroscopic and theoretical studies on the band structure determination, and the excitonic transitions, (ii) Fabrication and optical investigations of CuCl micro/nano crystals in various matrices, (iii) Surface and interface studies of the epitaxial CuCl layers on various substrates.

a) Electronic structure and optical properties of CuCl

Optical and electronic properties of Cu halides were investigated in order to comprehend their band structures. Precise conclusions about the position of the electronic levels and the density of states in the valence band were extracted from photoemission experiments [51,52], ultraviolet spectroscopy [53,54,55,56] and x-ray spectroscopy [57,58]. Both theoretical [59,60] band structure calculations and experimental investigation using angle resolved spectroscopy were reported. These measurements were reviewed by Goldmann [61] and also semi-empirical model on the band structure was proposed by the same author [62]. To summarise these results: CuCl has a direct band gap of 3.4 eV. The valence band of CuCl is formed by a hybridization of the filled $3s^2$ and $3p^6$ shells of Cl^- ions and $3d^{10}$ shells of Cu^+ ions. The conduction band is predominantly formed by Cu 4s orbitals.

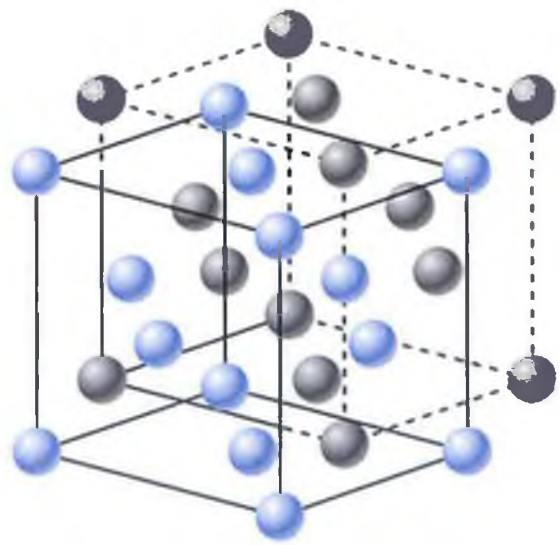

Figure 1.5. Crystal structure of γ-CuCl

CuCl exists in its zinc blende cubic structure (space group T_d^2) at room temperature. At a temperature of 422°C, it melts and transforms to a wurtzite crystal structure. Zinc blende structure is composed of two interpenetrating FCC sub-lattices occupied by Cu^+ and Cl^- atoms respectively, and shifted relatively to each other by ¼ of the space diagonal. The crystal structure of CuCl is given in figure 1.5. The zinc blende crystal structure has a Brillouin zone of truncated octahedron. The absorbance, photoluminescence and reflection spectra of CuCl display Mott-Wannier excitons.

An *exciton* is a bound state of an electron and a hole in a semiconductor, or in other words, a Coulomb correlated electron-hole pair, which is electrically neutral. In a CuCl crystal, the top of the valence band is the split-off hole (Γ_7), which is ~ 60 meV away from the degenerate heavy-hole and light-hole (Γ_8) bands. (Schematic shown in figure 1.6. The exciton consisting of the Γ_7 (Γ_8) hole and Γ_6 electron has been called the Z_3 (Z_{12}) exciton [62]. The edge excitons Z_{12} and Z_3 originate from the coupling of the lowest conduction band state Γ_6 to the uppermost valence band holes Γ_7 (Z_3) and Γ_8(Z_{12}). These edge excitons are called *Mott-Wannier* excitons.

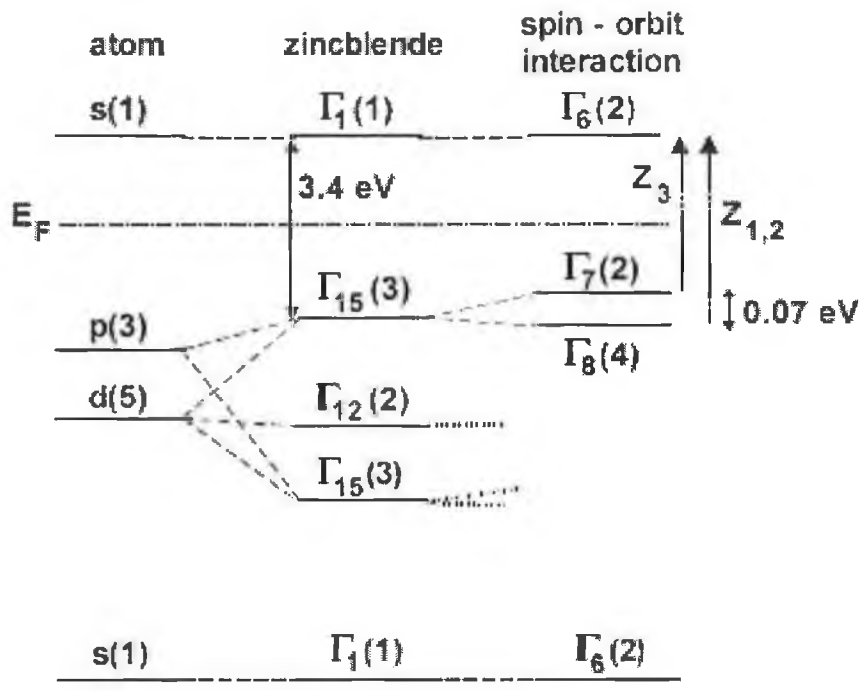

Figure 1.6. Schematic development of valence states due to s, p and d electrons at the Brillouin Zone center Γ in the cubic crystal field of the zincblende structure (not to scale) [13]

The binding energies of the excitons and biexcitons (excitonic molecules) are 190 meV and 34 meV [48], which are very much larger than those of III-V and II-VI semiconductors. Since the binding energy of the excitons is much larger than the thermal energy at room temperature (25 meV), excitonic luminescence in copper chloride is stable over wide temperature ranges. Also the Z_3 emission has a remarkably high quantum yield of almost close to unity for crystallites > 5 nm [63]. Thus the luminescence process in CuCl will have a high efficiency.

Under high density excitation, two excitons will interact with each other and forms an excitonic molecule or 'biexciton'. The biexciton formation is attributed to the

physical origin of optical non linear phenomena. That is, the biexciton is generated by strong laser irradiation and decays radiatively, leaving a free exciton in the crystal. Materials with high optical nonlinearity have applications in optical shutters and optical information processors. The binding energy of biexciton in CuCl is 34 meV. The biexciton binding energy is also higher in CuCl than other semiconductors, for example ZnO (15 meV [64]), ZnSe (8.5 meV [65] and CdS (6.3 meV [66]). Many studies have focused on the properties of the confined biexcitons in CuCl [12,15,16,20,26].

The optical properties Cu halides and their mixed crystals have been investigated by several researchers [48,53,67,68] as the excitonic binding energy is very large which makes it possible to perform investigations over wide temperature ranges. Formation of excitonic molecules, i.e biexcitons, is also observed in Cu halides. The optical gain mechanism due to biexcitons was first demonstrated in CuCl bulk crystal in 1971 by Shaklee *et al* [69]. Photoluminescence from biexcitons and biexcitons bound to an impurity, i.e bound biexciton, were investigated for CuCl films grown by MBE [70] and vacuum deposition [48].

b) Growth of CuCl microcrystals and epitaxial layers

The possibility of growing microcrystals stimulated a renewed interest in CuCl in the 1990s. CuCl microcrystals were fabricated using RF magnetron sputtering with composite target embedded with CuCl pellets [71,72,73]. CuCl microcrystals in SiO_2 were also prepared by the co sputtering of CuCl and SiO_2 [74]. The optical properties

of semiconductor quantum dots (QDs) have attracted much interest in recent years. The distance between the electron and the hole within an exciton is called Bohr radius of the exciton. The typical exciton Bohr radius in semiconductors is of the order of few nanometers. (~0.7 nm for CuCl).

When the length of a semiconductor is reduced to the same order as the exciton radius, i.e., few nanometers, quantum confinement effect occurs and as a result, modified and novel optical properties are expected. Hence, these structures are good candidates for developing high-performance opto-electronic devices such as semiconductor light-emitting diodes and laser diodes. CuCl quantum dots have been fabricated various matrices such as borosilicate glass [75,76], NaCl [77,78,79,80,81], sodalime aluminoborosilicate [82]. Similar quantum confined structures were grown by sputtering in SiO_2 host systems [71,72,74,73].

In nanocrystals, electrons, holes and, excitons are confined spatially, and their energy levels are quantized. This quantum-size effect is classified in to two limiting cases depending on the ratio (σ) of the radii of the nanocrystals (a) to the exciton a_B. For $\sigma > 1$, exciton translational motion is confined, while, for $\sigma < 1$, translational motion of an electron and a hole are individually confined. The former and latter are called exciton confinement (weak confinement) and electron-hole individual confinement (strong confinement), respectively. A CuCl nanocrystal is a typical example of the former, because its exciton Bohr radius (0.7 nm) is much smaller than the size of the nanocrystal.

Quantum confinement produces a number of important manifestations in the electronic and optical properties. This includes a blue shift in the band transition, increase in the binding energy of excitons and increase in oscillator strength. When the dimension of quantum confinement decreases, the band gap increases and this is observed as a blue shift in the exciton transition. The blue shift of the exciton energy is the ground state can be expressed as,

$$\Delta E = \frac{\hbar^2 \pi^2}{2M(a^*)^2} \qquad (1.1)$$

Where $a^* = a - 0.5\ a_B$, is the effective radius of a spherically shaped nanocrystal, a is the real nanocrystal radius, a_B is the exciton Bohr radius and M is exciton translational mass. The factor $a - 0.5\ a_B$ is included for the so called *'dead layer correction'* [84].

In the quantum confinement observed in the CuCl microcrystal systems, the edge excitons Z_{12} and Z_3 are shifted to a smaller wavelength in the microcrystals compared to bulk. The same was observed when the size of the microcrystallites was reduced [83]. For example a shift of $\Delta E = 15$ meV was observed for nanocrystals obtained by inductively coupled plasma assisted sputtering, which yielded a mean particle size of 3.5 nm [83]. The confinement of biexcitons is also reported by some authors [84,85]. Quantum confinement produces increased binding between electron and holes. This results in an increased binding energy of the excitons. In CuCl, an increase of the exciton binding energy of three times was observed by Masumoto *et al* [84].

Surface, interface studies and growth mechanisms of epitaxial layers of CuCl on a number of substrates are reported. Molecular Beam Epitaxy was used to grow epitaxial layers of CuCl on different substrates: Cu(100) bulk single crystals and Ag(111) single crystals [86], MgO [87,88,89], GaAs [90] and reconstructed (0001) Haematite (α–Fe_2O_3) [91]. CuCl epitaxial layers were also grown by thermal evaporation on CaF_2 [49,92], NaCl [93]. There is a report [90] on the growth of epitaxial CuCl on Si and GaAs which mainly focuses on the interface analysis and the island growth mechanisms in the early stages of film growth.

Recently, our group has explored the possibility of exploiting CuCl for Si based UV optoelectronics [94], and also demonstrated electroluminescence (EL) from CuCl/Si system with a simple MIS structure (AC-ELD) [95]. The present investigation deals with the growth of high quality CuCl films and evaluation of its properties from the device point of view. Sputter deposition possesses its own advantages which enable a controllable film growth and it is widely used in the large scale device fabrication in industries.

1.5 Scope of the thesis

This present research aims to step towards the challenge of the development of Si based optoelectronics using CuCl as an active UV emitting layer. The growth of a defect free CuCl-Si system with high optical quality is important for optoelectronic applications. Defect states including non stoichiometry and dislocations play an important role as non-radiative recombination centers which are mainly attributed to

near surface regions and grain boundaries [96,97,98,99]. From the device point of view, the effects of chemical stoichiometry and microstructure on the optoelectronic properties are crucial.

CuCl thin films are deposited by RF magnetron sputtering technique. Using various sputtering parameters, such as target to substrate distance, sputtering pressure and substrate bias potential, grain interface area and microstructure are controlled and a growth process is established to achieve stoichiometric and high optical quality films. The optoelectronic transitions are investigated using temperature dependant photoluminescence spectroscopy. Moreover, preliminary electrical investigations are carried out and electrical properties such as resistivity and field dependant conduction mechanisms are investigated. Based on the current work, some comments and suggestions are made at the end that can be investigated in future.

Chapter 2

METHODS AND TECHNIQUES

Magnetron sputtering is one of the potential physical vapor deposition (PVD) techniques for the controlled growth of thin films. CuCl films were deposited using a custom designed RF magnetron sputtering system. Structural, compositional, optical and electrical properties of the deposited films were analyzed using several techniques. The experimental details are briefly explained below.

2.1 Sputtering

Sputtering is a physical process which involves removal of the portions of a material called the target, and deposits a thin, firmly bonded film onto a substrate. The process occurs by bombarding the surface of the sputtering target with gaseous ions (out of a plasma) under high voltage acceleration. As these ions collide with the target, atoms or occasionally entire molecules of the target material are ejected and propelled

against the substrate, where they form a thin film. The process is realized carried out in a vacuum chamber which is pumped down before deposition starts (see figure 2.1).

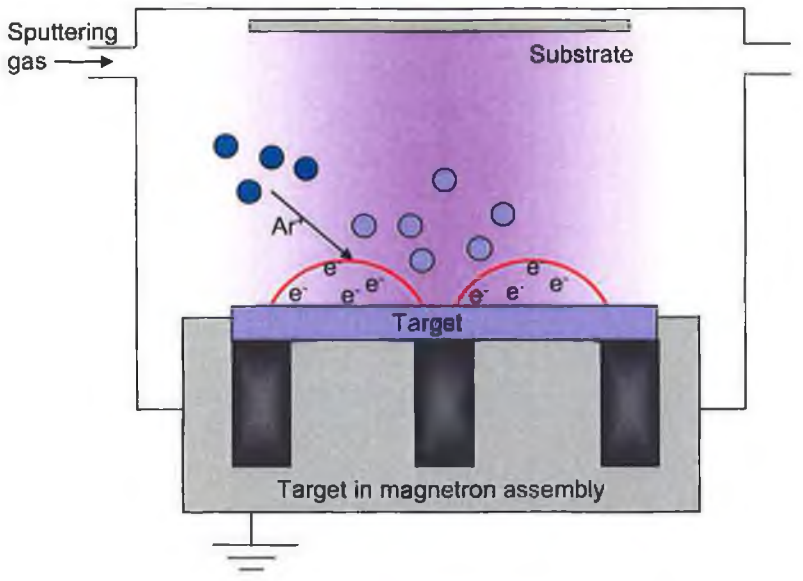

Figure 2.1. The principle of the sputtering process

Plasma is usually created with Argon which is fed into the chamber. By natural cosmic radiation there are always some ionized Ar^+ ions available. In DC-sputtering a negative potential U up to some hundred volts is applied to the target. As a result, the Ar ions are accelerated towards the target and remove the atoms on the surface, on the other hand they produce secondary electrons. These electrons cause a further ionization of the gas. In principle the ionization probability rises with an increase in pressure and hence the number of ions and the conductivity of the gas also increase. For a sufficient ionization rate a stable plasma results, wherefrom a sufficient amount of ions is available for sputtering of the material.

a) Magnetron sputtering

The fraction of ions in a plasma is significantly less than the total concentration of gas atoms (typical ion densities in a plasma are ~ 0.0001%). In general, this leads to reduced deposition rates of sputtering as compared with evaporation. Magnetron sputtering is used to increase the deposition rate. Magnetrons make use of the fact that a magnetic field configured parallel to the target surface can constrain the motion of secondary electrons ejected by the bombarding ions, to a close vicinity of the target surface. An array of permanent magnets is placed behind the sputtering source. The magnets are placed in such a way that one pole is positioned at the central axis of the target, and the second pole is placed in a ring around the outer edge of the target. A schematic of the magnetron assembly is shown in figure 2.1.

This configuration creates crossed E and B fields, where electrons drift perpendicular to both E and B according to vH = E/B. If the magnets are arranged in such a way that they create closed drift region, electrons are trapped, and rely on collisions to escape. By trapping the electrons in this way, the probability for ionization is increased by orders of magnitudes. Ions are also subjected to the same force, but due to their larger mass, the Larmor radius often exceeds the dimensions of the plasma. The trapping of electrons creates a dense plasma, which in turn leads to an increased ion bombardment of the target, giving higher sputtering rates and, therefore, higher deposition rates at the substrate. The electron confinement also allows for a magnetron to be operated at much lower voltages compared to basic sputtering (~ 500 V instead of 2-3 kV) and be used at lower pressures (typically mbar region).

There are two configurations in magnetron assembly such as (i) balanced magnetrons and (ii) unbalanced magnetrons. Balanced magnetrons have a tightly confined magnetic field. So the magnetic lines of force remain close to the target surface and the plasma is strongly confined to this area. This allows the field to be more easily optimized for high target utilization or rate. And, since electrons and ions are less likely to strike the substrate, the substrate stays cooler. Unbalance magnetrons are characterized by a less tightly confined magnetic field, so the magnetic lines of force extend further out in the chamber. Electrons and ions are therefore less tightly bound to the target region and electrons in particular can readily reach the substrate. The higher the electron density near the substrate heats it to a higher temperature, and provides a mechanism for ionization; both of which can be important in the film formation in some applications.

b) RF Sputtering

If insulating/dielectric targets (such as oxides or nitrides) are sputtered using DC voltages, the negative charge applied to the target is neutralized by the Ar ions. Eventually, positive charge builds up on the cathode (target) and hence no more ions will be attracted towards the target to carry out the sputtering process. A very high potential difference (10^{12} volts) between the electrodes is needed to sputter insulators. This creates practical difficulties. To overcome this, an alternating current in the radio frequency (RF) is used rather than DC.

At RF frequencies above 50 kHz, the ions do not have enough mobility to allow establishing a DC diode-like discharge and the applied potential is felt throughout the space between the electrodes. The electrons acquire sufficient energy to cause ionizing collisions in the space between the electrodes and thus the plasma generation takes place throughout the space between the electrodes. When an RF potential, is capacitively coupled to an electrode, an alternating positive/negative potential appears on the surface. During part of each half cycle, the potential is such that ions are accelerated to the surface with enough energy to cause sputtering while on alternate half-cycles, electrons reach the surface to prevent any charge build-up. RF sputtering can be performed at low gas pressures (<1 mbar). A major disadvantage in RF sputtering of dielectric targets is that most electrically insulating materials have poor thermal conductivity, high coefficients of thermal expansion, and are usually brittle materials. Since most of the bombarding energy produces heat, this means that large thermal gradients can be generated that result in fracturing the target if high power levels are used.

c) Sputtering parameters

The resulting film properties can be controlled by adjusting the following sputter parameters. The sputtering power determines mainly the rate of the deposition process and hence the time which remains for the arriving particles during the growth process for either surface diffusion and agglomeration on existing growth centers or nucleation with other ad-atoms. It also determines the maximum energy, with which sputtered particles can escape from the target (reduced by the binding energy).

Energies of the sputtered particles show a broad distribution with a maximum of the distribution between 1 eV and 10 eV. The energy distribution of the sputtered atom is usually assumed to obey the Thompson distribution [100] which is expressed by [101],

$$f(E)dE = C\left(1-\sqrt{\frac{U+E}{\gamma E_i}}\right)\frac{E}{(U+E)^3}dE \tag{2.1}$$

$$\gamma = \frac{4M_g M_t}{(M_g+M_t)^2} \tag{2.2}$$

where U is the binding energy of the target material, E_i is the average energy of the incident ions C is a normalization constant and γ is the fractional energy transfer from the projectile to the target atom. M_g and M_t are masses of projectile and target atoms respectively. The sputtered atoms or molecules undergo collisions during their travel from the target to the substrate, thereby continuously losing their energy and directionality. When a sputtered neutral of mass M_s collides with the argon ambient with a mass M_g, the sputtered neutral is scattered from the normal of the target by an angle of α [102],

$$\alpha = \tan^{-1}\left(\frac{M_s}{M_g}\right) \tag{2.3}$$

The maximum energy transfer during the collision can be expressed by [103],

$$E_m = \left[\frac{4M_sM_g}{(M_s+M_g)^2}\right]E_1 \tag{2.4}$$

Were E_1 is the energy of the sputtered atom before collision.

The sputtering pressure P determines the mean free path λ for the sputtered material, which is proportional to 1/P. Pressure has a direct influences on the mobility of the particles on the substrate surface. Target-substrate distance (d_{ts}) influences the film composition and also the crystallinity of the films. In principle a bias-voltage (V_b) can be applied to the substrate (typically ± 100 V), which has the effect of accelerating electrons or ions towards the substrate or keeping them away. Both may have an influence on the film composition and crystallinity and the density.

d) Features of sputtering

Sputtering has become one of the fastest-growing techniques in modern manufacturing. In fact, today's technologists are using it to coat more surfaces in more industries than ever before. From semiconductors to credit cards; from compact discs to auto parts; magnetron sputtering is adding new value to a growing list of products every day. This process can be used to deposit virtually all metals, alloys and compounds and provides a unique combination of advantages. The specific advantages of sputtering are given below.

(i) The high kinetic energy of sputtered atoms gives better film adhesion.

(ii) Since coverage is independent of line-of-sight, sputtering inherently produces uniform film coatings over nonflat surfaces.

(iii) Unlike evaporation techniques, which require horizontal placement of the crucible containing molten material and vertical placement below the substrate, sputtering works in any orientation, providing it faces the substrate.

(iv) It offers much greater versatility than other approaches because, as a cold momentum-transfer process, it can be used to apply either conductive or insulating materials to any type of substrate - including metals, ceramics, and heat-sensitive plastics.

(v) Sputter-cleaning of the substrate in vacuum prior to film deposition can be done.

(vi) For industrial applications, sputtering can be made a continuous, inline process.

(vii) Film properties (for e.g. composition, microstructure, step coverage) can be more easily accomplished, than any other techniques, by varying any one of or the combination of the sputtering parameters such as target to substrate spacing, sputtering gas pressure, sputtering gas/ion type, biasing the substrate.

Despite many advantages mentioned above, sputtering has the following disadvantages:

(i) High capital expenses are required (target)

(ii) Rates of deposition of some materials (such as SiO_2) are relatively low

(iii) Materials such as organic solids are easily degraded by ion bombardment

(iv) Sputtering has a greater tendency to introduce impurities in the substrate than deposition by evaporation because the former operates under a lower vacuum range than the latter.

2.2 Film deposition

a)

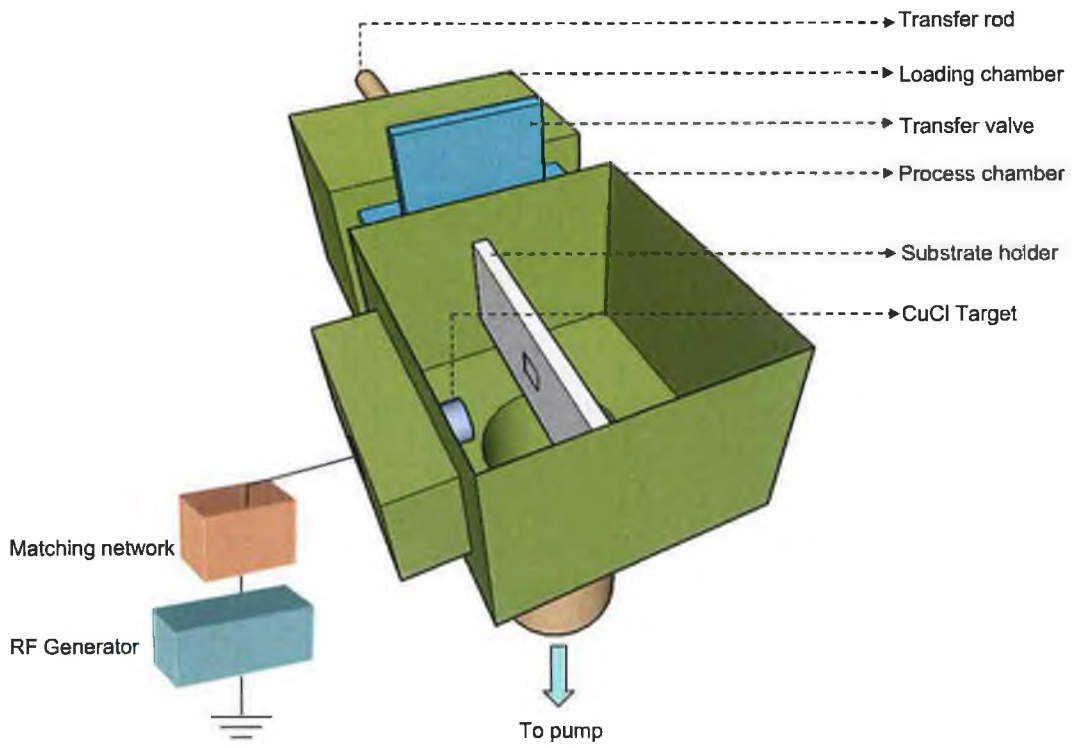

b)

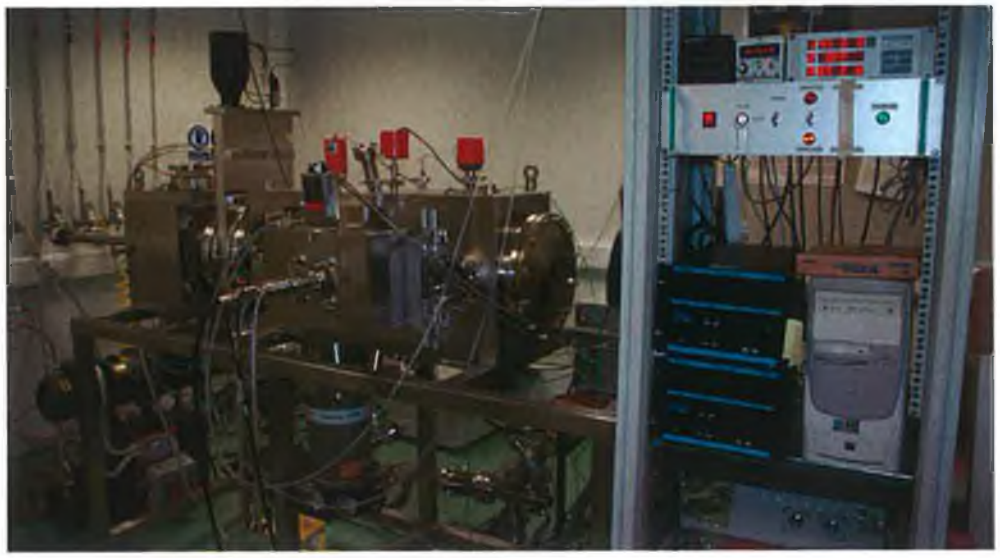

Figure 2.2 a) Schematic and b) photograph of RF magnetron sputtering system

CuCl films were deposited using a custom designed RF magnetron sputtering system which is shown in figure 2.2. The films deposited on Si and glass substrates. This system consists of two chambers namely (i) a process chamber and (ii) a loading chamber. The target is placed in the process chamber where the sputtering process takes place. The process chamber is kept under vacuum all the time.

The substrate holder is transported in to the process chamber with a transport assembly through loading chamber. The vacuum system has a rotary pump, which takes the chambers to a rough vacuum of around 10^{-3} mbar. A cryo pump is used to pump down the system to a higher vacuum level (as low as 10^{-8} mbar). RF power is applied through a matching network to the electrode where the target is fixed in a water-cooled magnetron assembly. The system is pumped down to a vacuum of approximately 10^{-7} mbar and then the argon gas is let in through a mass flow controller (MFC). An intentional bias voltage was applied to the substrates in some experiments. A second RF power supply was used for this purpose. The CuCl target is pre-sputtered for 10 minutes prior to deposition. Optical emission spectroscopy and electrical impedance monitoring of the magnetron source showed that this period of time was necessary to allow the sputtered flux to reach a steady state. The substrate is kept at room temperature and the temperature during the process is monitored with a thermocouple fixed on the substrate holder.

There are several challenges in the CuCl target preparation since CuCl is thermally and electrically non-conductive. CuCl compound targets cannot be easily prepared by melting process like metal or and alloy targets. However, we made a number of

attempts to melt the CuCl powder. When the powder was heated above 250°C, it turned black as it got oxidized. This was not successful even under vacuum or inert gas atmospheres (N_2, Ar). On the other hand, CuCl targets were prepared by pressing CuCl powder mechanically under very high compressive force using a hydraulic press, which was found to be successful. The optimized holding time and the pressure were 60 seconds and 10 kg/cm^2, respectively.

RF power is an important parameter for sputter deposition of CuCl. Various power levels were employed up to 5 W/cm^2. High power sputtering resulted in a very quick erosion of the target. Also, the target got oxidized and also became coppery due to the heat produced at such higher power levels. This kind of localized heating is usually due to the magnetron race track. Due to very low thermal conductivity of CuCl, the heat dissipation within the target is poor. When the power level is too low, plasma could not be ignited. A power density of 0.5 W/cm^2 was found to be optimum and all the depositions were performed in this condition. The target to substrate distance was varied from 3-9 cm and sputtering pressure was also varied from 1.1×10^{-3} to 1×10^{-2} mbar. Another RF supply was used to provide an intentional bias to the substrate. Film thickness was ~ 400 nm for a deposition period of 30 minutes. The influence of these parameters on the film properties will be investigated in chapter 3 and 4.

Plasma stabilization monitoring

Plasma conditions were monitored using non invasive techniques such as Optical Emission Spectroscopy (OES) and Plasma Impedance Monitoring (PIM). Emission lines from the plasma are collected by a SOFIE fiber optic spectrometer and a fiber optic cable, which is fixed in the UV-visible transparent (Sapphire) window.

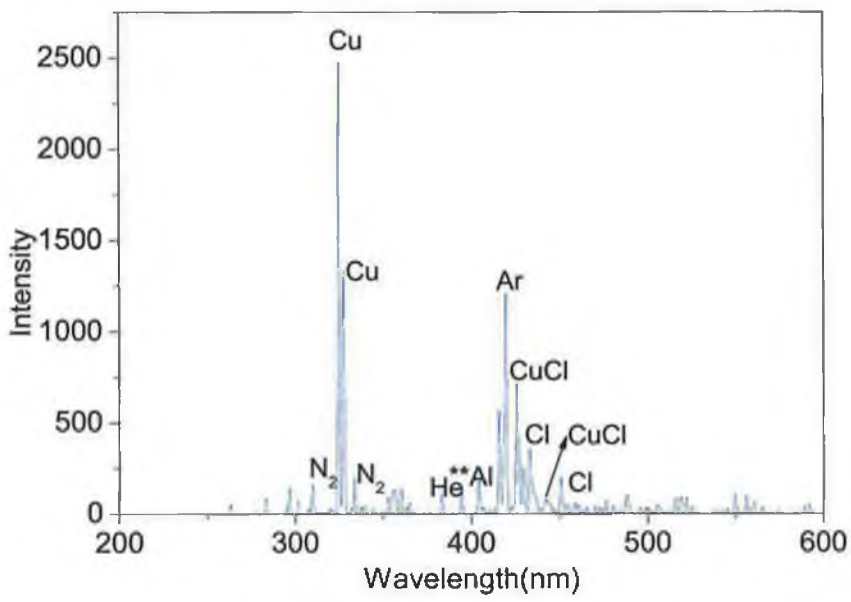

Figure 2.3 Optical emission spectra (Power = 0.5 W/cm^2, Pr = 1.1×10^{-3} mbar, d_{ts} = 6 cm)

a)

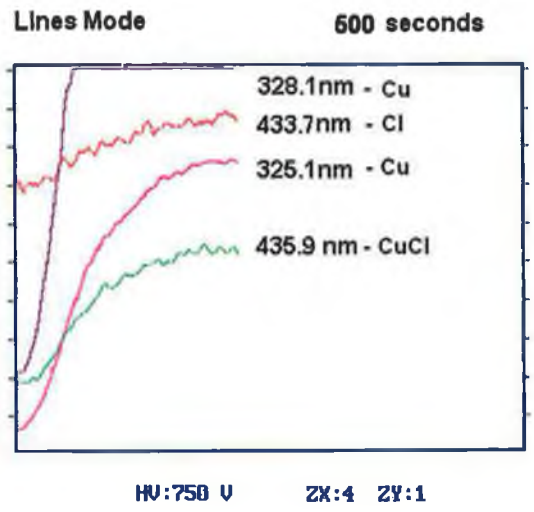

b)

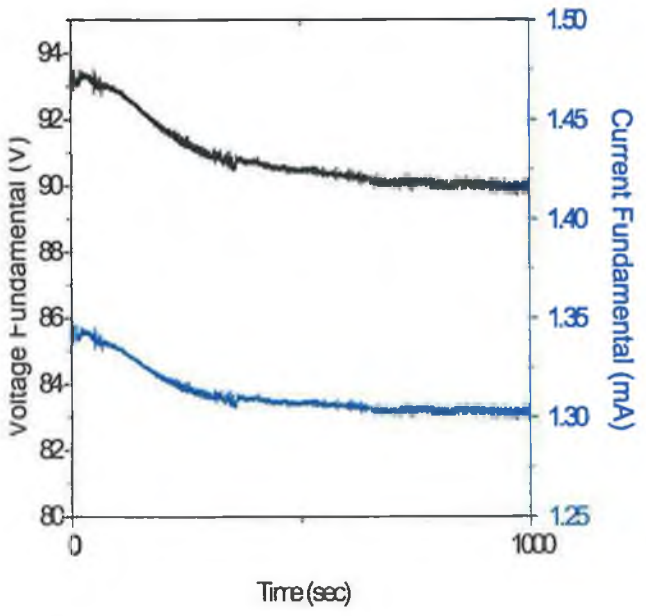

Figure 2.4 a) OES line intensities with time and b) Change in voltage, current fundamentals (PIM) (Power = 0.5 W/cm^2, Pr = 1.1×10^{-3} mbar, d_{ts} = 6 cm)

The next technique for plasma monitoring involves a plasma impedance monitoring device by Scientific Systems. Information on the amplitudes of voltage and current first four harmonics, as well as on the value of phase shift between them can be monitored simultaneously. The variation in PIM signals and optical emission line intensities with time is given in figure 2.4b. The voltage and current fundamental decrease and stabilizes after a time period of about 10 minutes, indicating the stabilized plasma conditions. Interestingly it was observed that the plasma line emission intensity levels and the voltage fundamental stabilize at about the same point after the plasma is ignited. This stabilization in the above signals can be related to the oxidation of few layers of the target and once they are sputtered away, the signals were stable. The target was presputtered until these were stabilized and then the substrate was introduced for deposition.

2.3 Characterization techniques

a) X-ray diffraction analysis

X-ray diffraction (XRD) is one of the vital techniques to characterize the structure of the crystalline material. This technique has a wide range of applications including few of the following: phase identification, lattice parameter quantification, grain size calculation, texture analysis. Diffraction effects are observed when electromagnetic radiation impinges on periodic structures with geometrical variations on the length scale of the wavelength of the radiation.

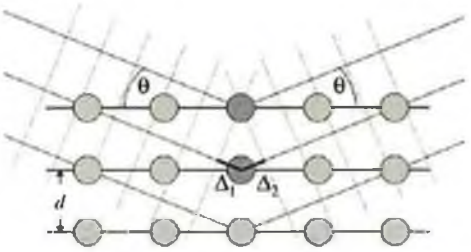

$$\Delta_1 + \Delta_2 = 2d\cos(90° - \theta) = 2d\sin\theta$$

Figure 2.5. Visualization of Bragg equation: Maximum intensity is observed only when the phase shifts add to a multiple of incident wavelength λ

Figure 2.6. Photograph of a Bruker AXS D8 Advance XRD system

The inter-atomic distances in crystals and molecules are in the range of 0.15–0.4 nm which correspond in the electromagnetic spectrum with the wavelength of X-rays having photon energies between 3 and 8 keV. Accordingly, phenomena like

constructive and destructive interference should become observable when crystalline and molecular structures are exposed to X-rays. Diffraction is only observed when a set of planes makes a very specific angle (Bragg angle) with the incoming X-ray beam (figure 2.5). The crystallinity of the CuCl films grown on glass substrates was examined using a Bruker D8 AXS advance instrument (figure 2.6) with Cu K_α radiation of wavelength 1.54 Å. The XRD spectra were measured in the Bragg-Brentano (θ–2θ) geometry.

b) Atomic force microscopy

Atomic force microscopy (AFM) is a technique from the family of scanning probe microscopy which allows imaging of samples in nanoscale. AFM consists of a micro-scale cantilever with a sharp tip (probe) at its end that is used to scan the specimen surface. The cantilever is typically silicon or silicon nitride with a tip radius of curvature in the order of nanometers. When the tip is brought into proximity of a sample surface, forces between the tip and the sample lead to a deflection of the cantilever according to Hooke's law.

a)

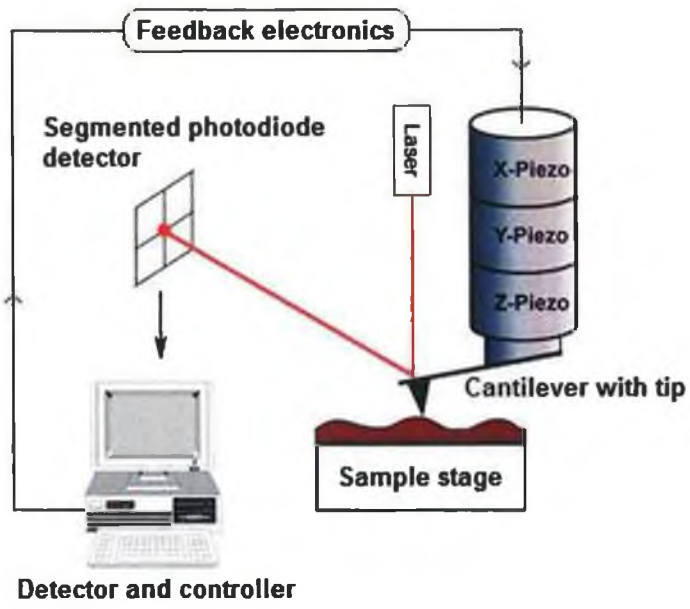

b)

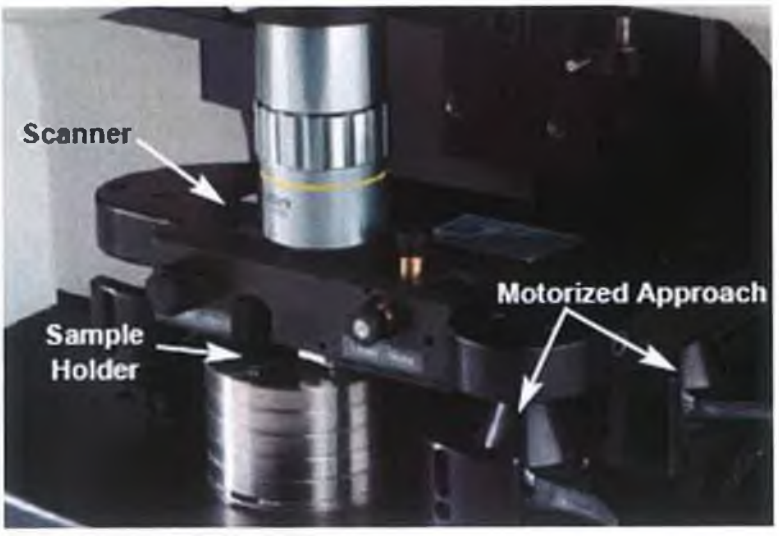

Figure 2.7 a) Schematic and b) photograph of an AFM scanning set up

The schematic of an AFM imaging system is shown in figure 2.7. As the cantilever flexes, the light from the laser is reflected onto the segmented photo-diode. By measuring the difference in the signal, changes in the bending of the cantilever can be measured. The movement of the tip or sample is performed by an extremely precise positioning device made from piezo-electric materials. Contact mode is one of the most common methods of operation of the AFM for high-resolution imaging of small areas. As the name suggests, the tip and sample remain in close contact as the scanning proceeds. Tapping mode is another generally adopted method mode of AFM for large scans. In this mode, the cantilever oscillates at its resonant frequency by maintaining a constant distance from the surface so that it only taps the surface for a very small fraction of its oscillation period.

AFM has several advantages over electron microscopes. It gives a three dimensional profile of the sample, can be operated in ambient and requires less sample preparation. A disadvantage of AFM is that the resolution is limited by the radius of curvature of the probe tip. For the analysis of CuCl thin films, we used a Pacific Nano Technology Nano-R system shown in figure 2.7b. The minimum scan size of this system is 0.7 micron. The samples were scanned in a contact mode scanning using silicon nitride probes.

c) X-ray Photoelectron Spectroscopy

X-ray Photoelectron Spectroscopy (XPS, also known as ESCA) uses highly focused monochromatised X-rays to probe the material of interest. Figure 2.8 illustrates the

principle of X-ray photoelectron spectroscopy. The energy of the photo-emitted electrons ejected by the X-rays is specific to the chemical state of the elements and compounds present, i.e. bound-state or multivalent states of individual elements can be differentiated. The presence of peaks at particular energies therefore indicates the presence of a specific element in the sample under study. Furthermore, the intensity of the peaks is related to the concentration of the element within the sampled region.

The binding energy of the core level electron is given by the following Einstein's relationship;

$$E_b = h\upsilon - E_k - \phi \qquad (2.5)$$

Where hν is the X-ray photon energy, E_k is the kinetic energy of the photoelectron. ϕ is the work function induced by the analyser. Since the work function can be altered artificially, it can be eliminated and the above expression can be simplified as,

$$E_b = h\upsilon - E_k \qquad (2.6)$$

The exact binding energy of an electron depends not only upon the level from which photoemission is occurring, but also upon:

(i) the oxidation state of the atom

(ii) the local chemical and physical environment

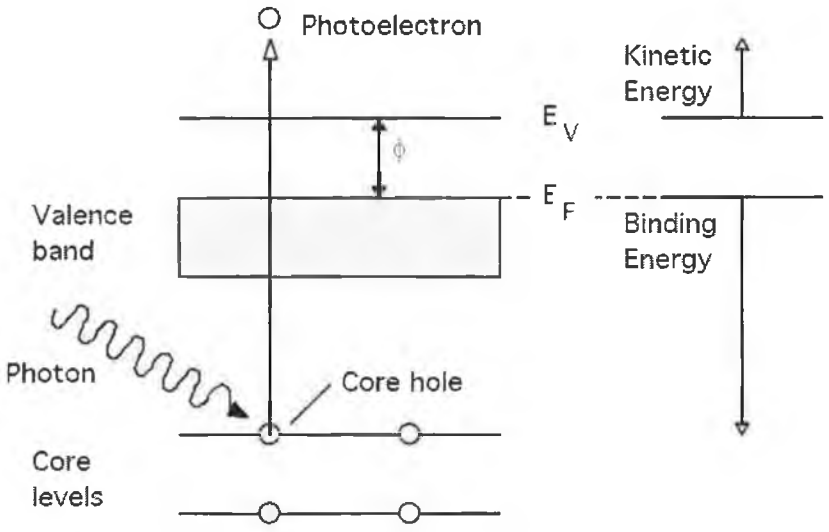

Figure 2.8. Schematic of the emission of photo electron from the core level from the absorption of a photon.

Changes in either of the above gives rise to small shifts in the peak positions in the spectrum - so-called *chemical shifts*. Such shifts are readily observable and interpretable in XPS spectra because the technique is of high intrinsic resolution (as core levels are discrete and generally of a well-defined energy) and it is a one electron process. Atoms of a higher positive oxidation state exhibit a higher binding energy due to the extra coulombic interaction between the photo-emitted electron and the ion core. This ability to discriminate between different oxidation states and chemical environments is one of the major strengths of the XPS technique. CuCl samples were analysed using a VG Microtech electron spectrometer at base pressures in the preparation and analysis chambers of $2x10^{-10}$ and $1x10^{-10}$ mbar respectively. The photoelectrons were excited with an X-ray source using MgK_{α} ($h\nu$ = 1253.6 eV) and the pass energy of the analyser was 20 eV. The calibration was done using the carbon peak.

d) Scanning electron microscopy

Scanning Electron Microscope (SEM) is one of the potential tools widely used for surface analysis. It makes use of an energetically well-defined and highly focused beam of electrons that scans across the sample. SEM works on the principle that the electron beam generates a "splash" of electrons with kinetic energies much lower than the primary incident electrons, called secondary electrons. Detection of secondary electrons as a function of primary beam position makes it possible to attain images with high magnifications. Figure 2.9 shows various signals coming out of the *interaction volume* of the sample when it is illuminated by an electron beam. The interaction volume is the volume inside the specimen in which interactions occur while being struck with an electron beam.

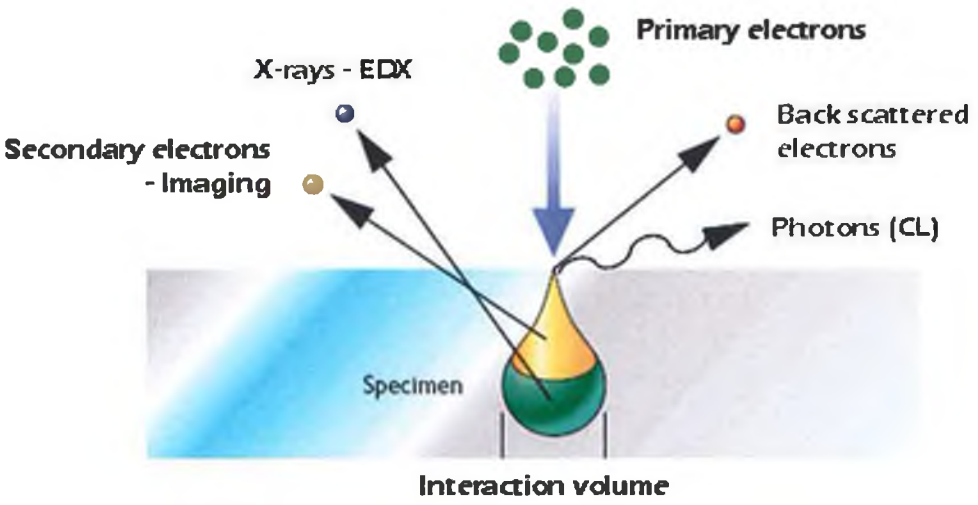

Figure 2.9. Schematic of the various signals generated by the interaction of electron beam with the sample

By detecting the signals coming out of the sample with suitable detectors, a range of information can be extracted. Therefore, in addition to the basic surface imaging facility (using the secondary electrons), SEM can also be used for several specific applications including compositional (using the out coming X-rays) and cathodoluminescence analyses (using the outcoming photons) with relevant additional detectors equipped in a basic SEM. A schematic of the scanning electron microscope (with CL and X-ray detectors) that is used for our experiments is shown in figure 2.10.

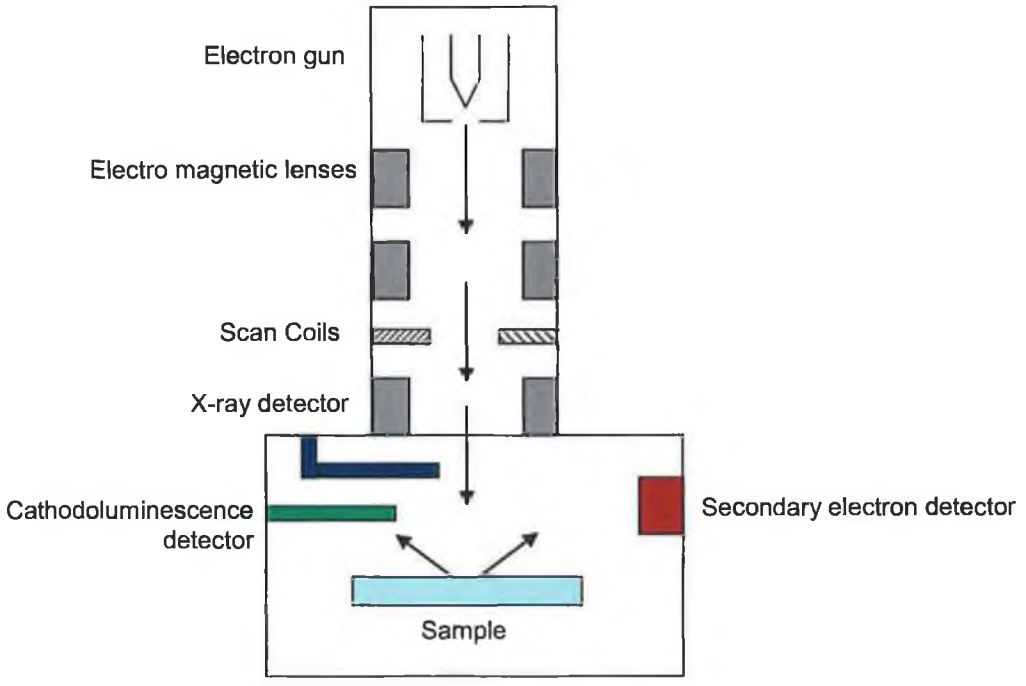

Figure 2.10. Schematic of an SEM system with EDX and CL attachments

e) Energy-Dispersive X-ray analysis

An energy-dispersive X-ray spectrometer (EDX) detects X-rays from the sample excited by a highly focused, high-energy primary electron beam penetrating into the

sample. When high-energy electrons interact with the atoms of material in the "interaction volume", they generate characteristic X-rays which are the fingerprints of individual elements present in the sample. Because the intensity of the individual X-ray is related to the quantity of the "parent atom" in the interaction volume, quantitative elemental analysis can be performed with the aid of a suitable software. If known standards are available, the quantitative analysis of the sample can be based on a comparison of spectral lines with the standards. Compositional analyses of CuCl samples were performed with a Princeton Gamma Tech energy dispersive X-ray analyzer attached to SEM with a Si (Li) detector. Film composition was analyzed relative to that of the target with a normalized accelerating voltage of 14.5 keV and a probe current of 3 nA. EDX data were quantified using the ZAF method whereby the atomic number (Z), absorption (A) and fluorescence (F) effects were taken into account. The accuracy thus achieved was better than ± 2 % relative.

f) Cathodoluminescence

Cathodoluminescence is the light emission associated with the excitation of materials by an electron beam. It occurs when a high energy electron beam impinges on the sample, where the electrons promote from the valence band into the conduction band, leaving behind a hole. When an electron and a hole recombine, it is possible for a photon to be emitted. The optics of a scanning electron microscope can be utilized to produce a focused beam and to excite a small region of the sample. The beam diameter in the SEM is of the order of a few nanometers. The light emitted from the sample is captured by a parabolic mirror, and a spectrum is obtained using a grating

and a high efficiency light detector. Room temperature cathodoluminescence studies were performed using an electron beam of 4 keV and probe current of 15 nA. The luminescence was collected by a parabolic mirror placed approximately 1 mm above the sample. The signal collected was then transferred onto a Gatan MonoCL instrument equipped with a 1200 lines/mm grating. The spectral resolution was approximately 0.1 nm.

g) Photoluminescence

Photoluminescence (PL) is similar to that of cathodoluminescence except the excitation is done optically using a laser. When light of sufficient energy is incident on a material, photons are absorbed and electronic excitations are created. Eventually, these excitations relax and the electrons return to the ground state. If radiative relaxation occurs, the emitted light is called PL.

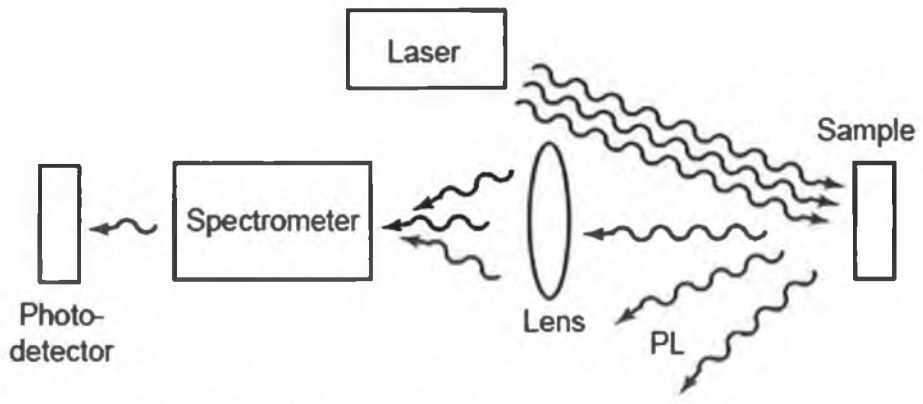

Figure 2.11. Schematic of the PL experimental set up

This light can be collected and analyzed to yield a wealth of information about the photo-excited material. The PL spectrum provides the transition energies, which can

be used to determine electronic energy levels. The PL intensity gives a measure of the relative rates of radiative and non-radiative recombination. Variation of the PL intensity with external parameters like temperature can be used to characterize further the underlying electronic states and bands. Schematic of the experimental set up for PL is shown in figure 2.11. Photoluminescence analyses of the films were performed in the temperature range of 20 K to room temperature. Photo-excitation, at 244 nm, was provided with an Innova Ar ion laser. A Jobin Yvon-Horiba, Triax 190 spectrometer with a spectral resolution of 0.3 nm, coupled to a liquid nitrogen cooled CCD, was used to record the photoluminescence spectra.

h) UV/Visible spectroscopy

Ultraviolet and visible (UV-Vis) absorption spectroscopy is the measurement of the attenuation of a beam of light after it passes through a sample or after reflection from a sample surface. It probes the electronic transitions of molecules as they absorb light in the UV and visible regions of the electromagnetic spectrum. When light (UV or visible) is absorbed by valence electrons, they are promoted from the ground state to excited state. This absorption corresponds to a wavelength, absorption band which is observed at 200-900 nm in the UV and visible range of detection. Absorption measurements can be at a single wavelength or over an extended spectral range.

a)

b)

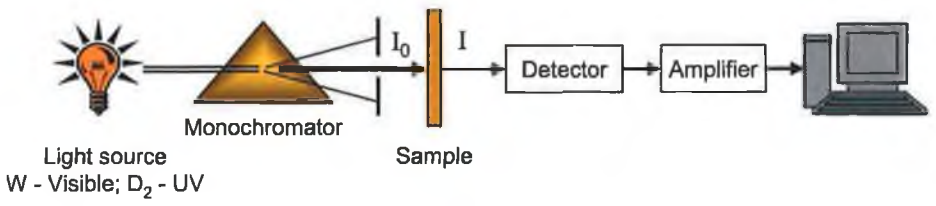

Figure 2.12. (a) Photograph and (b) schematic of a UV-Visible spectrophotometer

A Perkin Elmer Lambda 40 spectrometer (Figure 2.12a) was used for analyzing the optical properties of CuCl samples and its schematic is shown in figure 2.12b. A deuterium lamp is used as a UV source and a tungsten lamp is used for getting visible light. This spectrometer compares an uncoated glass slide and the CuCl film on glass and gives the absorption/transmittance spectrum of CuCl. If the intensity of the incident beam is I_0 and the intensity of the beam transmitted through the sample is I, transmittance and absorbance may be presented as $T = I/I_0$ or $A = \log_{10} I_0/I$. The resolution of the instrument is 0.5 nm.

i) Electrical studies

Preliminary electrical studies are carried out in order to understand the charge carrier transport mechanisms in CuCl films and also to measure film resistivity. The schematic of the electric circuit used in our experiments is shown in figure 2.13. Gold layers were evaporated on both sides of Si/CuCl structure as electrodes. A spring loaded probe station was designed and used for measurements to avoid damaging of the surface layer.

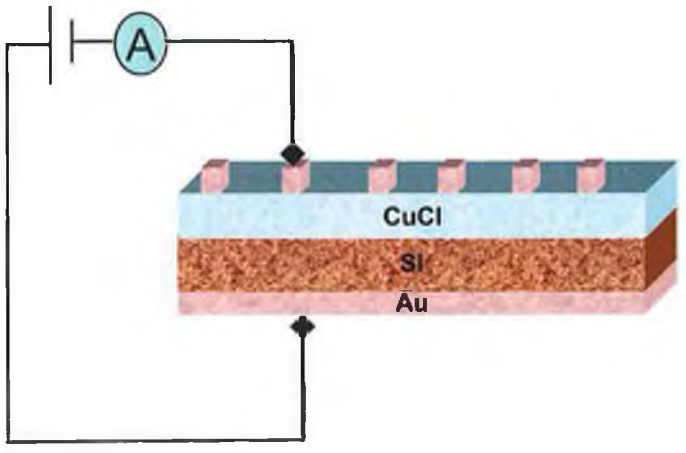

Figure 2.13. Schematic of a CuCl/Si structure for electrical characterization

A Keithley 617 instrument with a built in voltage source was used to measure the electric current through the sample. Voltage across the sample was increased in the steps of 0.05 V with 5 seconds hold on time on each increment. Automated IV measurements were performed using LabVIEW software interfaced with the Keithley electrometer.

Chapter 3

STOICHIOMETRY CONTROL OF SPUTTERED CuCl

Controlling the stoichiometry in the deposited films is essential, as the chemical composition has a significant role in determining the UV emission properties. In sputtered thin films, stoichiometry can be controlled by varying the sputtering parameters. Films with composition close to stoichiometry were achieved by varying target to substrate distance (d_{ts}) and substrate bias potential (V_b) is used to further tune the stoichiometry. The influence of stoichiometry on the film properties such as structural and optoelectronic properties was analyzed. Based on these studies, optimum conditions to deposit stoichiometric, high optical quality samples were determined.

3.1 Optimization of stoichiometry using target to substrate spacing

The spacing from the target to substrate was found to have a strong influence on the film properties in our studies. This spacing was varied from 3 cm to 9 cm and the properties of all the samples were thoroughly investigated. Figure 3.1 shows the variation in the Cu/Cl ratio of the film, obtained from EDX analysis, as a function of target to substrate spacing. Film composition was analyzed relative to the target with an accelerating voltage of 14.5 kV and a probe current of 3 nA. A spacing of 3 cm from the target to substrate yields highly non-stoichiometric (i.e. chlorine rich) films. The film composition drastically varies when the target to substrate distance is increased from 3 cm to 4.5 cm and nearly stoichiometric films were obtained when d_{ts} is increased to 6 cm.

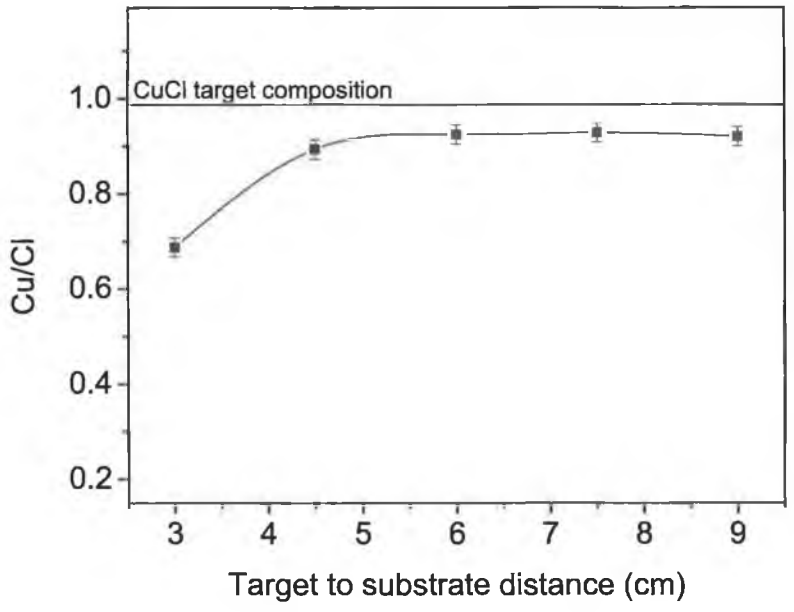

Figure 3.1. Influence of target to substrate spacing on the film composition (Determined by EDX analysis). Note: The solid line is only a guide to the eye.

There was no noticeable variation observed in the stoichiometry for further increase in the spacing beyond 6 cm, i.e. the films deposited at the positions 6, 7.5 and 9 cm from the target were found to have compositions close to that of stoichiometry. These experiments were performed several times to establish the veracity of the results.

EDX is a versatile technique that provides quantitative details about the elemental composition; however a limitation of EDX is that one cannot get the information regarding the chemical state of the elements present in the sample. On the other hand, XPS is a powerful tool that can extract the chemical states of the elements by a detailed examination of the shift in binding energy corresponding to the core-level transitions. One of the chlorine rich samples (deposited at d_{ts} = 3 cm) and stoichiometric samples (deposited at d_{ts} = 6 cm) were taken for XPS analysis to examine the oxidation states of the elements. Cu $2p_{3/2}$ core level XPS spectra of the samples deposited with 3 cm and 6 cm target to substrate spacing are shown in figure 3.2. One can observe a noticeable difference in the peak widths and also peak positions between the spectra given.

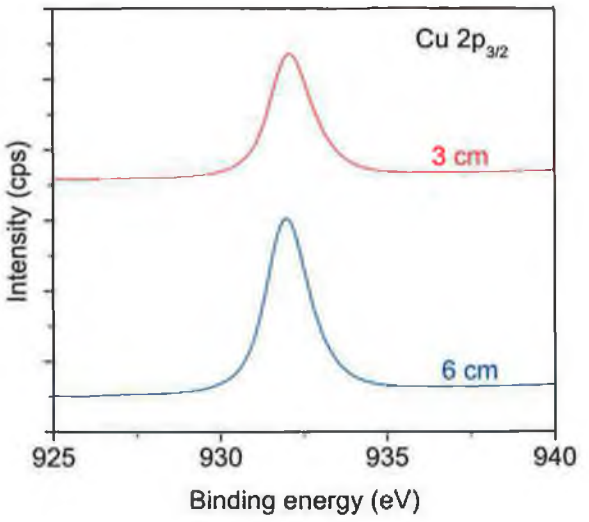

Figure 3.2. Cu 2p3/2 core level XPS spectra of CuCl thin films for d_{ts} = 3 and 6 cm

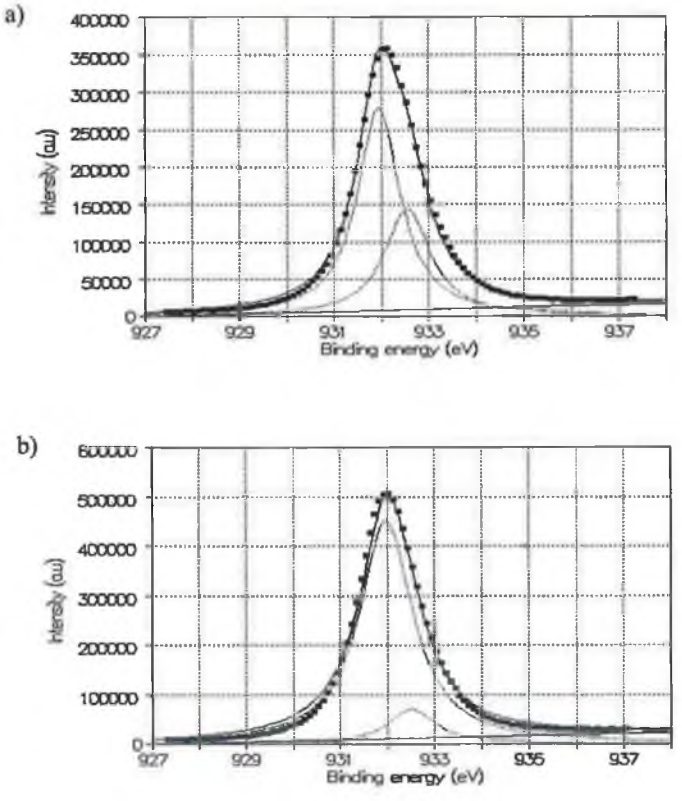

Figure 3.3. Deconvoluted Cu 2p3/2 peaks of samples with target to substrate distance d_{ts} = 3 and 6 cm

A shift in binding energy towards higher values confirms the presence of a higher oxidation state of an element. A closer look at the deconvoluted (using Peakfit software) spectra (see figure 3.3) reveals that there are two distinct peaks at the binding energies of 931.94 eV and 932.55 eV. Figure 3.3a clearly shows the presence of a mixture of more than one oxidation state of copper in the sample deposited at d_{ts} = 3 cm. The lower binding energy peak is due to the copper in stoichiometric CuCl and the peak at higher binding energy is due to the higher oxidation state of Cu in Cl rich phase. The Cu $2p_{3/2}$ core level spectrum of the sample deposited at 6 cm target to substrate spacing (see figure 3.3b) is mostly dominated by the peak centered at 931.97 eV. Hence it can be concluded from the XPS studies that a considerable amount of $CuCl_2$ phase is present in addition to CuCl for the samples deposited with 3 cm target to substrate spacing, whereas CuCl is the predominant phase in the samples deposited with 6 cm target to substrate distance.

a) Stoichiometry and structural properties

The structural properties were investigated using X-ray diffraction analysis. Due to the fact that CuCl and Si has a very close lattice match, the diffraction angles in an XRD spectra appears at the same position for both lattices. For example, the most intense (111) diffraction of CuCl appears at $2\theta \sim 28.46^{o}$, which is 28.5^{o} for Si. Such close matching makes it difficult to distinguish the diffraction of CuCl from that of Si. X-ray diffraction spectra measured using θ-2θ geometry for films deposited on a glass substrate with different d_{ts} is shown in figure 3.4.

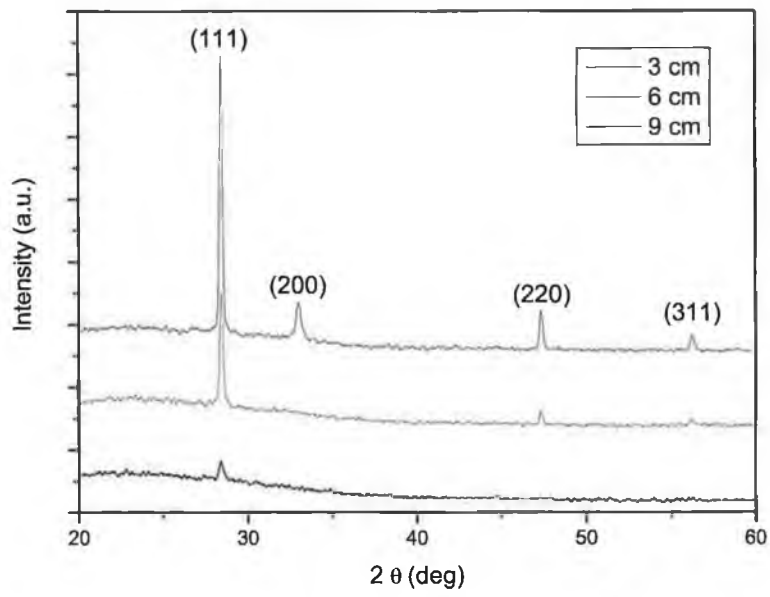

Figure 3.4. XRD spectrum of CuCl film on glass deposited with different target to substrate spacings

The most intense peak appears at $2\theta \sim 28.46^{o}$ corresponds to (111) plane. The other two less intense peaks centered at $\sim 47.44^{o}$ and 56.27^{o} correspond to the (220) and (311) planes. These observed diffraction peak positions are quite close to the bulk CuCl [104]. Figure 3.4 shows three characteristic peaks of cuprous chloride with zinc blende cubic structure. Another noticeable feature is the appearance of (200) peak at 2θ~33 in the CuCl film sputtered at 3 cm from the target. This is normally not observed in the CuCl films evaporated on glass [94]. The appearance of (200) peak in the Cl rich sample is not understood at present. It can not be related to the defect/disorder in the sample since this diffraction is also seen in bulk single crystal.

A comparison between the experimentally measured diffraction parameters for the sputtered CuCl films (d_{ts} = 6 cm) and the bulk CuCl is shown in Table 3.1. It is very interesting to note that the intensity ratio of the reflection peaks is completely different from that of bulk CuCl. The reflections due to (220) and (311) planes are suppressed when compared to the reported values (for bulk CuCl) [47]. Also there is no trace of growth along <200> direction, which is present in the diffraction of the bulk CuCl. The ratio of (111) peak with other reflections indicates that CuCl grows along <111> direction predominantly for the thin films deposited by sputtering. That is, the close-packed planes are perpendicular to the growth direction.

	JCPDS data (PDF No. 6-334)				**Experimental data**			
Plane (hkl)	111	200	220	311	111	200	220	311
2θ	28.55	33.02	47.44	56.29	28.45	-	47.44	56.27
Intensity	100	8	55	30	100	-	11	4
Lattice parameter (a)	5.4163 Å				5.4312 Å			

Table 3.1. Comparison of X-ray diffraction data of CuCl film deposited on glass with d_{ts}= 6 cm with JCPDS diffraction data for bulk CuCl.

It is well known that the crystalline quality is indicated by the width of the diffraction peak. Smaller width is an indication of the good crystalline quality [105]. Figure 3.5 shows the variation in FWHM of the (111) peak with the target to substrate distance in the nearly stoichiometric samples. The FWHM of (111) diffraction decreases for the sample with 6 cm d_{ts} and then it starts to increase with further increase in target to substrate spacing, indicating a degradation in the crystalline quality. The grain sizes

of the samples were calculated from the line width of the X-ray diffraction using Scherrer equation [105];

$$D = \frac{0.9\lambda}{\beta \cos\theta} \tag{3.1}$$

where, λ is the wavelength of the X-ray used (1.54 Å), β is the full width at half maximum and θ is the Bragg angle.

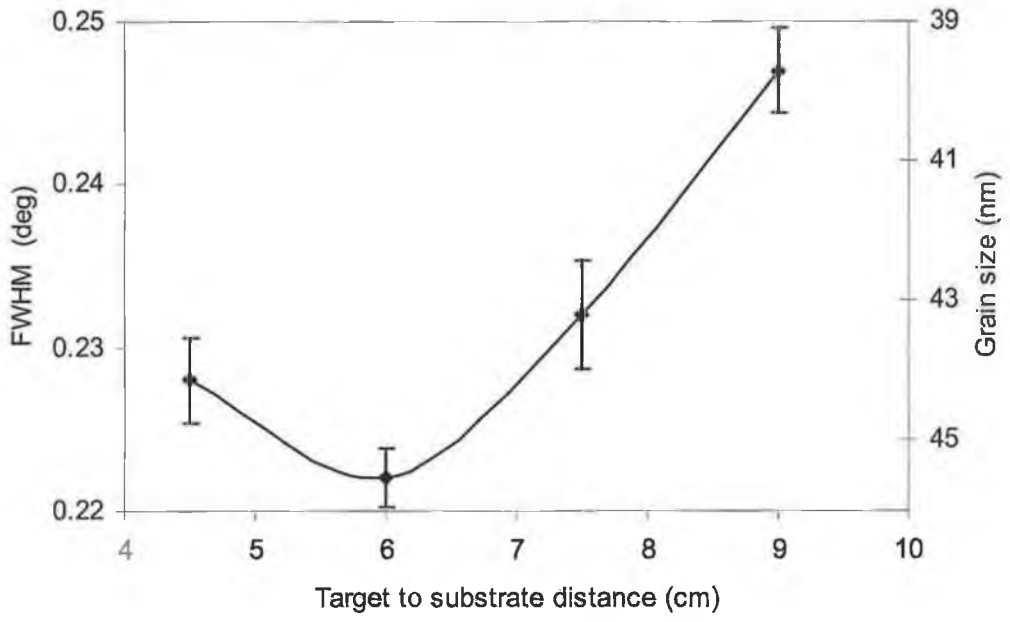

Figure 3.5. Variation in FWHM of (111) peak with target to substrate spacing. Variation in grain sizes are given in secondary y axis

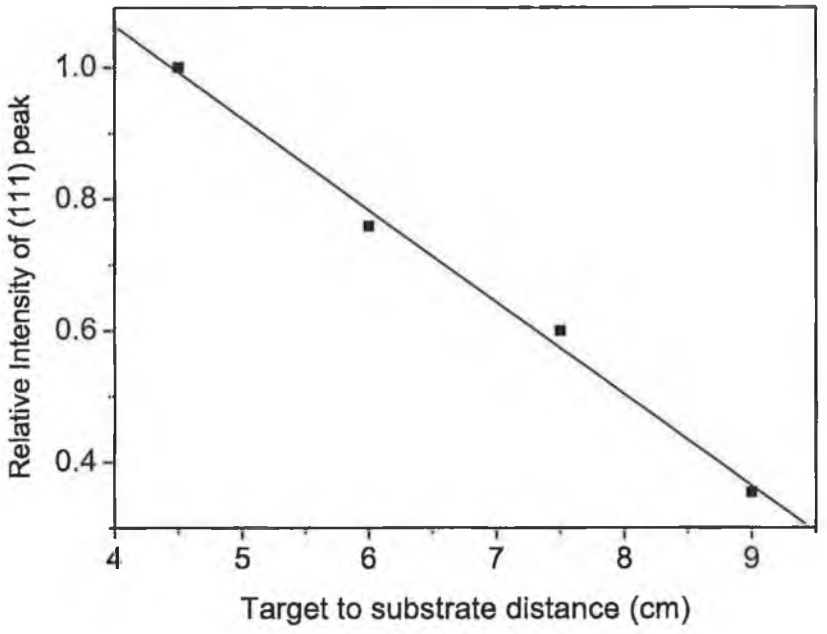

Figure 3.6. Variation in relative intensity of (111) peak with target to substrate spacing

The (111) diffraction peak intensities are plotted as a function of the target to substrate distance as shown in figure 3.6. The peak intensity gradually decreases with increased target to substrate distance. Note that the change in film thickness (typically caused by the change in deposition rate with the d_{ts}) will only contribute to a minor extent in the decrease in the diffraction intensity, as the film thickness variation was measured to be less than 15 % over the range of target to substrate distance. It is also interesting to note that the sample with 4.5 cm target to substrate spacing has a slightly higher diffraction peak intensity, but it has a higher FWHM than the sample with d_{ts} = 6 cm, indicating lower crystalline quality.

The kinetics of the formation of CuCl thin films is dependent on a number of factors including,

i) the intensity of fluxes of Cu, Cl and CuCl arriving at the substrate
ii) the sticking coefficient/sticking probability of the particles reaching the substrate
iii) angular distribution of the fluxes arriving at the substrates
iv) desorption of the atoms on the surface
v) mobility of the ad-atoms on the growing surface

The compositional variation for different target to substrate positions observed from EDX analysis can be explained as follows. The mean free path of the particles was calculated to be around 3.3 cm at a working pressure of 2×10^{-3} mbar. Mean free path was calculated from the following expression [106],

$$\lambda=\frac{RT}{\sqrt{2}\,\pi d^2 N_A P} \tag{3.2}$$

Where R is the universal gas constant, T is the temperature, d is the atomic radius, N_A is Avogadro's number and P is pressure.

When the substrate is kept within a mean free path length, the sputtered neutrals reach the substrate with high energy (almost with their initial energy) with few collisions. The energy distribution of the sputtered atom is usually assumed to obey the Thompson distribution [107] which is expressed by [108],

$$f(E)\,dE=C\left(1-\sqrt{\frac{U+E}{\gamma E_i}}\right)\frac{E}{(U+E)^3}dE \;;\; \gamma=\frac{4M_g M_t}{(M_g+M_t)^2} \tag{3.3}$$

where U is the binding energy of the target material, E_i is the average energy of the incident ions C is a normalization constant and γ is the fractional energy transfer from the projectile to the target atom. M_g and M_t are masses of projectile and target atoms respectively.

When the particles have higher energy they are more mobile on the substrate surface and it is more likely that free atoms will be desorbed. If the fluxes of Cu and Cl atoms from the target are equal, it is likely that any Cl atom on the surface will bond with the top layer as chlorine is highly electronegative (electronegativity of Cu and Cl is 1.90 and 3.16 Pauling units respectively) [109], whereas some Cu atoms may remain unbonded. These unbonded Cu atoms will more easily desorb from the substrate. This explains the presence of excess chlorine in the samples deposited with a target to substrate distance of ~3 cm.

When the substrate is kept closer to the target, the sputtered species have relatively higher mobility on the substrate surface as they undergo fewer collisions. As the substrate is moved away from the target, the particles start to lose their kinetic energy due to an increase in the number of collisions before reaching the substrate. Lower mobility of the sputtered particles can yield less crystalline films [110]. This is related to the increase in FWHM of (111) peak when the substrates are kept closer to the target. The loss of intensity can be explained by smaller grain size and high defect density for the films of poor crystallinity. Higher diffraction peak intensity but poor crystalline quality of the sample with d_{ts} = 4.5 cm can be related to the presence of

defects caused by slight compositional deviation (refer figure 3.1). Therefore, for our experimental set up, a target to substrate distance of 6 cm is considered to yield optimum structural quality samples.

b) Stoichiometry and optical properties

UV-VIS transmittance spectra of the samples deposited with target to substrate spacings of 3 cm and 6 cm are shown in figure 3.7. The sample deposited at d_{ts} = 3 cm (chlorine rich) has no clear absorption edge as a result of high non-stoichiometry.

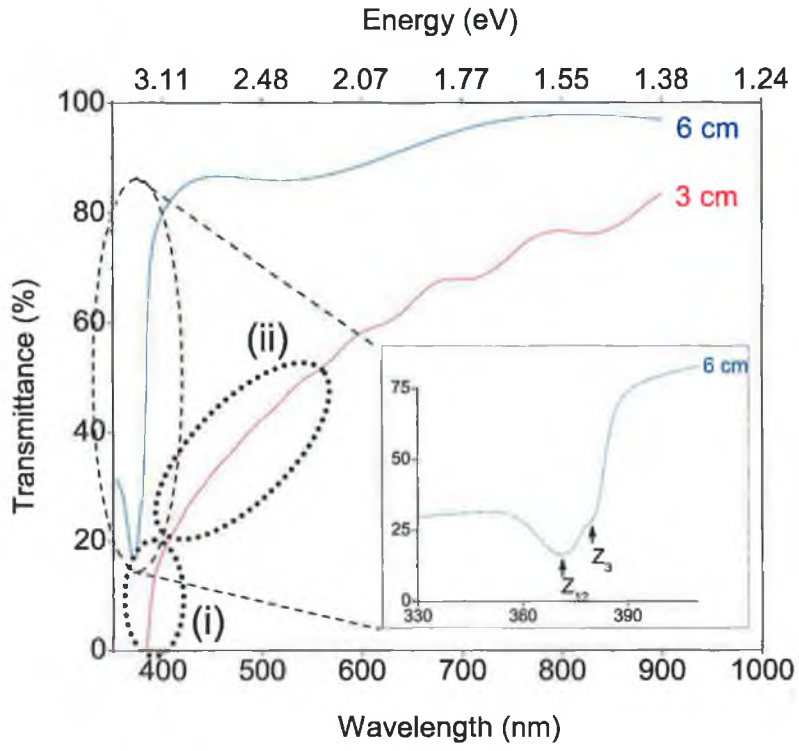

Figure 3.7. UV-VIS transmittance spectra of CuCl film on glass with target to substrate distance

The samples deposited with the target to substrate spacing more than 6 cm were fairly transparent (> 90 %) in the visible region and the spectrum for sample with d_{ts} = 6

cm is shown in the figure. The spectrum shows two Mott-Wannier exciton peaks at 372 nm and 382 nm which are Z_{12} and Z_3 excitons respectively, and this is given in the insert of figure 3.7. Z_{12} is made up of a Γ_8 hole and a Γ_6 conduction electron and Z_3 exciton has a hole from Γ_7 state and an electron from Γ_6 state [53,62]. These exciton peak positions are in good agreement with previous reports [111,112]. The sample deposited at d_{ts} = 3 cm (chlorine rich) does not reveal any excitonic feature such as seen in stoichiometric films. Also it has no clear absorption edge as a result of high non-stoichiometry. In the spectrum, there are two different absorption trends in different regions (see the spectral regions marked in figure 3.7); (i) absorption in the UV region from around 385 to 410 nm and (ii) absorption in the visible region from 410 nm. The UV absorption originates from the CuCl phase as a result of band edge effects, and the visible absorption can be due to the non stoichiometry. Also, it was found that the UV absorption in the non-stoichiometric film is red shifted compared to the stoichiometric samples.

Figure 3.8 shows the room temperature cathodoluminescence spectra of samples deposited at d_{ts} = 3 cm (Cl rich) and d_{ts} = 6 cm (nearly stoichiometric). There are two noticeable features in the CL spectra; (i) strong and sharp excitonic emission in UV and (ii) a broad emission in the green spectral region. UV emission appearing around 3.2 eV (at 385 nm) is due to Z_3 excitonic mediated recombination and the green emission at ~ 515 nm is due to deep levels present in the sample.

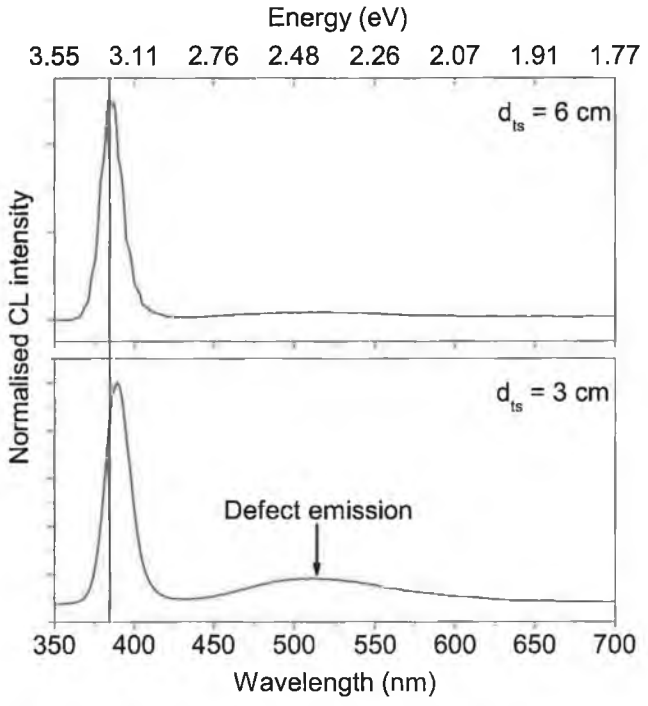

Figure 3.8. Room temperature CL spectrum of CuCl films deposited at d_{ts} = 3cm and 6 cm

The chlorine rich sample has differences in both of these emissions comparing to that of the stoichiometric sample. First, the UV excitonic emission is red shifted to 30 meV. It can be recalled that this red shift was also observed in the UV absorption in the transmittance spectra. The second difference is that the ratio of UV emission to green emission (I_{UV}/I_{GE}) is much lower than the stoichiometric sample.

Sub-band gap emission such as that seen in the chlorine rich samples is generally considered to originate from non-stoichiometry and/or defects. Deep level emission originating from non-stoichiometry is reported by several authors [113,114] for UV emitting ZnO thin films. It is reported to be caused by different intrinsic defects such

as an oxygen vacancy (V_O), a zinc vacancy (V_{Zn}), interstitial zinc (I_{Zn}), etc. [115,116,117,118]. The fact that this green emission increases markedly for Cl rich samples suggests that it originates from non-stoichiometry and structural defects. The FWHM of the Z_3 emission peak from Cl rich and nearly stoichiometric samples were 20 and 16.1 nm, respectively. Line broadening and the increase in deep level emission shows the optical degradation of the film when the film composition deviates from stoichiometry.

3.2 Fine control of stoichiometry using substrate bias

The samples sputtered with the target to substrate spacings less than 6 cm were non-stoichiometric. For target to substrate distance more than 6 cm, the deposition results in loss of crystalline quality. Hence a target to substrate distance of 6 cm is chosen as an optimum distance for depositing CuCl films with better compositional, structural and optoelectronic qualities. In order to achieve further improvement in the stoichiometry, the bias potential to the substrate was varied, while keeping the T-S spacing at 6 cm. Substrate bias was given using an RF power supply through a matching circuit.

a) Influence of substrate bias on stoichiometry

Figure 3.9 shows the variation in the Cu/Cl ratio (obtained from EDX analysis) on increasing the negative substrate bias up to -62 V. The film deposited without any substrate bias is chlorine rich ($CuCl_{1+x}$) and the chlorine content decreases upon

making the bias more negative. Stoichiometric CuCl films were obtained at a bias of -22 V. The films become chlorine deficient (i.e. copper rich $CuCl_{1-x}$) for further increases in the negative substrate bias.

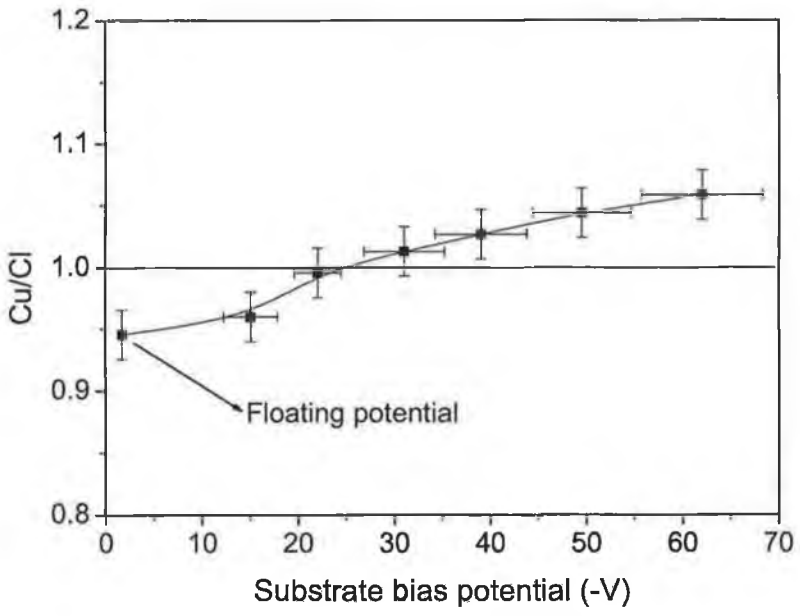

Figure 3.9. Variation of Cu/Cl ratio with substrate bias

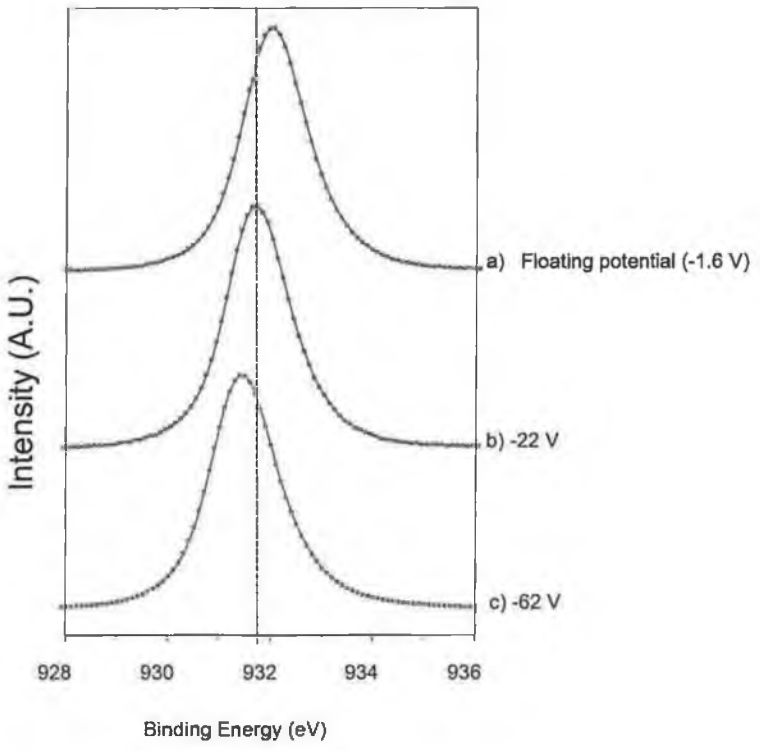

Figure 3.10. Cu 2p3/2 spectra of samples with different substrate bias

In addition to EDX, the samples were also subjected to XPS analysis in order to confirm the change in composition with the applied substrate bias. Cu $2p_{3/2}$ core level spectra of the samples deposited at various substrate bias were compared as shown in figure 3.10. It is clearly evident that the spectral peak position shifts towards lower binding energy for the sample deposited at -22 V bias, compared to that deposited at floating potential. A further shift in the same towards lower binding energy is observed when the negative bias is increased to -62 V. In principle, a shift towards lower binding energy indicates a decrease in the positive charge of the atom [119]. In the present case, a shift towards a lower binding energy indicates a decrease in the positive charge on Cu. This reveals that there is a decrease in the chlorine content on

varying the bias from floating potential to -62 V. Hence, the shift in the core level spectral emission of Cu $2p_{3/2}$ towards the lower binding energy on the increase in negative substrate bias confirms the trend seen from EDX analysis.

b) Influence of stoichiometry on film properties

To investigate the influence of chemical composition on the structural and optical properties, X-ray diffraction and optical absorption spectroscopic analyses were performed. Figure 3.11 shows the variation of the full width at half maximum (FWHM) of (111) diffraction intensity and the Z_3 optical absorption intensity as a function of Cu/Cl ratio.

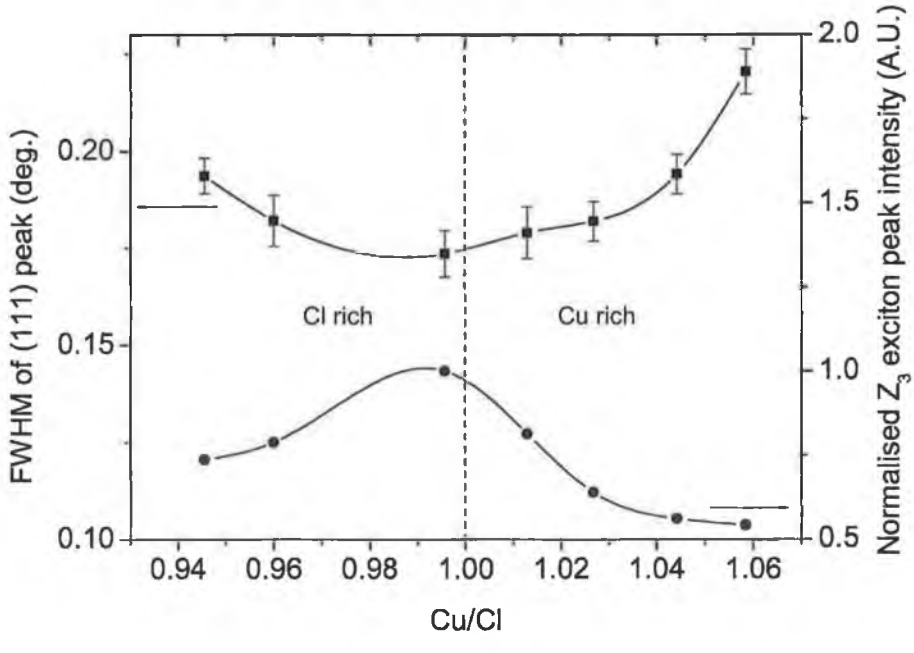

Figure 3.11. Variation in the FWHM of XRD (111) peak and Z_3 exciton peak with Cu/Cl ratio

The FWHM of the (111) diffraction peak is smaller and Z_3 optical absorption is higher when the Cu/Cl ratio is 1, which indicates that the stoichiometric sample has good crystalline and optical quality. The sample quality is degraded with deviations from stoichiometry. This plot also indicates that there is a correlation between the microstructure and the optical properties.

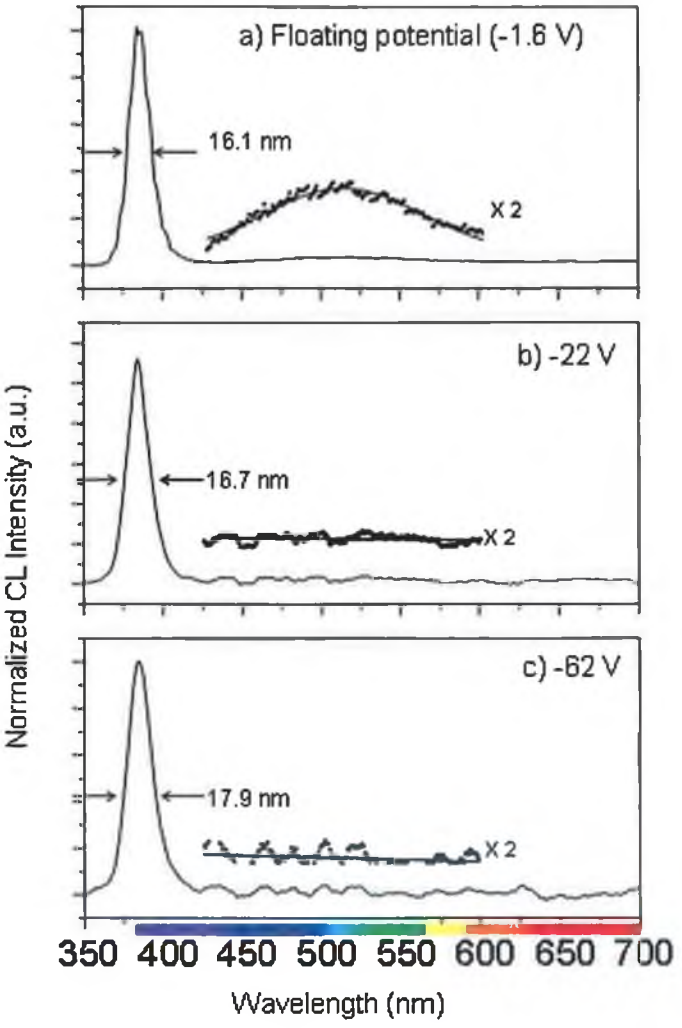

Figure 3.12. CL spectra for the samples with different substrate bias voltages

Figure 3.12 shows the room temperature cathodoluminescence spectra of Cl rich, stoichiometric and Cu rich samples. An intense UV emission appears at a wavelength of around 385 nm due to Z_3 excitonic mediated recombination for all the three samples. The optical quality of the films can be assessed based on two important properties: i) the width of the Z_3 exciton emission and ii) the existence of deep level green emission. A smaller FWHM of the Z_3 emission and absence of any deep level emission represents the higher optical quality. In the Cl rich samples (deposited at floating potential), a green emission centered at ~ 515 nm is observed in addition to the exciton emission. In the stoichiometric and Cu rich samples, there is no trace of the abovementioned green emission, and the exciton emission is the only feature observed.

A noticeable increase in the FWHM for Cu rich samples indicates the degradation of optical quality. Although the Cl rich sample has a smaller FWHM for Z_3 emission, it suffers from the deep level emission from non-stoichiometric defects, whereas, the stoichiometric sample has a strong UV emission without any deep level emission indicating its high optical quality and low defect density. This green emission is only seen in the Cl rich samples whereas it is not observed in the stoichiometric and Cu rich samples. Hence, it is suggested that copper vacancies or chlorine interstitials could be the origin of the green emission observed in the CL spectra. The FWHM of the Z_3 emission peak from Cl rich, stoichiometric and Cu rich samples were 16.1, 16.7 and 17.9 nm, respectively

It is interesting to investigate the variation in composition with the substrate bias, as biasing results in a selective removal of chlorine. When the substrate has only floating bias applied (approximately -1.6 V), the growing film is Cl rich and biasing reduces the Cl content. Applying a negative bias to the substrate induces an intentional ion (argon) bombardment on the growing surface. Increasing the negative bias increases the energy of the ions impinging on the film surface. Any displacement or desorption of particles on the film surface depends on the energy transfer in a collision and, thereby, on the masses of the projectile and surface particles. A large displacement yield is obtained, if the mass of the projectile matches the mass of the surface particle, because the transfer of energy is high [120]. Among the surface particles; Cu and Cl, the mass of Cl is closer to that of the projectile (argon); hence, a larger surface displacement yield is expected for Cl. This could be related to the decrease in Cl content on biasing the substrate. Increasing the bias voltage results in desorption of a higher number of Cl atoms from the film surface. Therefore, the film composition progresses towards the stoichiometry with increasing the negative bias, and the films become Cu rich for a further increase in the negative bias.

3.3 Summary

The target to substrate distance and substrate bias were found to have a very strong influence on the sputtered film properties including composition, crystallinity and also UV emission. Samples deposited with $d_{ts} < 6$ cm were Cl rich. The film crystallinity gradually decreased for $d_{ts} > 6$ cm. Nearly stoichiometric CuCl films were deposited at a distance of 6 cm. The film stoichiometry was then finely tuned by

adjusting the substrate bias. The chemical stoichiometry has a strong correlation with the crystalline and optical qualities of the films. Cathodoluminescence showed a strong UV exciton emission and a green emission from deep levels for Cl rich samples. This deep level green emission could be eliminated on attaining stoichiometric or copper-rich films. Stoichiometric samples were found to have the highest optical quality. As the elemental content can be finely controlled using substrate bias, it may therefore be possible to vary the intrinsic doping levels and so tune the electrical properties of the material.

Chapter 4

MICROSTRUCTURE CONTROL AND IT'S INFLUENCE ON FILM PROPERTIES

In the device point of view, the effect of microstructure on the optoelectronic properties is very important. Imperfections such as dislocations and defects play an important role as non-radiative recombination centers which are mainly attributed to near surface and grain boundaries. Optimizing the growth parameters is one of the key factors in obtaining high optical quality films. The influence of the working pressure on the micro-structural and optoelectronic properties is investigated in detail. The optoelectronic properties are studied using cathodoluminescence spectroscopy, mainly considering the existence of meso and nanostructural interfaces within the thin film.

4.1 Influence of sputtering pressure on surface mobility

The target to substrate distance was kept at the optimum distance of 6 cm from the previous experiments. To analyze the influence of working pressure on the film properties, Ar pressure was varied from 1.1×10^{-3} mbar to 1×10^{-2} mbar. The composition and the structural properties were studied and the influence of microstructure on the optoelectronic properties was analysed using cathodoluminescence spectroscopy. The compositions of the samples deposited at the sputtering pressures ranging from 1.1×10^{-3} mbar to 1×10^{-2} mbar were analyzed using EDX. All of the films were nearly stoichiometric, and a change in the working pressure had no major influence on the film stoichiometry. A typical EDX spectrum obtained from a sample deposited at 1.1×10^{-3} mbar is shown in figure 4.1. In addition no impurity elements were detected in the samples.

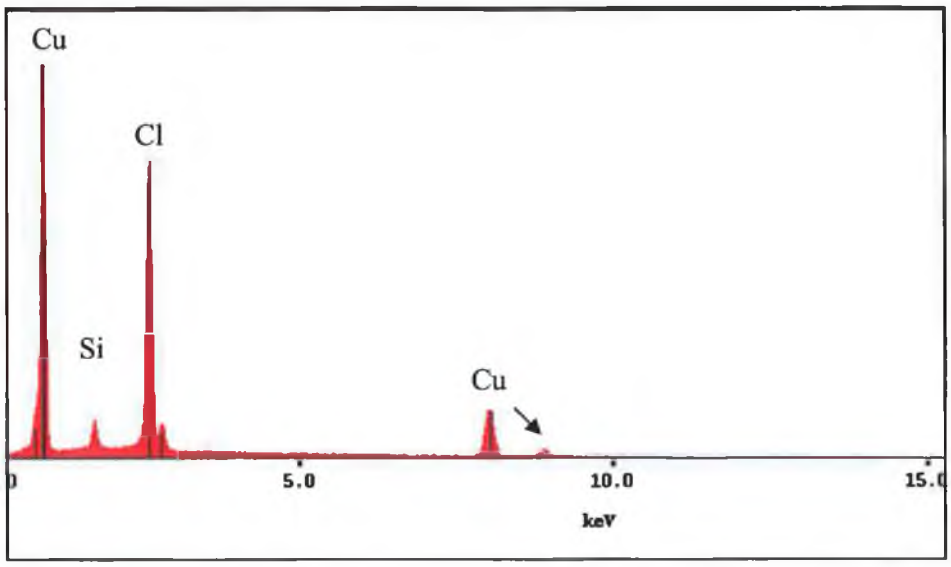

Figure 4.1. A typical EDX spectrum of a CuCl film deposited at a sputtering pressure of 1.1×10^{-3} mbar

Figure 4.2 shows the XRD spectra of the samples deposited at different sputtering pressures. The most intense peak observed at $2\theta = 28.46^0$ corresponds to the (111) diffraction of CuCl. The <111> direction is the preferred growth orientation for a cubic lattice, since it has the lowest surface free energy [121]. As seen in figure 4.2, the intensity of the (111) diffraction decreases as the sputtering pressure increases. The full width at half maximum (FWHM) of the diffraction peak is a measure of the crystalline quality of the samples [101]. From the XRD spectra of the samples, the FWHM of (111) diffraction peaks were measured and plotted as a function of the sputtering pressure (Figure 4.3).

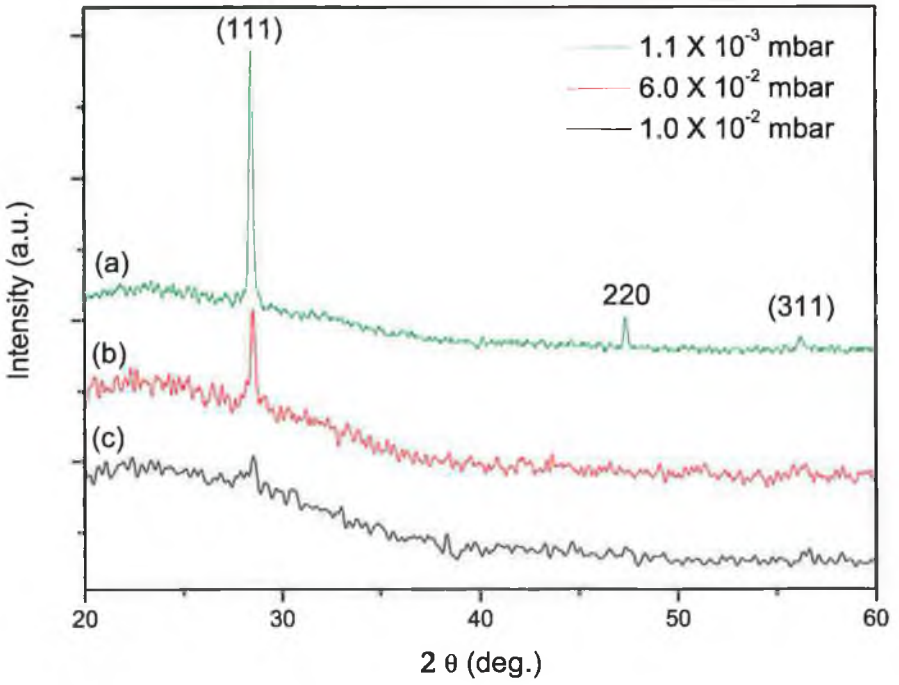

Figure 4.2. XRD spectra of CuCl films deposited at different sputtering pressures: a) 1.1×10^{-3} mbar, b) 6×10^{-3} mbar and c) 1×10^{-2} mbar.

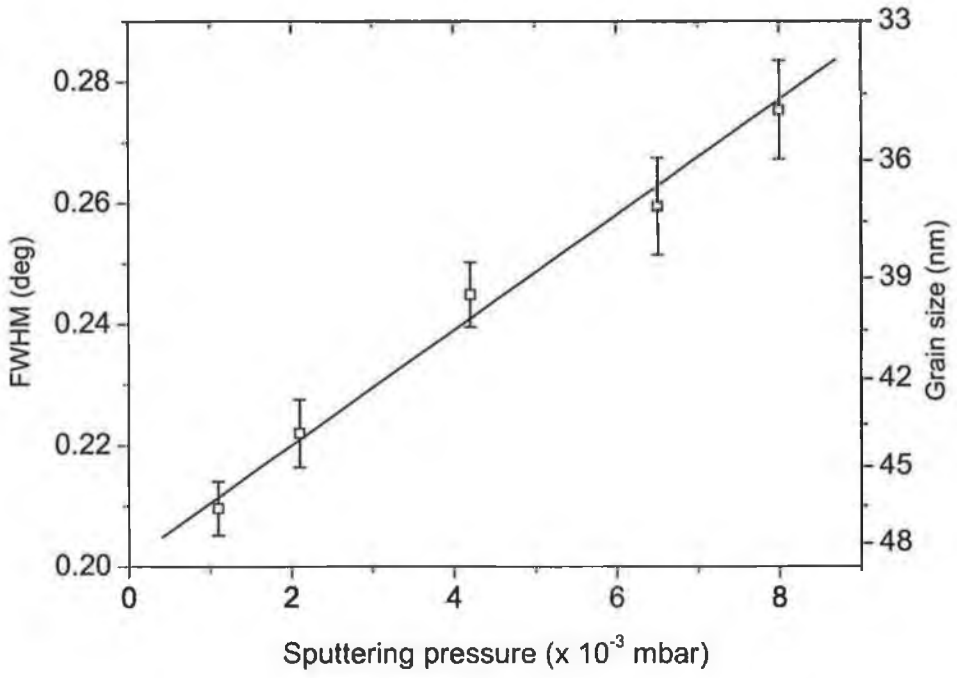

Figure 4.3. Variation in the FWHM of XRD (111) peak for the films deposited at different sputtering pressure. Variation in grain size is given in secondary y axis

The variation of the FWHM value indicates the grain size of the samples decreases linearly with the increase in sputtering pressure. The average crystallite sizes were found to be approximately 40 and 30 nm for the samples deposited at 1.1×10^{-3} and 1×10^{-2} mbar, respectively.

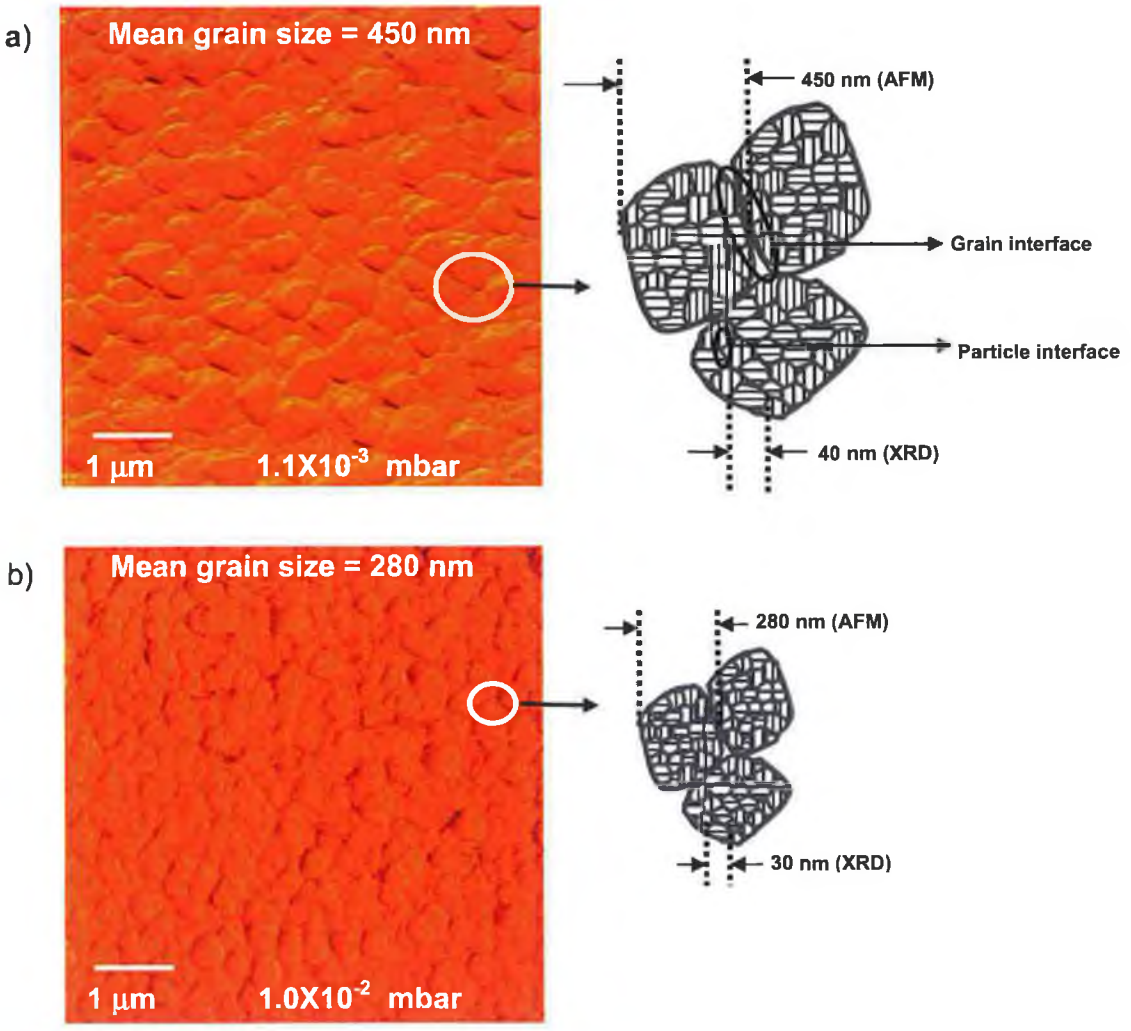

Figure 4.4.AFM topograph of the sample deposited at 1.1×10^{-3} and 1×10^{-2} mbar, Also shown is the schematic of sub-grains for each sample

The AFM topographs of the same set of samples are shown in figure 4.4. The images show that the samples consist of particles with mean sizes of around 450 and 280 nm for those deposited at 1.1×10^{-3} and 1×10^{-2} mbar respectively. It is interesting to note that the grain size seen in AFM is much greater than the grain size deduced from XRD analysis. Therefore the grains observed in AFM topography could be considered as polycrystalline domains consisting of clusters of nano-crystallites.

Hence there are two types of interfaces viz., particle-particle and grain-grain are expected as shown in figure 4.4. The surface to volume ratio (S/V) of the grains increases as the particle size decreases, accompanied by an increase in grain boundary area. Hence, when the sputtering pressure is increased, the overall interface area (particle and grain) in the sample increases.

4.2 Impact of grain interface on UV emission

Figure 4.5 shows the room temperature CL spectra of the samples deposited at various sputtering pressures. A very strong UV emission appears at $\lambda \sim 385$ nm, which is due to the recombination governed by Z_3 excitons. A broad green emission centered at ~ 515 nm is also observed. Sub-band gap emission such as this is generally considered to originate from deep level impurities, defects and non-stoichiometry. As discussed in the previous chapter, similar deep level emission is reported by several authors [110,111] for UV emitting ZnO thin films.

There is a variation in the FWHM of the Z_3 peaks from 16 to 18 nm with the increase in sputtering pressure. There is also a substantial decrease observed in the intensity ratio of the UV exciton peak to the green emission peak (I_{uv}/I_{ge}) for the samples deposited at higher sputtering pressures.

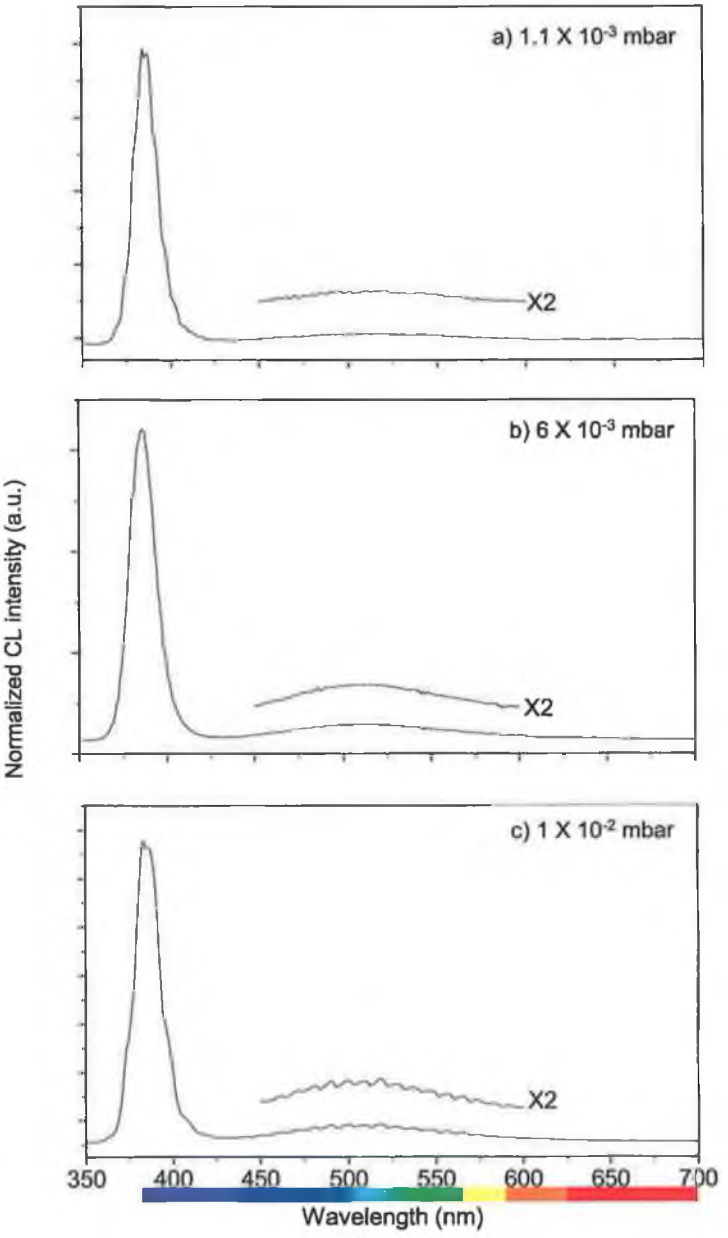

Figure 4.5. CL spectra taken at RT of the samples deposited at different sputtering pressures

The small FWHM of the exciton peak and the high value (~ 30) of I_{uv}/I_{ge} indicate the high optical quality of the samples. Hence it is clear from the CL analysis that the excitonic UV emission increases with the decrease in grain interface area. Therefore

the lower working pressure of 1.1×10^{-3} mbar is found to be optimum for producing better optical quality CuCl thin films.

Origin of grain interface

Since the grain interface has a significant influence on the optical properties, it is interesting to analyse the origin of the interface. The microstructural properties are influenced by the growth mechanisms of the films on the substrate surface. The film growth depends on several factors including the energy of the adatoms, substrate temperature, properties of the substrate and the substrate-film interface structure and energy. The formation of crystalline films can have,

i) a higher nucleation rate and/or

ii) faster grain growth,

depending on the growth environment.

When the energy of the incoming particles to the substrate is lower, the particles are just adsorbed on the substrate surface as they are less mobile. These particles do not actively contribute to the grain growth by surface diffusion after nucleation on the growing surface. This favours the formation of a large number of nuclei rather than the spread of the existing nuclei by coalescing with the neighbouring ones. On the other hand, when the energy of the particles is higher, the particles are mobile enough to diffuse across the substrate surface and be captured by an existing nucleus. This speeds up grain growth and hence grain growth is more favourable in this case.

At lower working pressures (1.1×10^{-3} mbar), the arriving particles are more mobile as they undergo a fewer collisions, favouring the grain growth, resulting in a film with larger grains (figure 4.4a). In contrast to this, at higher working pressures (1×10^{-2} mbar), the sputtered particles reaching the substrate are less energetic as they undergo a greater number of collisions in the plasma. This is illustrated in figure 4.6. Therefore the film growth has a higher nucleation density and the grown films consist of a larger number of smaller grains (figure 4.4b).

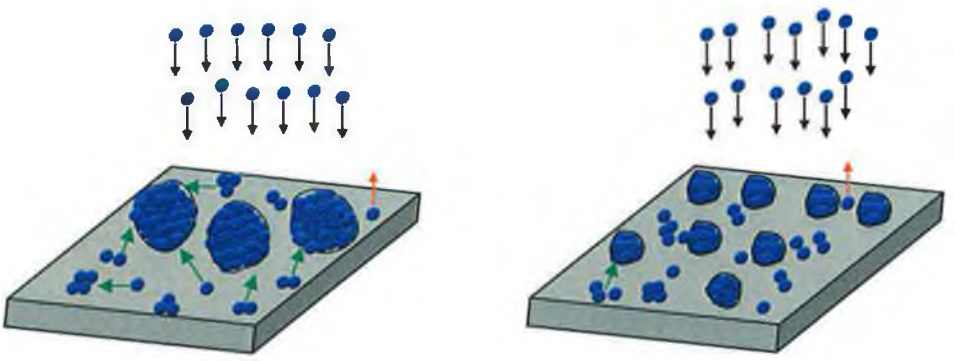

Figure 4.6. Schematic of atomic mobility and grain growth at lower and higher sputtering pressure

Grain boundaries are interfacial defects that are rich in,

i) structural disorder,

ii) impurity segregation, and,

iii) non-stoichiometry.

Hence it is suggested that structural disorder at the grain interface could be the origin of the green emission seen in CL spectra. When the size of the nanocrystallites

decreases, the grain boundary area increases as the S/V ratio increases. Non-radiative recombination centres and the deep level emission centres for green emission should increase in prevalence as the grain size decreases resulting in a degradation of the optical quality of the samples.

4.3 Correlation between structural and optical properties

From the CL analysis, a strong dependence of the intensity ratio between the excitonic emission and defect emission on the grain interface area has been observed. Furthermore, to confirm the influence of the microstructure on the optical properties, the samples were analysed with the UV-VIS spectroscopy.

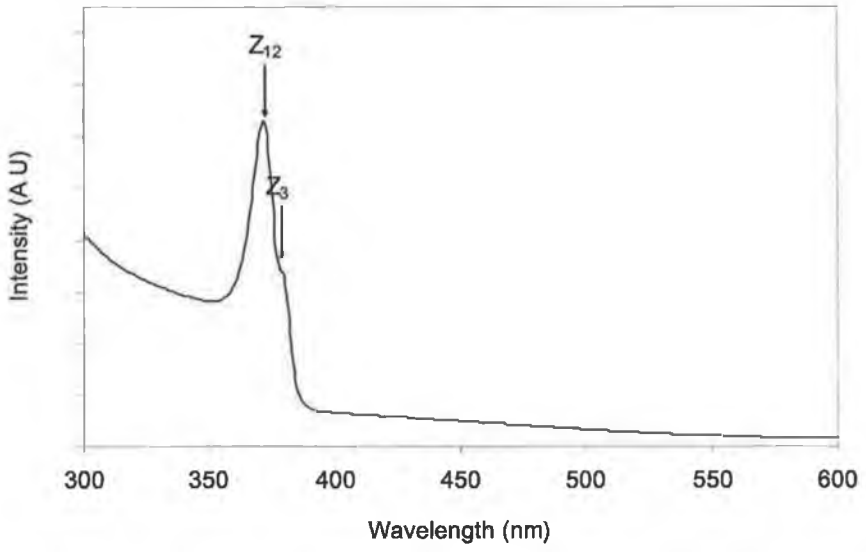

Figure 4.7. A typical UV-Visible absorption spectrum from a sample deposited at 1.1×10^{-3} mbar

A typical UV-VIS absorption spectrum taken at room temperature from a film deposited at 1.1×10^{-3} mbar is given in figure 4.7. The peak at approximately 372 nm

is the absorption due to the Z_{12} exciton and the shoulder peak at 380 nm is due to the Z_3 exciton. The intensity of the exciton peaks in the UV-VIS spectra is compared with the XRD results (Figure 4.8).

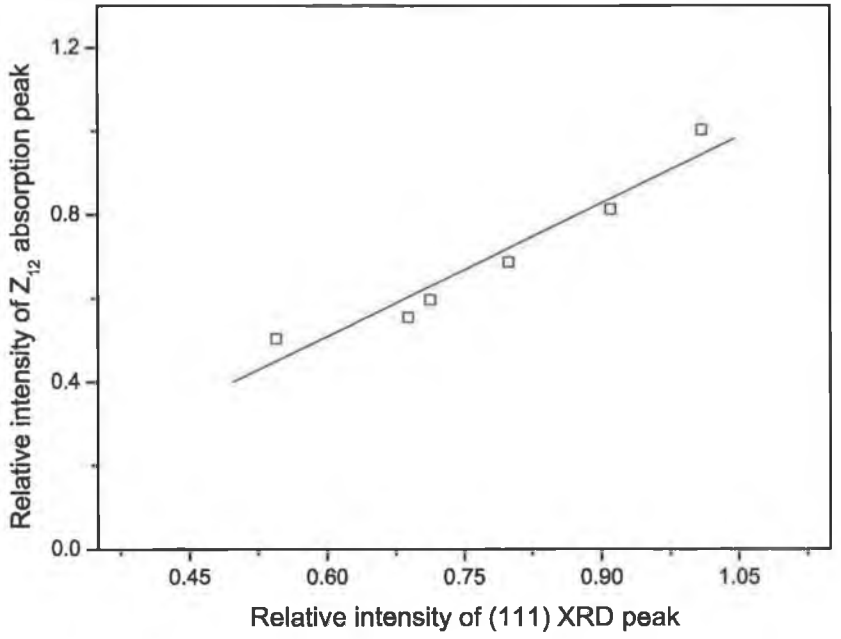

Figure 4.8. Plot showing the relationship between structural and optical properties of the film.

It is interesting to note that the intensity of the exciton absorption decreases as the (111) X- ray diffraction intensity decreases on increasing the sputtering pressure. The UV-VIS spectroscopic analysis correlates well with the CL and XRD analysis and a strong relation between the microstructure and excitonic characteristics has been found.

4.4 Summary

The microstructural and optical properties of sputtered CuCl thin films were found to be influenced by the sputtering gas pressure. Microstructural analysis revealed that the grain interface area of the films increases when the sputtering pressure is increased. The growth mechanism of the film is influenced by the diffusion and grain growth rates determined by ad-atom mobility on the growing surface. The CL spectrum shows a strong UV emission due to the recombination of Z_3 excitons. The UV emission increases with the decrease in grain interface area. The optoelectronic properties were found to be influenced by the existence of meso and nanostructural interfaces with in the thin film.

Chapter 5

TEMPERATURE DEPENDENDANT OPTICAL INVESTIGATIONS

Low temperature optical spectroscopy gives a better insight into the electronic transition in the material. In this chapter, a detailed investigation is presented on the excitonic characteristics of CuCl films at various temperatures from 15 - 300K using photoluminescence spectroscopy. When the temperature increases, the interaction between phonons and excitons results in the decrease excitonic line intensity, line broadening and shift. In this context, the experimental data are theoretically fitted and extracted parameters are compared with the previous reports.

5.1 Excitonic transitions in CuCl

The edge excitons (*Mott-Wannier* type) Z_{12} and Z_3 originate from the coupling of the lowest conduction band state Γ_6 to the uppermost valence band holes $\Gamma_7(Z_3)$ and $\Gamma_8(Z_{12})$. The binding energies of the excitons and biexcitons (excitonic molecules) are 190 meV and 34 meV [48], which are very much larger than those of III-V and II-VI semiconductors.

Figure 5.1 shows the PL spectra taken at room temperature and 15 K. The emission bands at 15 K are composed of a strong UV emission governed by the free exciton (Z_3) emission at ~ 385 nm and two other weaker peaks observed at approximately 375 and 390 nm. The peak at 375 nm is identified as the Z_{12} exciton and the shoulder peak at 390 nm is the I_1 exciton. The origin of the I_1 bound exciton is considered to be intrinsic and a Cu^+ ion vacancy is the most probable defect that binds the exciton [122].

Comparing the low temperature PL spectrum with the previous reports [123,124], one major difference observed in sputtered CuCl films is that it exhibits much stronger free exciton emission than polycrystalline or bulk CuCl. A similar observation is reported for microcrystalline CuCl [125] and very thin CuCl epitaxial films [126]. This can be related to the radiative decay of the ballistic collisions of free excitons on the grain boundaries, a microcrystalline counterpart of so-called *wall collisions,* proposed by Shuh *et al* [126].

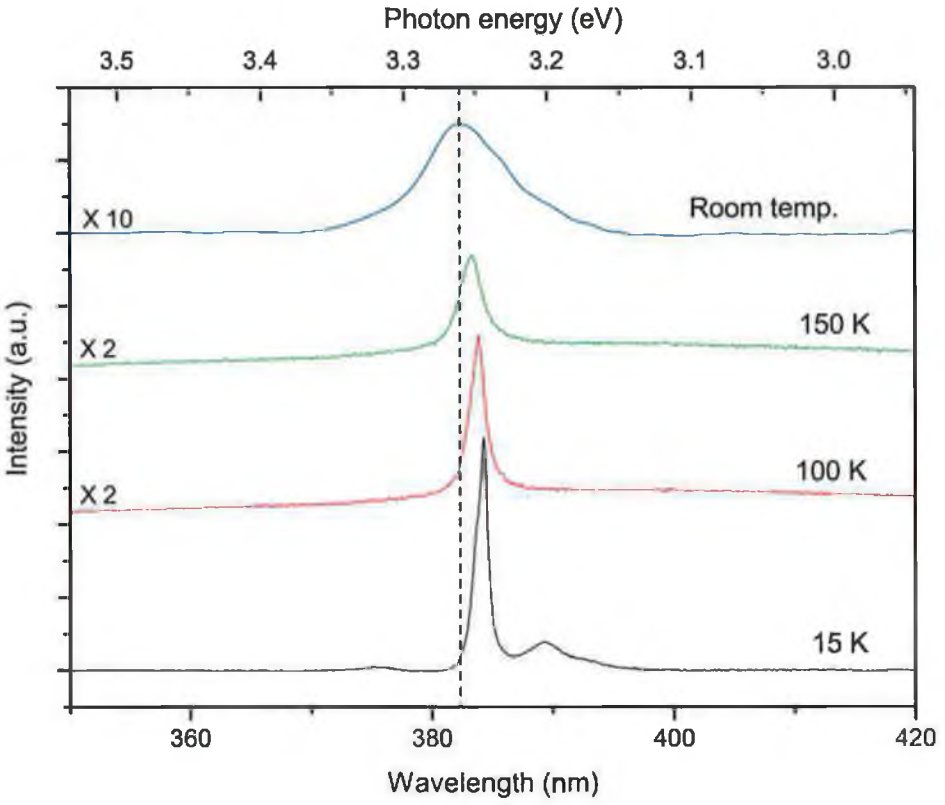

Figure 5. 1. Photoluminescence spectra taken at different temperatures

When the temperature increases, the atoms in the lattice move from their equilibrium positions and this will give rise to a set of lattice vibrational waves propagating through the lattice. These are called phonons or lattice vibrations. Any material that has more than one atom in the unit cell has two types of phonon (acoustic and optic) whose vibrating frequencies are different. Due to the interaction of these phonons with the excitons in the materials, several consequences are observed in the temperature dependant spectroscopy that include,

(i) intensity decrease,

(ii) disappearance of transitions related to the bound state,

(iii) line broadening and

(iv) a shift to high energy (blue shift)

The emission intensities of both the free and bound exciton transitions decreased with the increase in temperature. The Z_{12} free exciton and I_1 bound exciton emissions disappeared above 40 K. Generally, Z_{12} is not observed clearly in the emission spectra due to self absorption. The bound exciton I_1 is thermally dissociated when the temperature increases [127]. For single crystal CuCl, the I_1 line was found to disappear after 70 K [127], which is slightly more stable than that of sputtered CuCl films. A bound exciton dissociation may result in the release of free exciton as observed in ZnO [128]. But in the case of CuCl, thermal quenching of I_1 did not cause any increase in the Z_3 emission intensity, hence the decrease of bound excitons does not release any free excitons.

5.2 Thermal quenching of luminescence intensity

The stability of the exciton emission can be determined by analysing the rate of decrease in the emission intensity as a function of temperature. (Figure 5.2) The decrease in the free exciton emission intensity can be expressed by the well-known equation [129] for thermal quenching:

$$I = \frac{I_0}{\left[1 + A\exp\left(\frac{-E_A}{k_B T}\right)^{-1}\right]} \tag{5.1}$$

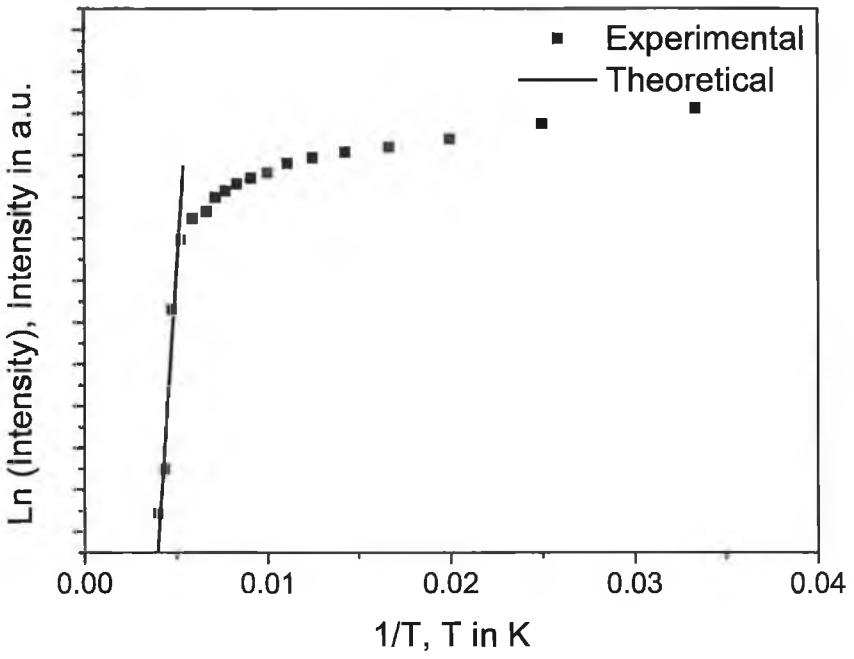

Figure 5.2. Excitonic emission intensity as a function of temperature

Where, I_0 is the peak intensity at T = 0 K. E_A is the activation energy in the thermal quenching process. A is a constant and k_B is the Boltzmann constant. The advantage of having a large excitonic binding energy is clearly seen from equation 5.1. As the exciton emission intensity has an exponential variation with the temperature, the straight line part of the above plot gives the thermal activation energy/excitonic binding energy for Z_3 excitons. The thermal activation energy was estimated to be around 112 meV. This energy is related to the thermal dissociation of the free excitons and this is essentially the same as the binding energy of the excitons. This value is lower than the calculated exciton binding energy (190 meV) [48,130] and

also that reported for single crystal CuCl (150 meV) [131]. The exciton emission in the sputtered CuCl films is much more stable compared to ZnO and GaN [132].

5.3 Exciton line broadening

The FWHM of the Z_3 exciton line increases together with the blue shift when the temperature is raised due to the increased exciton-phonon interactions [53]. The variation in the Z_3 line width Γ is plotted as a function of temperature in figure 5.3. The emission peaks taken at different temperatures were fitted to a Lorentzian distribution [133] to find the FWHM. The line width increases gradually up to 110 K and increases exponentially up to room temperature.

The temperature induced Z_3 line broadening was studied for CuCl single crystals by Kaifu and Komatsu [134]. The line width variation was explained by a simple function,

$$\Gamma = \Gamma_0 + CT^2 \tag{5.2}$$

Where C is a fitting parameter and T is the absolute temperature. Hence, Z_3 line width varies proportional to the square of the absolute temperature from 100K to 300 K. Less attention was paid to the variation less that 100 K. For temperatures above 100K, the interaction of excitons with long wavelength acoustic phonons is considered to cause the line broadening.

Later Masumoto *et. al.* [135], studied the line broadening in CuCl microcrystals. They used the following expression to explain the thermal broadening of Z_3 line width,

$$\Gamma = \Gamma_{inh} + \frac{A}{\left[\exp\left(B/k_B T\right) - 1\right]} \tag{5.3}$$

Γ_{inh} is the inhomogeneous line broadening, which was considered to arise from the size distribution of microcrystals. The parameters A and B represent the optical phonons. In this case also, the line broadening at low temperature could not be explained in terms of phonon broadening. The line width dependence was explained considering the interaction of excitons with optical phonons, which holds for the change in line width only above 70 K. The experimental results are fitted using eqn. 5.3, according to this model and it is shown in figure 5.3. It can be readily observed that the model is not obeyed at lower temperature although a reasonable fit is seen for higher temperature (above 150 K).

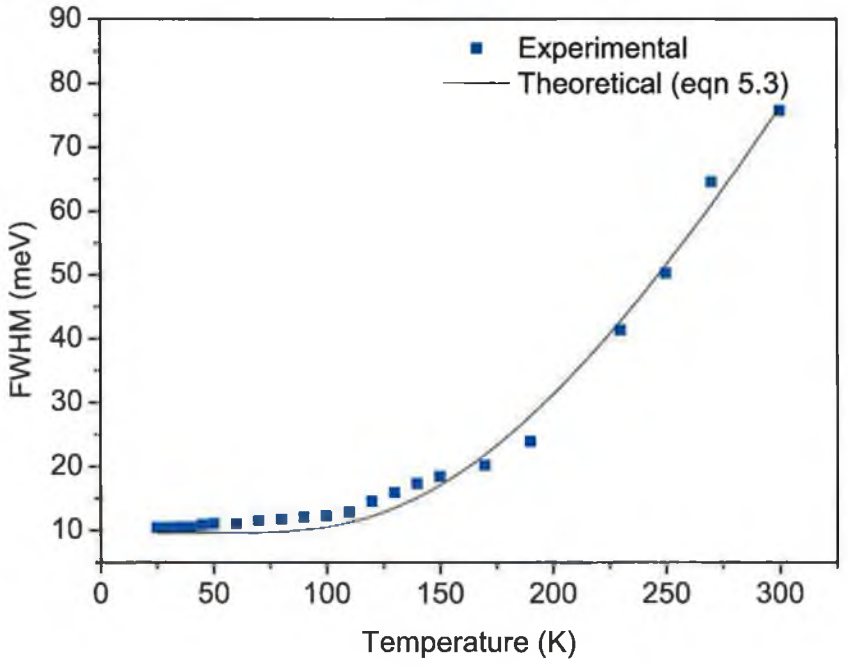

Figure 5.3. Temperature dependence of Z_3 line width fitted with eqn. 5.3

In our case, the line broadening is well expressed by [132],

$$\Gamma = \Gamma_0 + \gamma_{LA} T + \frac{\gamma_{LO}}{\left[\exp\left(h\upsilon_{LO}/k_B T\right) - 1\right]} \tag{5.4}$$

The best fit from the above equation is shown by the solid line in figure 5.4. This expression takes into account the interaction of excitons with both acoustic and optical phonons. Γ_0 is the line width at 0K which arises due to interface roughness, exciton-exciton interaction, and scattering of excitons by impurities. The parameters γ_{LA} and γ_{Lo} describe the interaction of excitons with longitudinal acoustic and optical phonons of a lattice. $\left[\exp\left(h\upsilon_{LO}/kT\right) - 1\right]^{-1}$ is the population of LO phonons of energy $h\upsilon_{LO}$ at temperature T. As seen from equation 5.2, the temperature

dependence of exciton line width allows one to analyze the coupling of excitons to the acoustic and optical phonons.

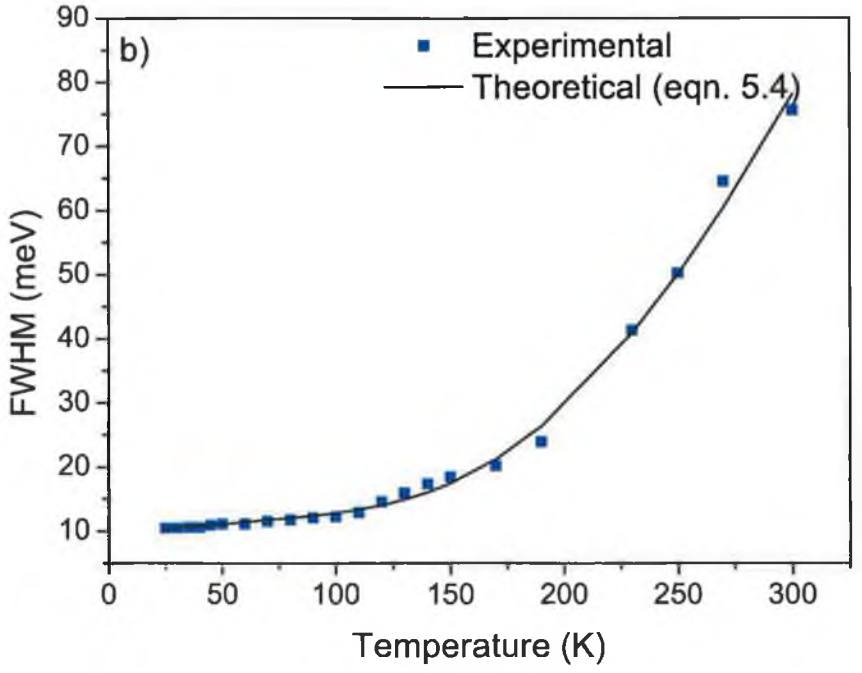

Figure 5.4. Temperature dependence of Z_3 line width fitted with eqn. 5.4

The line width increases gradually up to 110 K and increases exponentially up to room temperature. This means that the acoustic phonons are responsible up to 110 K and the optical phonons become dominant to cause the line width by interacting with the excitons. The separate contributions from acoustic and optic phonons will be discussed in detail in the next section (5.4). For a fitting of the above equation to our data, we get $\Gamma_0 = 9.61 \pm 0.9$ meV, $\gamma_{LA} = 29 \pm 14$ μeV and $\gamma_{Lo} = 938 \pm 77$ meV. The value of LO phonon energy in CuCl is 25.6 meV. Comparing the value from the fitting of equation 5.4, the line broadening in our case may involve absorption of

three LO phonons. For CuCl microcrystals, it was found to involve three LO phonons [115].

	Sputtered CuCl (present work)	CuCl microcrystals [135]	GaN [132]	ZnO [136]
Γ_0 (meV)	9.61	8	3.2	-
γ_{LA} (μeV/K)	29	-	14	10.8
γ_{LO} (meV)	938	474	395	735
$h\upsilon_{LO}$ (meV)	73	55	90	72

Table 5.1. Parameters for the exciton line broadening in sputtered CuCl films compared to previous reports

Table 5.1 compares the line broadening parameters of CuCl films with CuCl microcrystals, ZnO and GaN. The value of γ_{LA} is comparable to that of ZnO and GaN. γ_{Lo} is found to be noticeably larger for CuCl films. This indicates that there is a very strong exciton-optical phonon interaction. This is expected since CuCl is a highly polar material. [126] A room temperature PL-FWHM (~74 meV) of sputtered CuCl is better than, or comparable to, other UV emitting materials such as epitaxially grown GaN based quantum structures [137] and ZnO nanostructures [138].

5.4 Exciton line shift with temperature

As discussed above, due to the interaction of lattice vibrations with the excitons, the effective band gap increases until 100K and then it almost remains the same up to room temperature as shown in figure 5.5.

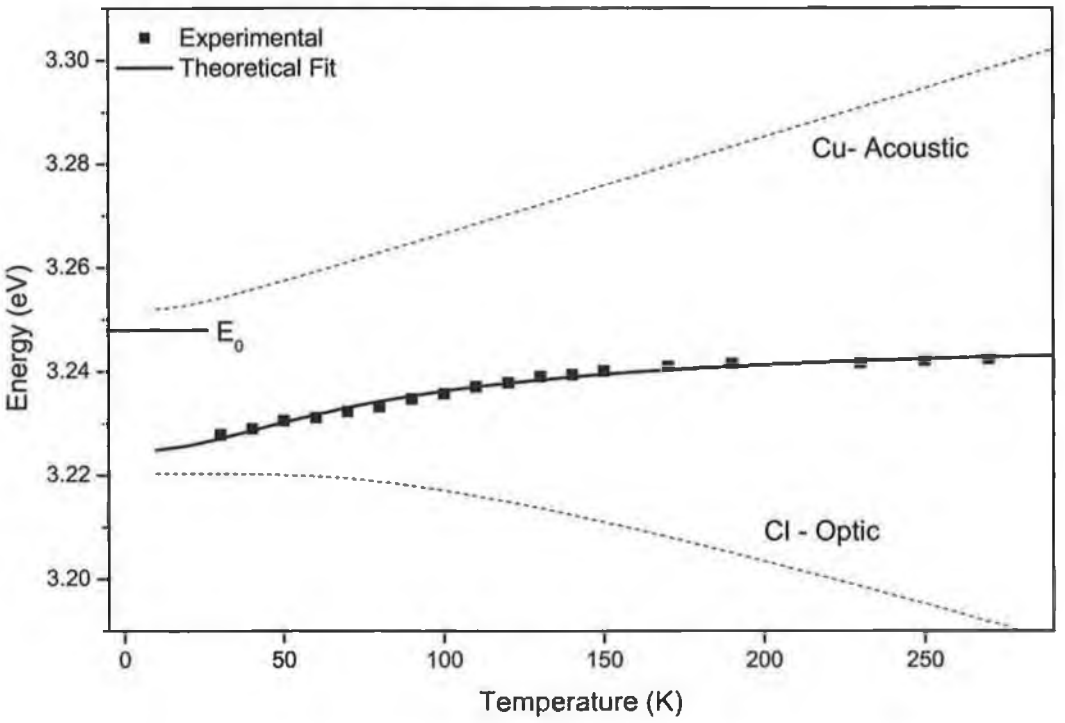

Figure 5.5. Variation of free exciton (Z_3) energy with temperature. Theoretical fit using equation 5.4

This blue-shift as a function of temperature is in contrast to that of other wideband gap semiconductors such as GaN, ZnO [132,139]. Therefore the band gap variation with temperature doesn't follow Varshni's model. The temperature dependence of band gap energy with Varshni's model is given as,

$$E(T) = E(0) - \frac{\alpha T^2}{(\beta + T)} \tag{5.5}$$

Where E(0) is the corresponding energy at 0K, and α and β are Varshini's thermal co-efficients.

Temperature dependence of band gap energy in CuCl is well explained by the *two oscillator* model proposed by Göbel *et al.* [140]. In general, the temperature dependence band gap renormalisation is a complicated interplay of,

(i) First and second order electron phonon interactions that contribute to the energy of the conduction and valence bands.

(ii) Changes due to thermal lattice expansion

(iii) Changes in the phonon occupation number

In a more simplified approach to explain this, the band gap renormalisation is considered to be caused by two harmonic oscillators. This considers that copper vibrates predominantly at low frequencies. (acoustic modes) and chlorine vibrates at higher frequencies (optic modes) because of its relatively smaller mass. According to the above hypothesis, the mass and temperature dependence of the gap can be expressed by the following equation [140]:

$$E(T,M) = E_0 + \frac{A_{Cu}}{\upsilon_{Cu} M_{Cu}}\left(\frac{1}{\exp(h\upsilon_{Cu}/k_B T)-1}\right) + \frac{A_{Cl}}{\upsilon_{Cl} M_{Cl}}\left(\frac{1}{\exp(h\upsilon_{Cl}/k_B T)-1}\right) \quad (5.6)$$

E_0 is the unrenormalised energy gap. Cu vibrates at the acoustic frequency of υ_{Cu} = 1 THz, and Cl which has relatively smaller mass vibrates at acoustic frequency of υ_{Cl} = 6 THz [140]. A_{Cu} and A_{Cl} are the electron-phonon interaction parameters for Cu and Cl respectively. E_0, A_{Cu} and A_{Cl} can be determined by fitting the above equation to the experimental data for temperature dependence of the band gap. These extracted parameters will de discussed later.

In figure 5.5, the experimental data points are fitted (Levenberg-Marquardt nonlinear fitting) with the above expression for band gap renormalisation which is shown by solid line. The separate contributions from copper and chlorine are given by the dashed lines. The unrenormalised energy gap was found to be $E_0 = 3.248$ eV. At the zero point motion, copper like acoustic vibrations increase the band gap by 3.6 meV and the chlorine like acoustic vibrations decrease the gap by 27.9 meV [140]. When the temperature increases, copper like vibrations begin to renormalize starting from the low temperature, where as the negative contribution from chlorine like vibrations is almost remains the same until 70 K and then it starts yield a higher negative contribution until room temperature.

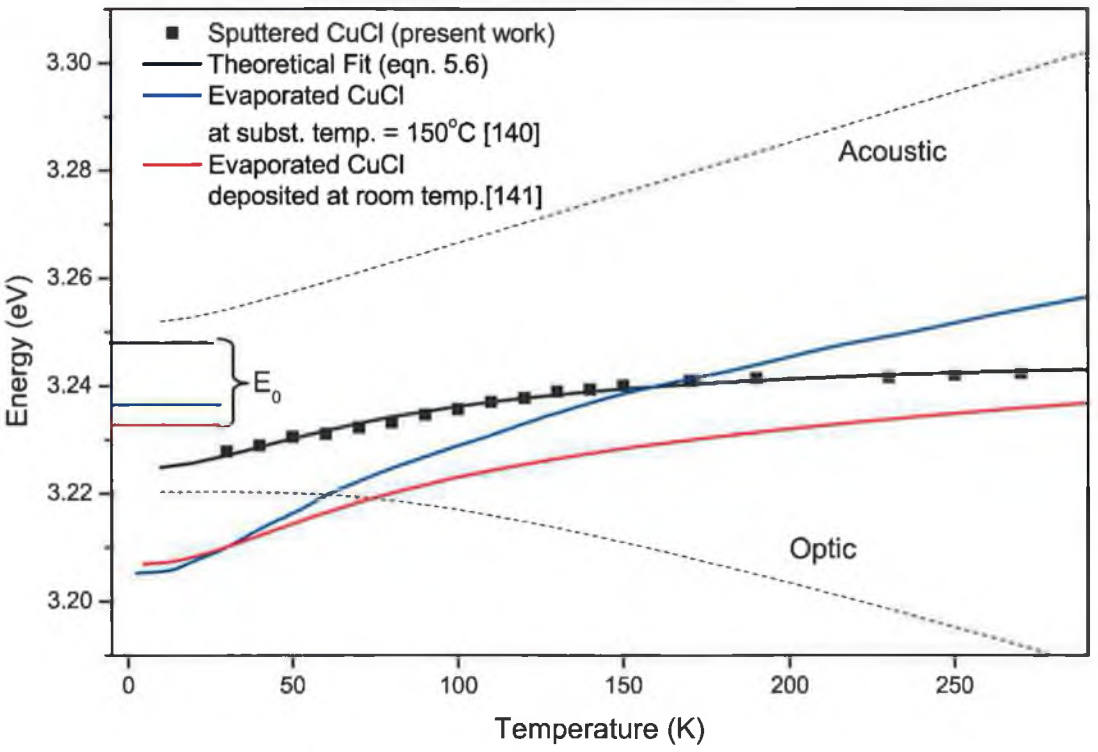

Figure 5.6. Z_3 excitonic energy shift with temperature: Comparison with ref. 140 & 141

Figure 5.6 shows a comparison of the present result with the other reports. The important conclusions drawn here are:

(i) The value of the unrenormalised energy gap (E_0) is higher compared to that of the previous reports for evaporated CuCl thin films [140,141].

(ii) The temperature dependence of the fundamental band gap is not significant above 100 K.

At a temperature of 15 K, Z_3 transition occurs at an energy of 3.224 eV ± 0.78 meV. This is blue shifted to about 15 meV compared to the Z_3 transition energy of bulk

CuCl (3.210 eV) [134]. This shift is similar to those reported for CuCl microcrystals grown by sputtering (3.224 eV) [124], and quench deposition (3.225 eV) [125]. Ref. 122 and 124 attribute the observed blue-shift to the quantum confinement of excitons. The blue-shift of the exciton energy in the nanocrystals can be expressed as [124],

$$\Delta E = \frac{\hbar^2 \pi^2}{2M(a^*)^2} \tag{5.7}$$

where, M is the exciton translational mass, $a^* = a - 0.5a_B$, a is the radius of the nanocrystal and a_B is the Bohr radius of the exciton (0.7 nm for CuCl). A blue-shift of ΔE = 15 meV corresponds to a nanocrystal radius of 3.5 nm. In our case the grain size of sputtered CuCl was found to be around 45 nm from X-ray diffraction analysis. Since the grain size is too large for quantum confinement of excitons, it is unlikely that such phenomenon could explain the observed blue-shift. The other possibility for the transition energy increase could be the micro-strain in the film. Strain in a sample, in principle, can produce changes in the crystal symmetry. Variation in the crystal symmetry is reflected in the electronic band structure and shifts the energy levels. Such an observation of Z_3 energy increase under stress is reported [142]. Comparing the lattice constant of sputtered CuCl (5.4312 Å) with that of the standard bulk (5.4163 Å [47]) suggests that the lattice of the sputtered film is strained in a tensile manner. Hence, it is believed that, the observed variation in Z_3 excitonic energy could be related to micro-strain in the sputtered films, among the various possible reasons.

Copper and chlorine vibrations begin to renormalize the fundamental gap E_0 when the temperature increases (refer figure 5.5). Copper-like vibrations increase the band gap,

whereas high frequency chlorine-like vibrations give a negative contribution. As a consequence of renormalization of both the vibrations (Cu and Cl), the band gap shifts towards higher energy when the temperature increases. However, the excitonic band gap blue-shift is less pronounced for our sputtered samples compared to Refs. 140,141. We relate this to the chemical stoichiometry deviation in our samples. Our samples are slightly chlorine rich (Cu/Cl = 0.93), as mentioned earlier. In Cl rich samples, a higher negative contribution from Cl phonons can be expected which inhibits the increase in the band gap with temperature. Moreover, the electron-phonon interaction parameters calculated from equation 5.4 were A_{Cu} = 0.00238 eV^2 amu^{-1} and A_{Cl} = -0.04782 eV^2 amu^{-1}. As expected, A_{cu} is smaller and A_{Cl} is larger than that of the previously reported evaporated CuCl films [141].

5.5 Summary

Excitonic line transitions of sputtered CuCl films were investigated using temperature dependant PL spectroscopy from 15K to room temperature. The thermal activation energy was calculated to be 112 meV. The line broadening was analysed considering the exciton-phonon interactions, at lower temperatures acoustic phonons were found to have larger influence, whereas at higher temperatures (above 110 K) optical phonon scattering was the main source of line broadening. The Z_3 excitonic line was found to exhibit a blue-shift with an increase of temperature and it follows a *two oscillator* model [140]. The fundamental band gap is shifted to higher energy with increasing temperature and this is probably related to the micro-strain developed due to smaller grain sizes. The energy shift is inhibited by the interaction between the

exciton and optical phonons as the samples are slightly Cl rich. Thermal quenching of exciton intensity and line broadening were investigated. The samples were found to a have high optical quality, comparable to other UV emitting materials such as epitaxially grown GaN and ZnO, demonstrating the potential for CuCl/Si based UV photonic devices.

Chapter 6

ELECTRICAL STUDIES

In this chapter, a preliminary electrical study on this material is discussed, since it is important to know the electrical characteristics such as resistivity and also conduction mechanisms in the material for the fabrication of a reliable device. Resistivity of CuCl was measured using Transmission Line measurement (TLM) geometry. Field dependant charge carrier transport mechanisms in CuCl/Si structures are investigated in detail.

There are a few reports on the AC conductivity and also ionic conduction [143,144] of this material. In general the major source for the electronic conduction in the compound semiconductors is the deviation from the ideal stoichiometry. Copper halides are found to be naturally halogen rich and excess halogen corresponding to a copper vacancy causes hole conduction [143]. When

the excess halogen was carefully removed, a predominant ionic conduction was observed through copper ions. Temperature dependant total electrical conductivity was reported by Wagner *et al.* [143]. The total electrical conductivity for samples free from excess Cl was measured in the temperature range of 200 to 400°C and it was concluded that ionic conduction is the predominant conduction mechanism for the temperatures more than 300^0C. Reports on the DC conductivity of CuCl are rarely found in the literature. In the present investigation, we attempt to find the resistivity and field dependant DC charge transport in sputtered CuCl. For the electrical studies, CuCl films were deposited at a target to substrate distance of 6 cm and a sputtering pressure of 1.1×10^{-3} mbar, keeping the substrates at floating potential. It is to be noted that films were slightly Cl rich (Cu/Cl = 0.94) and the grain size was around 40 nm.

6.1 Resistivity measurement by TLM technique

The more common techniques for the resistivity measurement of thin films are four point probe and *van der Pauw* methods. Among these, the four point probe method does not need any complicated sample preparation. But the van der Pauw method requires some post deposition patterning of the sample. These methods give the resistivity of the film only and not separate information on sample resistivity and the resistance due to the contact. Attempts were made to take resistivity measurements using a four point probe technique, but a high level of inaccuracies were found in the results.

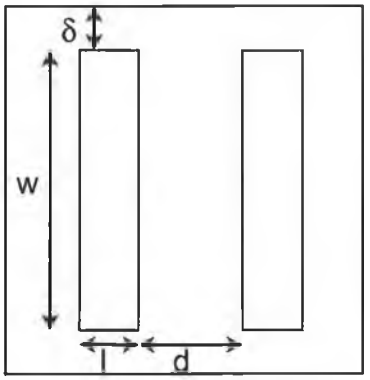

Figure 6.1. Geometry of a linear TLM structure

The resistivity measurements were then made using the Transmission line measurement (TLM). Although the TLM method is slightly more time consuming because of electrode deposition, it provides separate information on resistivity of the thin film and contact resistance. Also, the metal pads in the TLM ensure that puncturing through the film is less likely and repeatable results were obtained with acceptable standard deviation (less than 4%). This technique relies on resistance measurements between a series of pads with varying spacing.

This measurement was originally proposed by Shockley, where the resistance is measured between two rectangular pads of length l and width w on an insulated mesa width of $w+2\delta$. (Figure 6.1). When the resistance of the sample layer is constant, the total resistance R_T between two rectangular pads will be,

$$R_T = 2R + \left[\frac{\rho_s}{wt}\right] d \qquad \text{for } \delta << \text{w} \tag{6.1}$$

R_T is the total resistance between two contacts that comprises the resistances of the contacts and the contribution from the sheet resistance of the film. ρ_s is the

resistivity of the semiconductor. t is the thickness of the layer and R is the resistance of one contact.

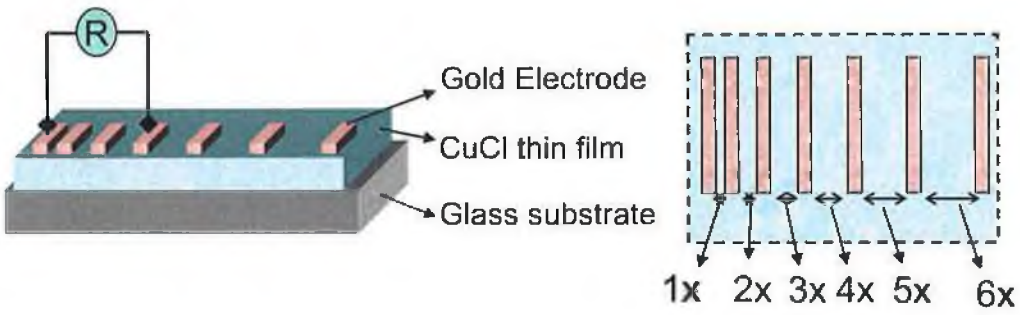

Figure 6.2 a) Schematic of TLM measurement, b) Top view

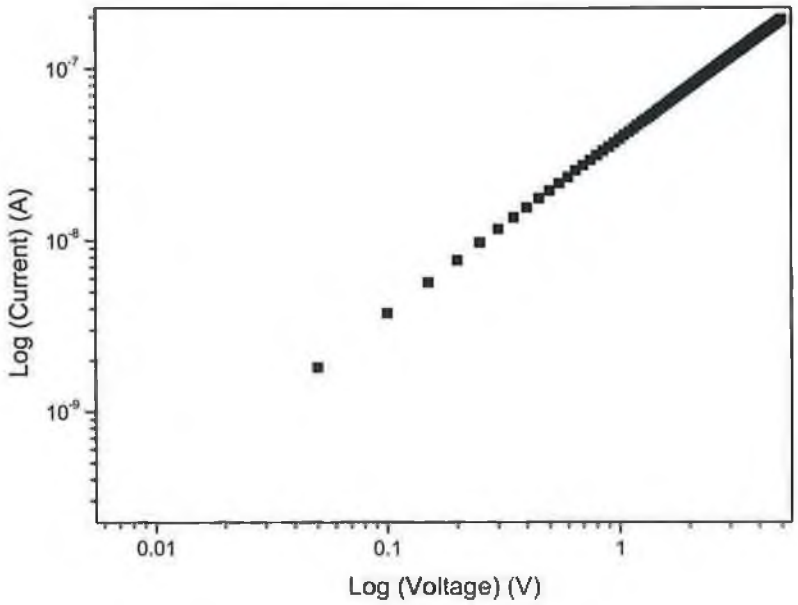

Figure 6.3. Log(I) vs log(V) measured between two contact pads in TLM structure

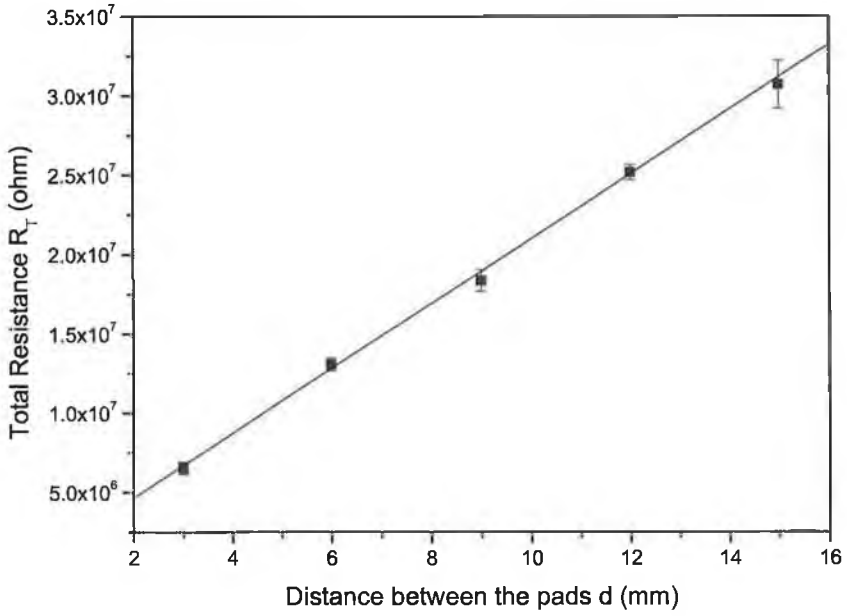

Figure 6.4. Variation in total resistivity (R_T) vs. the contact spacing (d) in a TLM structure

The current-voltage dependence was measured between two adjacent pads (see the schematic in figure 6.2) and it was found to be linear through out the applied field range (figure 6.3). Therefore, the resistivity and the contact resistance will be constant through this range. Figure 6.4 shows a typical plot of the total resistance R_T versus contact spacing. The intercept with the y-axis yields 2R, which is the contact resistance. Multiplying R with the contact area yields the normalized contact resistance. The intercept with the x-axis yields L_x, = $2L_T$, from which the transfer length, L_T, can be obtained. This transfer length is a measure for the "ohmic quality" of the metal contact. L_T typically varies from tens of μm to several μm. A shorter L_T means a better ohmic contact. (L_T = 165 μm) From the slope of the linear fit ($\frac{\rho_s}{wt}$) the resistivity of the thin film can be calculated. The specific contact resistance can be calculated from the y intercept, $\rho_c = R\ w L_T$.

The calculated resistivity from the above plot was ρ_s = 321 Ω.cm. From the previous report from our group [145], the resistivity of CuCl film by thermal evaporation was 300 Ω.cm, which is quite same as the sputtered CuCl films. Apparently, the resistivity of CuCl films is very high, comparing to the resistivity of more matured materials such as p or n doped Si which is in the order of less than 10 Ω.cm. It is to be noted that the sample taken for resistivity analyses is slightly Cl rich which is expected to be p- type due to non-stoichiometry [143]. The specific contact resistance of Au contacts on CuCl ρ_c was 2.1958×10^{3} Ω.cm^2. Comparing this to Si/Ti/Al/Ni/Au ohmic contacts on GaN = 1.06×10^{-6} Ω.cm^2 [146] and Ti/Al/Pt/Au ohmic contacts to ZnO = 3.9×10^{-7} Ω.cm^2 [147]. Therefore it is necessary to reduce the specific contact resistance to many orders.

6.2 Field dependant conduction studies

Electrical properties of CuCl/Si structure was studied by analyzing the I-V characteristics of the structure. I-V behavior of the structure is compared with that of Si in order to have separate information on the electrical behaviour of CuCl film. To investigate the I-V behaviour of Si, electrical contacts on the top and bottom of the substrate were taken via Ag electrodes. Figure 6.5 shows the I-V behaviour of a Ag/Si/Ag structure.

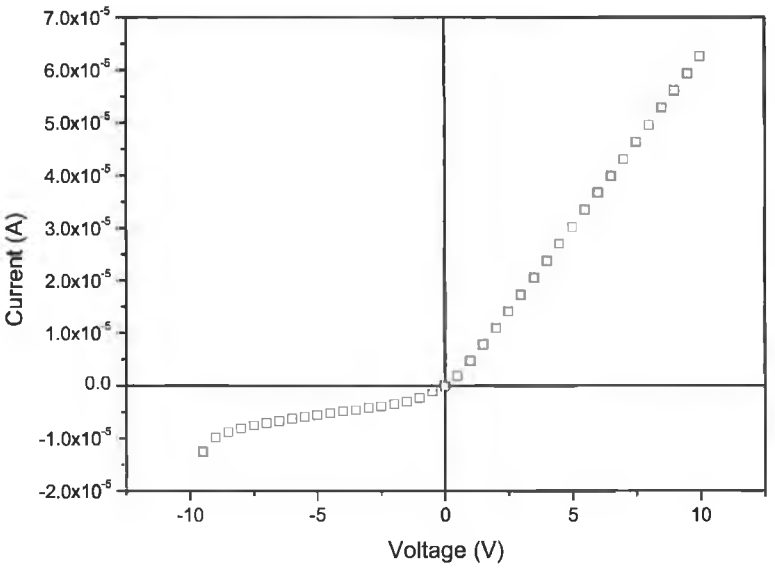

Figure 6.5. I-V characteristics of n-type Si (substrate)

According to the I-V curve (shown in figure 6.5), current varies linearly with voltage in one direction, whereas a comparatively lower current flows through the structure when the bias is reversed. This can be explained as follows: A contact resistance due to leakage current, in general, will be formed at the electrode-semiconductor junction. The magnitude of this resistance depends on the area of the junction. If the electrode area of the bottom and top contacts were equal, then a similar I-V behaviour for both positive and negative biases could be expected.

In the present case, however, the electrode-semiconductor contact area at the top electrode is much smaller than that at the bottom electrode (see figure 6.6a). Therefore, contact resistance of the top-electrode-Si junction (R1) will be higher than that at the top-electrode-Si junction (R2). The amount of current flows through the circuit, during either biasing, is mainly decided by these limiting resistors R1 and R2. In addition with a contact resistance, a metal contact with n-type Si will also perform as a Schottky type diode. D1 and D2 are the Schottky

diodes formed at the top and bottom electrode junctions with Si, respectively. The semiconducting Si itself can provide a resistance R3 to the electrical current flows through it. Hence, an equivalent electronic circuit for the Ag/Si/Ag structure considering all these resistors and diodes can be drawn as given in figure 6.6b. Note that this particular circuit represents the forward bias configuration.

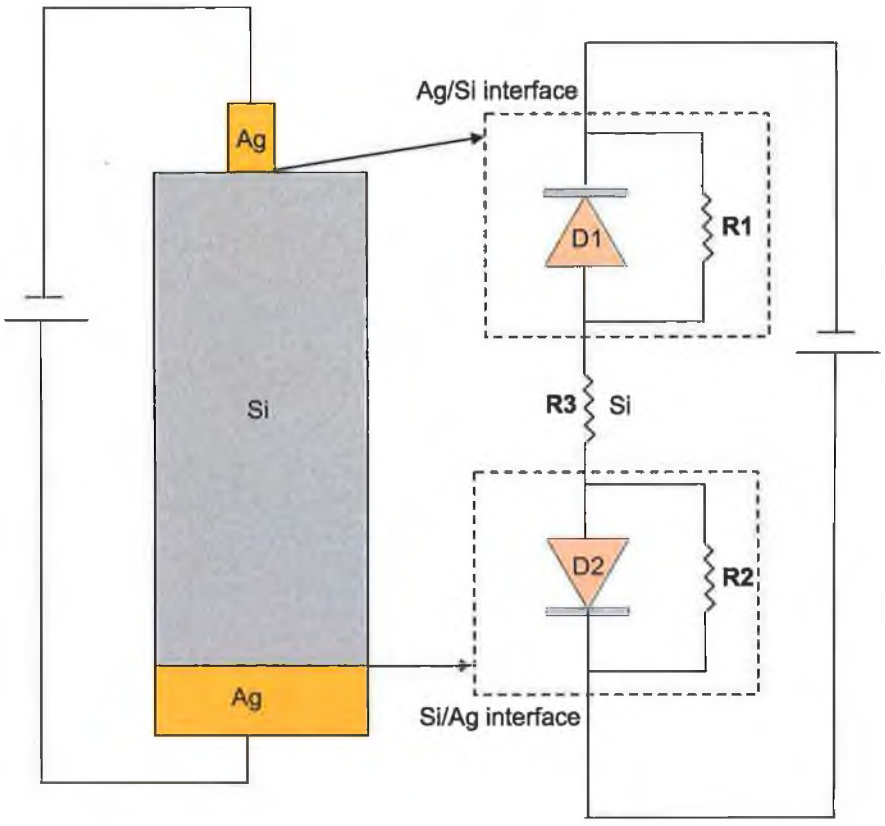

Figure 6.6. Schematic of Ag/n-Si/Ag structure used for I-V studies (b) an equivalent electronic circuit for Ag/n-Si/Ag structure.

For a forwards bias configuration of the structure as shown in figure 6.6b, more current flows through R2, R3 and D1 where as no current (or at least less current) flow will be along D2 diode and R1. This is because of the fact that D2 and D1 are locally subjected to reverse and forward biases, respectively. When the

structure is reverse biased, D1 is locally reverse biased where as D2 is on forwards bias. Hence, there will be more current flow through R1 and D2 compared to the current flow through D1 and R2. Since R1 is greater than R2, a net current flow through the circuit for reverse bias is smaller compared to the forwards-bias-current.

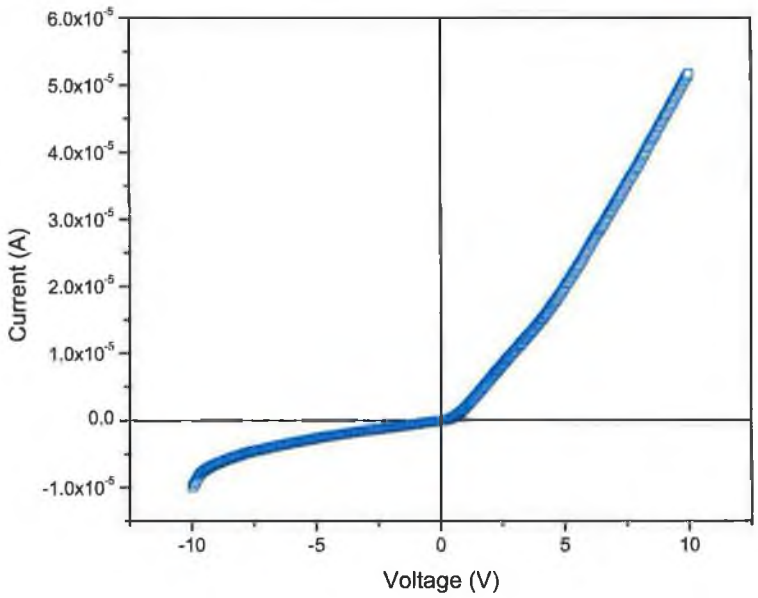

Figure 6.7. I-V characteristics of Au/CuCl/n-Si/Au structure.

The I-V behaviour of CuCl film on Si substrate is analyzed by forming Au contacts on the top and bottom of CuCl/Si structure. This Au/CuCl/n-Si/Au structure shows an I-V behaviour (see figure 6.7), which is somewhat similar to the one observed for the Ag/n-Si/Ag structure, but with an additional feature due to the presence of CuCl layer. I-V behaviour of Au/CuCl/n-Si/Au structure (see figure 6.8a) shows a difference in the slope of the IV curve in forward bias in comparison with Ag/Si/Ag structure. It should be noted that changing the metal electrode from Ag to Au should not have any significant influence on the I-V characteristics as the work function of Ag and Au metal electrodes are almost the

same (0.78 and 0.80 respectively). The pathway for the electrical current flow during the forward and reverse bias is the same as explained with the circuit shown in figure 6.6b.

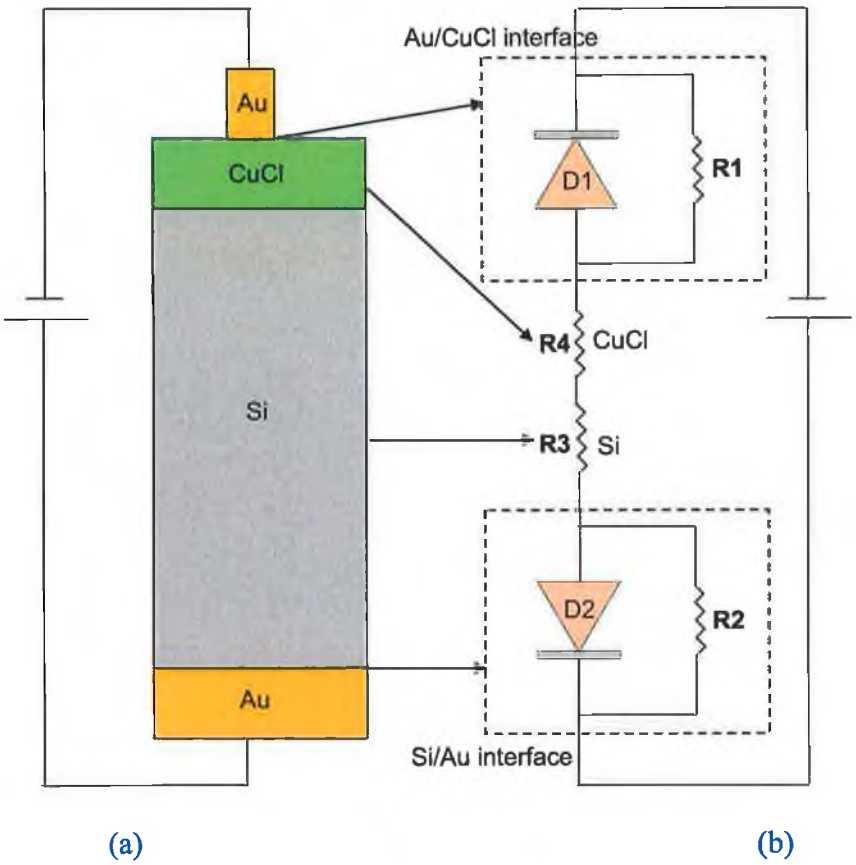

Figure 6. 8. (a): Schematic of Au/CuCl/n-Si/Au structure used for I-V characteristics. (b): Equivalent electronic circuit of Au/CuCl/n-Si/Au structure at forward bias.

It is expected that CuCl is p-type since it is naturally Cl rich. However, a hetero-structure formation between CuCl and n-type-Si is not observed. Comparing the I-V characteristics of bare Si and CuCl coated Si reveals that CuCl just acts as an additional high resistance, R3, in series with R4 as represented in the equivalent electronic circuit shown in figure 6.8b.

Voltage dependant conduction mechanism in forward bias

In figure 6.9, the I-V plot is shown in logarithmic scale which is fitted with two straight lines with two different slopes i.e., the current varies linearly with the voltage in the lower field region and a lower slope for higher applied fields. This indicates the transition of one charge transport mechanism to another as the applied field is increased.

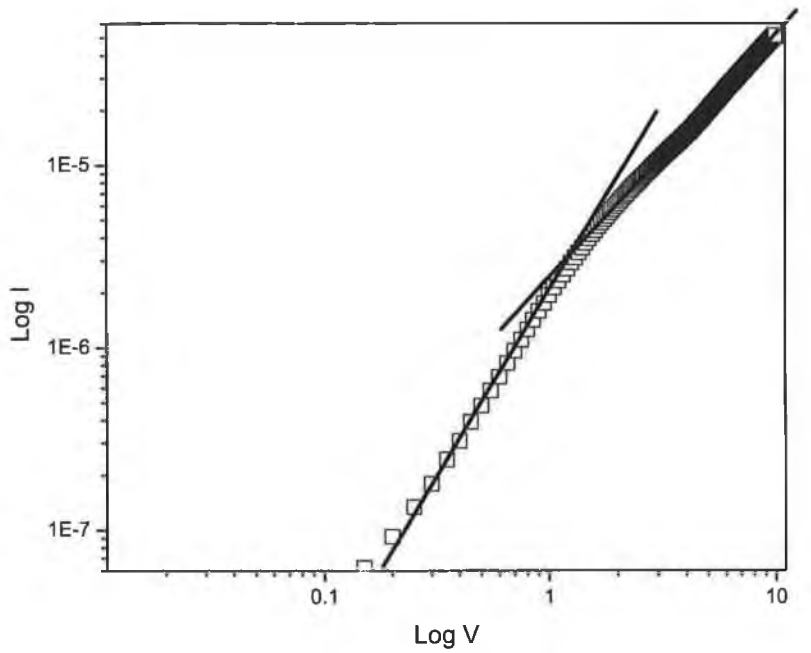

Figure 6.9. Voltage dependence of current in the form of log(I) vs log(V)

In the low field region, (up to 9.5×10^6 V/m) the I-V dependence was confirmed to be ohmic as the plot of log (I) vs log (V) yields a slope of ~1. Whereas, at higher field range above 9.5×10^6 V/m, the slope is decreases. Various mechanisms can be responsible for the charge transport at high field including,

i) Schottky (electrode limited)

ii) Poole-Frenkel (bulk limited)

iii) Ionic conduction

iv) Space charge limited conduction

v) Fowler-Nordheim tunnelling transport (thermally assisted tunnelling in very thin films ~ 10 nm thick)

Space charge limited conduction is a trap related conduction mechanism which has highly non linear I-V characteristics. The traps can arise from disorder, dangling bonds, impurities, etc. At higher applied voltages, the injected space charge will be predominant and for a solid containing trapping levels, the space charge current density J is given by [148],

$$J = \frac{9}{8}\theta\varepsilon\mu\frac{V^2}{d^3} \tag{6.2}$$

Where θ the fraction of total carriers which are free, ε is the dielectric constant, μ is the charge carrier mobility, d is the electrode spacing. Since a dependence of $I \propto V^2$ is not observed in the present case, this mechanism can be ruled out.

Fowler-Nordheim tunnelling is a quantum mechanical tunnelling process whereby electrons tunnel through the barrier in the presence of high electric field. This type of transport takes place only when the film thickness is as low as ~10 nm. Hence for the present case, the possibility of Fowler-Nordheim tunnelling transport can also be omitted because the film thickness is too large for this (~ 400 nm) [149].

From further analyses of the data, the most possible mechanism was confirmed to be either Poole-Frenkel (PF) conduction or a Schottky emission (SE) from a linear dependence of current with $V^{1/2}$ (see plot shown in figure 6.10). However, it is difficult to confirm the possible mechanism from the current dependence of $V^{1/2}$ since it is followed by both Poole-Frenkel and Schottky type conductions. The

main difference between these two conduction mechanisms is the source of the charge carriers.

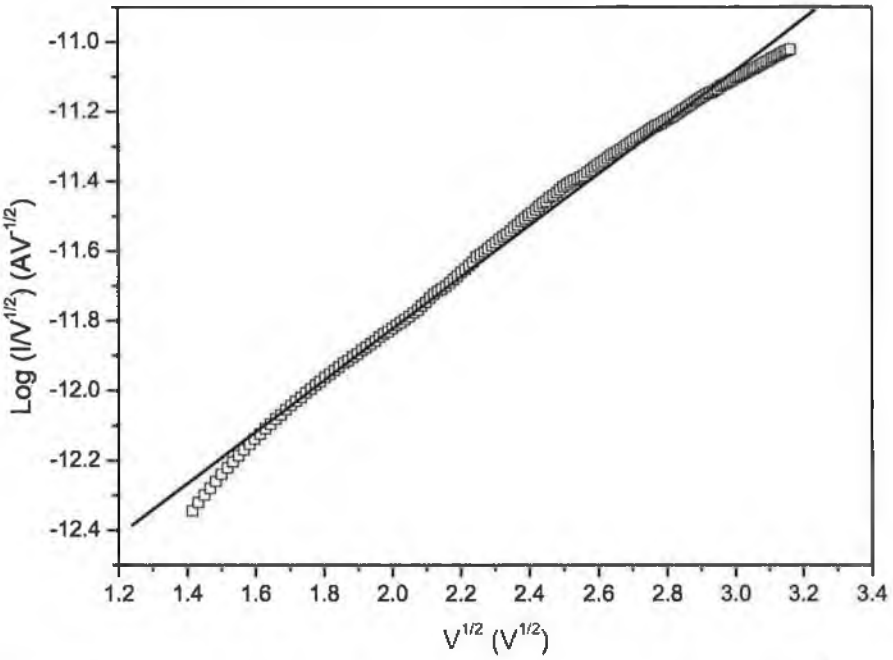

Figure 6.10. Voltage dependence of current in the form of $\log_{10}(I/V^{1/2})$ vs $V^{1/2}$

The Schottky type conduction is an electrode effect in which the charge carriers are supplied from the metal electrode, whereas Poole-Frenkel mechanism is a bulk effect, where the charge carriers come from the bulk of the insulator. The electron injection from the metal electrode into the semiconductor (SE type) can be expressed by the relation [149],

$$J_{SE} = A^{*} T^{2} \exp\left(-q\left[\phi_{B} - \left(\frac{qV}{4\pi\varepsilon_{0}\varepsilon_{r}d}\right)^{1/2}\right]/kT\right) \tag{6.3}$$

A^{*} is the effective Richardson constant, ϕ_B is the barrier height or the effective work function between the Fermi level of the metal and the conduction band of the semiconductor. ε_0 is the permittivity of the free space and ε_r and d are the

dielectric constant and thickness of the material. The other terms have their usual meanings. The Poole Frenkel effect involves lowering of a coulombic potential barrier under a high electric field. That is, the charge carriers are supplied from the bulk semiconductor. The current-voltage characteristic for this mechanism can be expressed as [149],

$$J_{PF} = BV \exp\left(-q\left[\phi_t - \left(\frac{qV}{\pi\varepsilon_0\varepsilon_r d}\right)^{1/2}\right]/kT\right) \tag{6.4}$$

B is a constant and ϕ_t is the depth of a trap potential well. For both SE and PF type mechanisms, current has a linear dependence with $V^{1/2}$ the slope of such plot should be,

$$\beta_{SE} = \frac{q}{2}\left(\frac{q}{\pi\varepsilon_0\varepsilon_r d}\right)^{1/2}/kT \tag{6.5}$$

$$\beta_{PF} = q\left(\frac{q}{\pi\varepsilon_0\varepsilon_r d}\right)^{1/2}/kT \tag{6.6}$$

for SE and PF mechanisms respectively.

The slope of the experimental plot for log (I) vs. $V^{1/2}$ was found to be 0.7697. As given by the above expression, the term $\beta_{PF/SE}$ includes the dielectric constant and also the thickness of CuCl films. The dielectric constant was deduced from the above equation for both SE and PF type mechanisms. The value of ε_r was found to be 37.7 from β_{PF}. From the previous reports, the value of ε_r for bulk CuCl ranges from 7.4 to 10 [150,151,152]. The value of 37.7 deduced from β_{PF} is physically unreasonable. Hence, it is unlikely that the observed current is due to PF mechanism. The value of ε_r calculated from β_{SE} was 9.425 which is in the

range of the reported values for the bulk CuCl. Hence, it is apparent that SE mechanism is the most likely conduction mechanism at higher field region (i.e., above the 9.5×10^6 V/m).

6.3 Summary

The resistivity of CuCl films was calculated using TLM geometry and it was found to be 321 Ω cm. This has to be reduced up to three orders of magnitude for device fabrication. The field dependant DC conduction mechanism of sputtered CuCl/Si structure was analysed. It was found that there are two distinct regions with different field dependant conduction mechanisms. Ohmic conduction prevails in the lower field of up to 9.5×10^6 V/m. By comparing the film properties (dielectric constant) obtained from the theoretical calculations and also experimental values, bulk limited Poole-Frenkel emission process was found to dominate the mechanism of charge carrier transport through these structures at higher fields up to 2.5×10^7 V/m. There was no trap related conduction even at higher bias voltages, which confirms that the films are stoichiometric and defect free.

Chapter 7

CONCLUSIONS AND FUTURE WORK

7.1 Conclusions

Wide direct band gap CuCl is a promising candidate for the next generation Si based optoelectronics, thanks to its excellent properties such as high excitonic binding energy and a close lattice matching with Si.

In this thesis, growth of CuCl using RF magnetron sputtering is investigated in detail. Stoichiometry and microstructure are the two deciding factors for the UV emission from the material. We have successfully controlled both these properties by varying different sputtering parameters. The chemical stoichiometry was mainly controlled by the spacing between the target and the substrate [Chapter 3]. Samples deposited with $d_{ts} < 6$ cm were Cl rich. The film crystallinity gradually decreased for $d_{ts} > 6$ cm. An optimum spacing of 6 cm was found to yield samples of almost close to stoichiometry (Cu/Cl = 0.94). A further control was done

providing a suitable bias to the substrate and high quality-stoichiometric CuCl films were achieved [Chapter 3].

Microstructural evaluation revealed that the grain interface area of the film increases on increasing the working pressure [Chapter 4]. UV emission properties of the films were found to be influenced by the existence of meso- and nanostructural interfaces within the thin film. Cathodoluminescence showed a strong UV exciton emission and a green emission from deep levels for non stoichiometric and poor crystalline quality samples. CuCl films deposited with optimum sputtering parameters showed good optical quality with an intense and sharp UV emission at room temperature with out any deep level emission.

Excitonic line transitions of sputtered CuCl films were investigated using temperature dependant PL spectroscopy [Chapter 5]. Sputtered CuCl films exhibit much stronger Z_3 exciton emission than evaporated or single crystal CuCl. The thermal activation energy was calculated to be 112 meV. The Z_3 excitonic line was found to exhibit a blue-shift with an increase of temperature and it follows a *two oscillator* model. Sputtered CuCl films were found to a have high optical quality, better than other UV emitting materials such as epitaxially grown GaN and ZnO, demonstrating the potential for Si based UV photonic devices.

Preliminary investigation on the electrical properties shows, the resistivity of the films is very high [Chapter 6] which an obstacle to proceed for any device fabrication. It has to be reduced two to three orders of magnitude by using a suitable dopant. Field dependant DC conduction studies of sputtered CuCl/Si

structure indicates that ohmic conduction prevails in the lower field and a bulk limited Poole - Frenkel process was found to dominate the mechanism of charge carrier transport through these structures at higher fields.

7.2 Suggestions for future work

The film properties were controllable in the RF sputtering of CuCl by varying different parameters. Optical quality of the films was also found to be very suitable for devices. One area to be explored is the electrical properties of the films since fabrication of a p-n junction is important for proceeding to any device fabrication based on CuCl. As analyzed in the preliminary electrical investigations in this thesis, the resistivity of undoped CuCl is very high. This has to be reduced 2 to 3 orders of magnitude.

As the elemental content can be finely controlled using substrate bias, it may therefore be possible to vary the intrinsic doping levels and so tune the electrical properties of the material. For extrinsic doping, introducing O_2 or N_2 during the sputter deposition can be investigated. Studies that provide information on the work function of CuCl will help to pick ohmic contact metals for CuCl.

From the evaluation of the contact resistance, Au makes a poor contact with a high contact resistance. Finding an ohmic contact for CuCl with a low contact resistance is another problem that deserves a detailed investigation. The hygroscopic nature is another important issue with CuCl. Our group has attempted to a suitable capping layer to protect CuCl films [50] and also demonstrated UV emission from an electroluminescence device [95]. Since it is proposed that the

final device on CuCl incorporates a capping layer which is a UV transparent insulating layer, further electrical studies should be carried for a structure that includes Si, CuCl and a suitable capping layer.

Another interesting area to explore in CuCl would be testing it for UV photodetector applications. Since CuCl has a band gap in UV, it will be a potential candidate for Si based UV photodetector devices. There is a previous report [153] on the photoconductivity of bulk CuCl. Again, to carry out this investigation, electrical properties have to be tuned. The bottom line is a more detailed electrical investigation on the properties such as resistivity and contact resistance is necessary for the evaluation and design of any device based on CuCl/Si.

References

[1] A. V. Nurmikko and R. L. Gunshor, IEEE J. Quantum Electron. **30**, 619 (1994).

[2] S. Nakamura, T. Mukai, and M. Senoh, Jpn. J. Appl. Phys. **30**, L1998 (1991).

[3] Y. Taniyasu, M. Kasu, and T, Makimoto, Nature **441**, 325 (2006).

[4] B. Monemar, Phys. Rev. B **10**, 676 (1974).

[5] J. A. Freitas, O.-H. Nam, R. F. Davis, G. V. Saparin, and S. K. Obyden, Appl. Phys. Lett. **72**, 2990 (1998).

[6] X. Li, S. G. Bishop, and J. J. Coleman, Appl. Phys. Lett. **73**, 1179 (1998).

[7] S. Nakamura *et al.*, Appl. Phys. Lett. **72**, 211 (1998).

[8] T. S. Zheleva, O.-H. Nam, M. D. Bremser, and R. F. Davis, Appl. Phys. Lett. **71**, 2472 (1997).

[9] J. I. Pankove, E. A. Miller, and J. E. Berkeyheiser, RCA Rev. **32**, 383 (1971).

[10] H. Amano, M. Kito, K. Hiramatsu, and I. Akasaki, Jpn. J. Appl. Phys. **28**, L2112 (1989).

[11] J. A. Freitas, O-H. Nam, R. F. Davis, G. V. Saparin, and S. K. Obyden, Appl. Phys. Lett. **72**, 2990 (2003).

[12] X. Li, S. G. Bishop, and J. J. Coleman, Appl. Phys. Lett. **73**, 1179 (2003).

[13] Y. R. Ryu, T. S. Lee, and H. W. White, Appl. Phys. Lett. **83**, 87 (2003).

[14] For a review, Z. L. Wang, J. Phys.: Condens. Matter **16**, R829 (2004).

[15] R. B. Heller, J. McGannon, and A. H. Weber, J. Appl. Phys. **21**, 1283 (1950).

[16] T. J. Gray, J. Am. Ceram. Soc. **37**, 534 (1954).

[17] G. P. Mohatny and L. V. Azaroff, J. Chem. Phys. **35**, 1268 (1961).

[18] R. R. Reeber, J. Appl. Phys. **41**, 5063 (1970).

[19] Ü. Özgür, Ya. I. Alivov, C. Liu, A. Teke, M. A. Reshchikov, S. Doğan, V. Avrutin, S.-J. Cho, and H. Morkoç, J. Appl. Phys. **98**, 041301 (2005).

[20] W. Walukiewicz, Phys. Rev. B **50**, 5221 (1994).

[21] C. G. Van de Walle, D. B. Laks, G. F. Neumark, and S. T. Pantelides, Phys. Rev. B **47**, 9425 (1993).

[22] C. H. Park, S. B. Zhang, and S.-H. Wei, Phys. Rev. B **66**, 073202 (2002).

[23] L. Svob, C. Thiandoume, A. Lusson, M. Bouanani, Y. Marfaing, and O. Gorochov, Appl. Phys. Lett. **76**, 1695 (2000).

[24] R. M. Park, M. B. Troffer, C. M. Rouleau, J. M. DePuydt, and M. A. Hasse, Appl. Phys. Lett. **57**, 2127 (1990).

[25] H. D. Jung, C. D. Song, S. Q. Wang, K. Arai, Y. H. Wu, Z. Zhu, T. Yao, and H. Katayama-Yoshida, Appl. Phys. Lett. **70**, 1143 (1997).

[26] K. Iwata, P. Fons, A. Yamada, K. Matsubara, and S. Niki, J. Cryst. Growth **209**, 526 (2000).

[27] A. B. M. A. Ashrafi, I. Suemune, H. Kumano, and S. Tanaka, Jpn. J. Appl. Phys. **41**, L1281 (2002).

[28] K. Minegishi, Y. Koiwai, Y. Kikuchi, K. Yano, M. Kasuga, and A. Shimizu, Jpn. J. Appl. Phys. **36**, L1453 (1997).

[29] Z.-Z. Ye, J.-G. Lu, H.-H. Chen, Y.-Z. Zhang, L. Wang, B.-H. Zhao, and J.-Y. Huang, J. Cryst. Growth **253**, 258 (2003).

[30] J. Wang *et al.*, J. Cryst. Growth **255**, 293 (2003).

[31] J. Lu, Y. Zhang, Z. Ye, L. Wang, B. Zhao, and J. Huang, Mater. Lett. **57**, 3311 (2003).

[32] A. Tsukazaki, H. Saito, K. Tamura, M. Ohtani, H. Koinuma, M. Sumiya, S. Fuke, T. Fukumura, and M. Kawasaki, Appl. Phys. Lett. **81**, 235 (2002).

[33] K. Nakahara, H. Takasu, P. Fons, A. Yamada, K. Iwata, K. Matsubara, R. Hunger, and S. Niki, Appl. Phys. Lett. **79**, 4139 (2001).

[34] K. Nakahara, H. Takasu, P. Fons, A. Yamada, K. Iwata, K. Matsubara, R. Hunger, and S. Niki, J. Cryst. Growth **237–239** 503, (2002).

[35] T. Ohshima, T. Ikegami, K. Ebihara, J. Asmussen, and R. Thareja, Thin Solid Films **435**, 49 (2003).

[36] M. Sumiya, A. Tsukazaki, S. Fuke, A. Ohtomo, H. Koinuma, and M. Kawasaki, Appl. Surf. Sci. **223**, 206 (2004).

[37] Ya. I. Alivov, D. C. Look, B. M. Ataev, M. V. Chukichev, V. V. Mamedov, V. I. Zinenko, Yu. A. Agafonov, and A. N. Pustovit, Solid-State Electron. **48**, 2343 (2004).

[38] M. Joseph, H. Tabata, and T. Kawai, Jpn. J. Appl. Phys. **38**, L1205 (1999).

[39] J. M. Bian, X. M. Li, X. D. Gao, W. D. Yu, and L. D. Chen, Appl. Phys. Lett. **84**, 541 (2004).

[40] Z.-Z. Ye, Z.-G. Fei, J.-G. Lu, Z.-H. Zhang, L.-P. Zhu, B.-H. Zhao, and J.-Y. Huang, J. Cryst. Growth **265**, 127 (2004).

[41] T. Aoki, Y. Hatanaka, and D. C. Look, Appl. Phys. Lett. **76**, 3257 (2000).

[42] K.-K. Kim, H.-S. Kim, D.-K. Hwang, J.-H. Lim, and S.-J. Park, Appl. Phys. Lett. **83**, 63 (2003).

[43] Y. R. Ryu, S. Zhu, D. C. Look, J. M. Wrobel, H. M. Jeong, and H. W. White, J. Cryst. Growth **216**, 330 (2000).

[44] T. L. Chu, J. Electrochem. Soc. **118**, 1200 (1971).

[45] H. M. Manasevit, F. M. Erdmann, and W. I. Simpson, J. Electrochem. Soc. **118**, 1864 (1971).

[46] JCPDS Card No. 06-344, International Centre for Diffraction, New York, 1997.

[47] JCPDS Card No. 27-1402, International Centre for Diffraction, New York, 1997.

[48] M. Nakayama, H. Ichida, and H. Nishimura, J. Phys.: Condens. Matter **11**, 7653 (1999).

[49] R. S. Williams, D. K. Shuh, and Y. Segawa, J. Vac. Sci. Technol., A. **6**, 1950 (1988).

[50] F. O. Lucas, L. O' Reilly, G. Natarajan, P. J. McNally, S. Daniels, D. M. Taylor, S. William, D. C. Cameron, A. L. Bradley, and A. Mitra, J. Cryst. Growth **28**, 112 (2006).

[51] S. Kono, T. Ishii, T. Sagawa, and T. Kobayashi, Phys. Rev. B **10**, 4388 (1974).

[52] A. Goldmann, J. Tejeda, N. J. Shevchik, and M. Cardona, Phys. Rev. B **10**, 4388 (1974).

[53] M. Cardona, Phys. Rev. **129**, 69 (1963).

[54] T. Ishii, S. Sato, T. Matsukawa, Y. Sakisaka, and T. Sagawa, J. Phys. Soc. Jpn. **32**, 1440 (1972).

[55] S. Lewonczuk, J. G. Gross, M. A. Khan, and J. Ringeissen, Phys. Status Solidi B **83**, 161 (1977).

[56] J. G. Gross, S. Lewonczuk, M. A. Khan, and J. Ringeissen, Solid State Commun. **30**, 181 (1979)

[57] W. W. Beemann, J. Forss, and J. N. Humphrey, Phys. Rev. **67**, 217 (1945).

[58] C. Sugiura, Phys. Rev. B **8**, 823 (1973).

[59] A. Zunger and M. L. Cohen, Phys. Rev. B **20**, 1189–1193 (1979)

[60] M. Ferhat, B. Bouhafs, H. Aourag, A. Zaoui, and M. Certier, Comput. Mater. Sci. **20**, 267-274 (2001).

[61] A. Goldmann and D. Westphal J. Phys. C: Solid St. Phys. **16,** 1335-1343 (1983).

[62] A. Goldmann, Phys. Status Solidi B **81**, 9 (1977).

[63] W. Pong and S. K. Okada, Phys. Rev. B **20**, 5400 (1979).

[64] H. J. Ko, Y. F. Chen, T. Yao, K. Miyajima, A. Yamamoto, and T. Goto, Appl. Phys. Lett. **77**, 537 (2000).

[65] W. Langbein, J. M. Hvam, M. Umlauff, H. Kalt, B. Jobst, and D. Hommel, Phys. Rev. B. **55**, R7383 (1997).

[66] V. Kutzer, B. Lummer, R. Heitz, A. Hoffmann, I. Broser, E. Kurtz, and D. Hommel, J. Cryst. Growth **159**, 776 (1996).

[67] M. Nakayama, A. Soumura, K. Hamasaki, H. Takeuchi, and H. Nishimura, Phys. Rev. B **55**, 10099 (1997)

[68] T. Goto, T. Takahashi, and M. Ueta, J. Phys. Soc. Jpn. **24**, 314 (1968).

[69] K. L. Shaklee, R. F. Leheny, and R. E. Nahory, Phys. Rev. Lett. **26**, 888 (1971).

[70] D. K. Shuh, R. S. Williams, Y. Segawa, J. Kusano, Y. Aoyagi, and S. Namba. Phys. Rev. B **44,** 5827 (1991).

[71] J. Sasai, K. Tanaka, and K. Hirao, Scripta Mater. **44**, 1225 (2001).

[72] K. Tsunetomo, R. Shimizu, A. Kawabuchi, H. Kitayama, and Y. Osaka, Jpn. J. Appl. Phys. **30**, 1764 (1991).

[73] H. Kurisu, K. Nagoya, N. Nakayama, S. Yamamoto, and M. Matsuura, J. Lumin. **87-89** 390 (2000).

[74] S. Takami, Y. Egashira, I. Honma, and H. Komiyama, Appl. Phys. Lett. **68**(7) 1020 (1996).

[75] T. Itoh, Y. Iwabuchi, and T. Kirihara, Phys. Status Solidi B **146**, 531 (1988).

[76] A. I. Ekimov, Al. L. Efros, and A. A. Onushchenko, Solid State Commun. **56,** 921 (1985).

[77] M. Ikezawa *et al.* Jpn. J. Appl. Phys. **36,** 4191 (1997).

[78] T. Itoh, M. Furumiya, and T. Ikehara C. Gourdon.: Solid State Commun. **73**, 271-274 (1990).

[79] N. Sakakura and Y. Masumoto, Phys. Rev. B **56,** 4051 (1997).

[80] M. Haselhoff and H.-J. Weber, Mat. Res. Bull. **30**, 607 (1995).

[81] M. Haselhoff and H.-J. Weber, Phys. Rev. B **58**, 5052 (1998).

[82] W.-T. Han and Y. K. Yoon, J. Non-Cryst. Solids **196,** 84 (1996).

[83] S. Kondo, M. Kakuchi, and T. Saito, J. Phys.: Condens. Matter **16**, 8085 (2004).

[84] Y. Masumoto, S. Okamoto, and S. Katayanagi, Phys. Rev. **50** 18658 (1994).

[85] S. Yano , T. Goto, and T. Itoh, J. Appl. Phys. **79** (1996) 8216.

[86] D. Westphal and A. Goldmann, J. Phys. C: Solid State Phys. **15**, 6661 (1982).

[87] Z. K. Tang, A. Yanase, Y. Segawa, N. Matsuura, and K. Cho, Phys. Rev. B **52**, 15 (1995).

[88] A. Yanase and Y. Segawa, Surf. Sci. **357-358,** 885 (1996).

[89] A.Yanase and Y.Segawa, Appl. Surf. Sci. **130-132**, 566 (1998).

[90] N. Nishida, K. Saiki, and A. Koma, Surf. Sci. **324**, 149 (1995).

[91] Q. Guo, L. Gui, and N. Wu, Appl. Surf. Sci. **99**, 229 (1996).

[92] E. Vanagas, D. Brinkmann, J. Kudrna, O. Crégut, P. Gilliot, R. Tomasiunas, and B. Hönerlage, J. Phys.: Condens. Matter **14,** 3627 (2002).

[93] G. R. Olbright and N. Peyghambarian, Solid State Commun. **58**, 337 (1986).

[94] L. O'Reilly, G. Natarajan, P. J. McNally, D. Cameron, O. F. Lucas, M. Martinez-Rosas, L. Bradley, A. Reader, and S. Daniels, J. Mater. Sci.: Mater. Electron. **16**, 415 (2005).

[95] L. O'Reilly, O. F. Lucas, P. J. McNally, A. Reader, Gomathi Natarajan, S. Daniels, D. C. Cameron, A. Mitra, M. Martinez-Rosas, and L. Bradley, J. Appl. Phys. **98**, 113512 (2005).

[96] K-K. Kim, J-H. Song, H-J. Jung, W-K. Choi, S-J. Park, J-H. Song, J-Y. Lee, and J. Vac. Sci. Technol. B **18**, 286 (2000).

[97] D. H. Fan, Z. Y. Ning, and M. F. Jiang, Appl. Surf. Sci. **245**, 414 (2005).

[98] M. Jung, J. Lee, S. Park, H. Kim, and J. Chang, J. Cryst. Growth **283**, 384 (2005).

[99] H. C. Ong, J. Y. Dai, K. C. Hung, Y. C. Chan, R. P. H. Chang, and S. T. Ho, Appl. Phys. Lett. **77**, 1484 (2000).

[100] M. W. Thompson, Philos. Mag. **18**, 377 (1968).

[101] S. D. Ekpe and S. K. Dew, J. Vac. Sci. Technol. A **21**, 476 (2003).

[102] A. R. Nyaiesh, Vacuum **36**, 307 (1986).

[103] G. L. Cano and R. W. Dressel, Phys. Rev. **139,** 1883 (1965).

[104] JCPDS Pattern Card No. 06-344, International Centre for Diffraction, New York, 1997.

[105] B. D. Cullity, Elements of X-ray Diffraction, 2nd Ed., Addison Wesley Publishing Company Inc. (1978).

[106] B. Chapman, Glow Discharge Processes, John Wiley & Sons, New York (1980).

[107] M. W. Thompson, Philos. Mag. **18**, 377 (1968).

[108] S. D. Ekpe and S. K. Dew, J. Vac. Sci. Technol. A **21**, 476 (2003).

[109] www.webelements.com (accessed on 05, Dec. 2006).

[110] J. A. Thornton, J. Vac. Sci. Technol. **11**, 666 (1974).

[111] W.-T. Han and Y. K. Yoon, J. Non-Cryst. Solids **196**, 84 (1996).

[112] J. Sasai, K. Tanaka, and K. Hirao, Scripta. Mater. **44**, 1225 (2001).

[113] B. Lin, Z. Fu, and Y. Jia, Appl. Phys. Lett. **79**, 943 (2001).

[114] X. Liu, X. Wu, H. Cao, and R. P. H. Chang, J. Appl. Phys. **95**, 3141 (1998).

[115] D. C. Reynolds, D. C. Look, and B. Jogai, J. Appl. Phys. **89,** 6189 (2001).

[116] E. G. Bylander, J. Appl. Phys. **49,** 1188 (1978).

[117] K. Vanheusden, W. L. Warren, C. H. Seager, D. R. Tallant, J. A. Voigt, and B. E. Gnade, J. Appl. Phys. **79,** 7983 (1996).

[118] M. Liu, A. H. Kitai, and P. Mascher, J. Lumin. **54,** 35 (1992).

[119] J. Chastain, Handbook of X-ray Photoelectron Spectroscopy, Physical Electronics Inc., USA (1992).

[120] A. Keudell, Plasma Sources Sci. Technol. **9,** 455 (2000).

[121] N. Fujimura, T. Nishihara, S. Goto, J. Xu, and T. Ito, J. Cryst. Growth **130,** 269 (1993).

[122] M. Ueta, H. Kanzaki, K. Kobayashi, Y. Toyozawa, and E. Hanumara, Excitonic processes in Solids, Springer-Verlag, Berlin, p.122 (1986).

[123] A. Kawamori, K. Edamatsu, and T. Itoh, J. Lumin. **237-239**, 1615 (2002).

[124] H. Kurisu, K. Nagoya, N. Nakayama, S. Yamamoto, and M. Matsuura, J. Lumin. **87-89,** 390 (2000).

[125] S. Kondo, M. Kakuchi, and T. Saito, J. Phys.: Condens. Matter **16,** 8085 (2004).

[126] D. K. Shuh and R. S. Williams, Phys. Rev. B **44,** 5827 (1991).

[127] M. Ueta, H. Kanzaki, K. Kobayashi, Y. Toyozawa, and E. Hanumara, Excitonic processes in Solids, Springer-Verlag, Berlin (1986).

[128] V. A. Fonoberov, K. A. Alim, A. A. Balandin, F. Xiu, and J. Liu, Phys. Rev. B, **73,** 165317 (2006).

[129] Y. Zhang, B. Lin, X. Sun, and Z. Fu, Appl. Phys. Lett. **86**, 131910 (2005).

[130] K. Saito, M. Hasuo, T. Hatano, and N. Nagasawa, Solid State Commun. **94,** 33 (1995).

[131] T. Goto, T. Takahashni, and M. Ueta, J. Phys. Soc. Jpn. **24**, 314 (1968).

[132] A. K. Viswanath, J. I. Lee, S. Yu and D. Kim, Y. Choi, and C. Hong, J. Appl. Phys. **84,** 3848 (1998).

[133] K. Edamatsu, T. Itoh, K. Matsuda, and S. Saikan, Phys. Rev. B **64,** 195317 (2001).

[134] Y. Kaifu and T. Komatsu, Phys. Stat. Sol. (B) **48,** K125 (1971).

[135] Y. Masumoto, T. Wamura, and A. Iwaki, Appl. Phys. Lett. **55,** 2535 (1989).

[136] X. T. Zhang, Y. C. Liu, Z. Z. Zhi, J. Y. Zhang, Y. M. Lu, D. Z. Shen, W. Xu, X. W. Fan, and X. G. Kong, J. Lumin. **99,** 149 (2002).

[137] Q. X. Zhao, M. Willander, R. E. Morjan, Q-H. Hu, and E. E. B. Campbell, Appl. Phys. Lett. **83,** 165 (2003).

[138] M. S. Minsky, S. B. Fleischer, A. C. Abare, J. E. Bowers, E. L. Hu, S. Keller, and S. P. Denbaars, Appl. Phys. Lett. **72,** 1066 (1998).

[139] K-K. Kim, J-H. Song, H-J. Jung, W-K. Choi, S-J. Park, and J-H. Song, J. Appl. Phys. **87**, 3573 (1996).

[140] A. Göbel, T. Ruf, M. Cardona, C. T. Lin, J. Wrzesinski, M. Steube, K. Reimann, J.-C. Merle, and M. Joucla, Phys. Rev. B **57** 15183 (1998).

[141] A. Mitra, L. O'Reilly, O. F. Lucas, G. Natarajan, A. L. Bradley, P. J. McNally, S. Daniels, D. C. Cameron, A. Reader, and M. Martinez-Rosas, J. Lumin. communicated.

[142] T. Koda, T. Murahashi, T. Mitani, S. Sakoda, and Y. Onodera, Phys. Rev. B **5**, 705 (1972).

[143] J. B Wagner and C. Wagner, J. Chem. Phys. **26** 1597 (1957).

[144] A. Brune and J. B. Wagner, Mater. Res. Bull. **30**, 573 (1995).

[145] L. O'Reilly, A. Mitra, G. Natarajan, O. F. Lucas, P. J. McNally, S. Daniels, D. C. Cameron, A. L. Bradley, and A. Reader, J. Cryst. Growth, **287,** 139 (2006).

[146] V. Desmaris, J. Eriksson, N. Rorsman, and H. Zirath, Electrochem. Solid-State Lett. **7**, G72–G74 (2004).

[147] K. Ip, Y. W. Heo, K. H. Baik, D. P. Norton, S. J. Pearton, and F. Ren, J. Vac. Sci. Technol. B **22**, 171 (2004).

[148] J. George and M. K. Radhakrishnan, J. Phys. D: Appl. Phys. **14**, 899 (1981)

[149] L. Maissel and R. Glang, Handbook of Thin Film Technology, McGraw-Hill, New York (1970).

[150] S. Roberts, Phys. Rev. **76**, 1215 (1949).

[151] I. P. Kaminow and E. H. Turner, Phys. Rev. B **5**, 1564 (1972).

[152] J. E. Potts, R. C. Hanson, C. T. Walker, and C. Schwab, Phys. Rev. B **9**, 2711, (1974).

[153] T. Goto, J. Phys. Soc. Jpn., **20,** 1654 (1965).

List of publications

Publications included in this thesis

1. "Stoichiometry control of sputtered CuCl thin films: Influence on ultraviolet emission properties"
   Gomathi Natarajan, R. T. Rajendra Kumar, S. Daniels, D. C. Cameron, and P. J. McNally
   J. Appl. Phys. ***100****, 096108 (2006).*

2. "Growth of CuCl thin films by magnetron sputtering for UV optoelectronic applications"
   Gomathi Natarajan, S. Daniels, D. C. Cameron, L. O' Reilly, P. J. McNally, O. Lucas, R. T. Rajendra Kumar, I. Reid, A. Mitra, and L. Bradley
   J. Appl. Phys. ***100,*** *033520 (2006).*

3. "Optical investigations on sputtered CuCl thin films"
   Gomathi Natarajan, A. Mitra, L. O' Reilly, S. Daniels, D. C. Cameron, P. J. McNally, O. Lucas, and L. Bradley
   Mater. Res. Soc. Symp. Proc. ***891****, 0891-EE03-22.1 (2005).*

4. "Structural and optoelectronic properties of sputtered copper (I) chloride"
   Gomathi Natarajan, L. O' Reilly, S. Daniels, D. C. Cameron, P. J. McNally, O. Lucas, A. Reader, A. Mitra, and L. Bradley
   Proc. SPIE Int. Soc. Opt. Eng. ***5825****, 364 (2005).*

5. "Electrical studies on sputtered CuCl thin films"
   Gomathi Natarajan, R.T. Rajendra Kumar, S. Daniels, D. C. Cameron, and P. J. McNally
   J. Mater. Sci. Mater. Electron., In press - DOI: 10.1007/s10854-007-9310-9 (2007).

6. "Influence of target to substrate distance on the optical properties of sputtered CuCl films"
   Gomathi Natarajan, S. Daniels, D. C. Cameron, and P. J. McNally
   Thin Solid Films, In press- DOI: 10.1016/j.tsf.2007.03.069 (2007).

7. "Temperature dependent optical properties of UV emitting γ-CuCl films on Si"
   Gomathi Natarajan, A. Mitra, S. Daniels, D. C. Cameron, and P. J. McNally
   Thin Solid Films, In press - DOI: 10.1016/j.tsf.2007.07.112 (2007).

Other relevant publications

8. "Impact on structural, optical and electrical properties of CuCl by incorporation of Zn for n-type doping"
   L. O' Reilly, A. Mitra, Gomathi Natarajan, O. F. Lucas, P. J. McNally, S. Daniels, D. C. Cameron, A. L. Bradley, and A. Reader
   J. Cryst. Growth ***287****, 139 (2006).*

9. "Encapsulation of the heteroepitaxial growth of wide bandgap γ-CuCl on silicon substrates"
   O. F. Lucas, L. O' Reilly, Gomathi Natarajan, P. J. McNally, S. Daniels, D. M. Taylor, S. William, D. C. Cameron, A. L. Bradley, and A. Mitra
   J. Cryst. Growth ***28****, 112–117 (2006).*

10. "Room temperature ultra-violet luminescence from γ-CuCl grown on near lattice–matched silicon"
    L. O' Reilly, O. F. Lucas, P. J. McNally, A. Reader, Gomathi Natarajan, S. Daniels, D. C. Cameron, A. Mitra, M. Martinez-Rosas, and A. L. Bradley
    J. Appl. Phys. ***98****, 113512 (2005).*

11. "Growth and characterisation of wide-bandgap I-VII optoelectronic materials on silicon"
    L. O' Reilly, Gomathi Natarajan, P. J. McNally, D. C. Cameron, O. F. Lucas, M. Martinez-Rosas, L. Bradley, and A. Reader
    J. Mater. Sci. Mater. Electron. ***16*** *(7), pp. 415-419 (2005).*

12. "The use of wide-bandgap CuCl on silicon for ultra-violet photonics"
    L. O' Reilly, Gomathi Natarajan, P. J. McNally, S. Daniels, O. F. Lucas, A. Mitra, M. Martinez-Rosas, L. Bradley, A. Reader, and D. C. Cameron
    Proc. SPIE Int. Soc. Opt. Eng. ***5825****, 29 (2005).*

13. "Towards the fabrication of a UV light source based on CuCl thin films"
    A. Mitra, O. F. Lucas, L. O'Reilly, P. J. McNally, S. Daniels, and Gomathi Natarajan
    J. Mater. Sci. Mater. Electron., corrected proof doi: 10.1007/s10854-007-9178-8 (2007).

14. "Characterisation of n-type c-CuCl on Si for UV optoelectronic applications"
    L. O'Reilly, A. Mitra, F. O. Lucas, Gomathi Natarajan, P. J. McNally, S. Daniels, A. Lankinen, D. Lowney, A. L. Bradley, and D. C. Cameron
    J. Mater. Sci. Mater. Electron., In press - doi: 10.1007/s10854-007-9173-0 (2007).

15. "CuCl films on silicon substrates: toward optoelectronic devices"
    A. Mitra, L. O' Reilly, O. F. Lucas, Gomathi Natarajan, A. L. Bradley, P. J. McNally, S. Daniels, D. C. Cameron, A. Reader, and M. Martinez-Rosas
    J. Lumin., communicated.

Patent

16. "A new γ- CuCl based electroluminescent device for the production of ultra-violet light on silicon substrate"
    P. J. McNally, D. C. Cameron, L. O' Reilly, Gomathi Natarajan, O. F. Lucas, and A. Reader.
    Filing Date: 25 June 2004. International Application No. ***PCT/IE2005/000072.***

Conference presentations

1. "Influence of target to substrate distance on the optical properties of sputtered CuCl"
   Gomathi Natarajan, S. Daniels, D. C. Cameron, and P. J. McNally: Thin Films 2006, 11- 15 Dec. 2006, Singapore.

2. "Electrical studies on sputtered CuCl thin films"
   Gomathi Natarajan, S. Daniels, D. C. Cameron, and P. J. McNally: 6th Int. Conf. on Materials for Microelectronics & Nanoengineering (MFMN2006), 29-31 Oct. 2006, Cranfield, UK.

3. "Stoichiometry and microstructure control of ultraviolet emitting sputtered CuCl thin films"
   Gomathi Natarajan, L. O'Reilly, O. F. Lucas, A. Mitra, S. Daniels, P. J. McNally, and D. C. Cameron: Irish Plasma and Beam Processing Group (IPBPG 2006) conference, 11-12 July 2006, Dublin, Ireland.

4. "Optimization of room temperature UV emitting CuCl thin films: Temperature dependent optical properties"
   Gomathi Natarajan, A. Mitra, S. Daniels, D. C. Cameron, and P. J. McNally: European Materials Research Society (EMRS), 29 May – 2 June 2006, Nice, France – Winner of the ***best paper*** and ***young scientist*** awards.

5. "Optical investigations on sputtered CuCl thin films"
   Gomathi Natarajan, A. Mitra, L. O' Reilly, S. Daniels, D. C. Cameron, P. J. McNally, O. F. Lucas, and L. Bradley: Materials Research Society (MRS) Symposium, 28 Nov. - 2 Dec. 2005, Boston, USA.

6. "Structural and optoelectronic properties of sputtered copper (I) chloride"
   Gomathi Natarajan, L. O' Reilly, S. Daniels, D. C. Cameron, P. J. McNally, O. Lucas, Reader, A. Mitra, and L. Bradley: Proc. SPIE Int. Soc. Opt. Eng. 5825, 364 (2005), 4–6 April 2005, Dublin, Ireland.

7. "Plasma diagnostics for the rf physical vapour deposition of CuCl thin films"
   Gomathi Natarajan, S. Daniels, D. Cameron, L. O'Reilly, and P. McNally: GEC04 meeting of the American Physical Society, 26-29 Sept. 2004, Bunratty, Ireland.